Influence of plasma rotation on tearing mode stability on the ASDEX Upgrade Tokamak

Sina Marie Ariane Fietz

SIGILL·UNIVERSITAT·LUDOVIC·MAXIM

München 2013

Influence of plasma rotation on tearing mode stability on the ASDEX Upgrade Tokamak

Sina Marie Ariane Fietz

Dissertation
an der Fakultät für Physik
der Ludwig-Maximilians-Universität
München

durchgeführt am
Max-Planck-Institut für Plasmaphysik

vorgelegt von
Sina Marie Ariane Fietz
aus München

München, den 23. September 2013

Erstgutachter: Prof. Dr. Hartmut Zohm
Zweitgutachter: Prof. Dr. Harald Lesch
Tag der mündlichen Prüfung: 16.12.2013

Zusammenfassung

In zukünftigen Fusionsexperimenten, wie ITER, wird erwartet, dass das Auftreten von neoklassischen Tearing Moden (NTM) den Betrieb und den Einschluss des Plasmas stark einschränken wird. NTMs entstehen als Folge einer initialen Störung, auch Trigger-Instabilität genannt, welche zur Ausbildung magnetischer Inseln führt. NTMs werden vom helikalen Stromverlust innerenhalb der Insel getrieben und haben einen Druckverlust des gesamten Plasmas zur Folge. Zusätzlich können NTMs die Plasmarotation zum erliegen bringen, sich an die Wand heften („locken") und letztendlich die Entladung mittels einer „Disruption" beenden. In ITER wird der Druckverlust die mögliche Fusionsleistung limitieren, wohingegen eine NTM induzierte „Disruption" höchstwahrscheinlich die Gefäßwand beschädigen wird. Um NTMs in ITER verhindern oder zumindest kontrollieren zu können, müssen heutige Beobachtungen und Erkenntnisse im Hinblick auf ITER extrapoliert werden. Ein wichtiger Aspekt diesbezüglich ist die Rotationsabhängigkeit von NTMs, vor allem bei deren Entstehung, da ITER voraussichtlich, im Vergleich zu heutigen Experimenten, bei sehr niedriger Rotation betrieben wird. Bis jetzt existiert noch keine Theorie, die diesen Zusammenhang beschreiben kann. Aus diesem Grund müssen die heutigen Experimente Anhaltspunkte für die korrekte Beschreibung der Physik liefern. Aus den im Experiment gewonnenen Daten können auch Skalierungen entwickelt werden, mit Hilfe derer das Verhalten in ITER vorhergesagt werden kann. Ein weiterer wichtiger Punkt ist die Untersuchung des Einflusses von extern angelegten magnetischen Störfeldern (MS-Felder) auf die Stabilität und Rotationsfrequenz von NTMs. Diese MS-Felder werden in ITER in erster Linie zur Unterdrückung von Randinstabilitäten verwendet. Als Nebeneffekt können diese Felder jedoch auch zum Abbremsen von NTMs führen. Dies wiederum kann das Auftreten von nicht rotierenden NTMs unterstützen. Zusätzlich können diese Störfelder auch die Stabilität von NTMs beeinflussen. Es ist wichtig, diese Wechselwirkung mithilfe von Modellen, die an heutigen Experimenten bestätigt wurden, für ITER vorherzusagen.

Der Einfluss der Plasmarotation auf die Entstehung von NTMs wird am Tokamak ASDEX Upgrade (AUG) untersucht. Es wurde eine Datenbank erstellt, in der jedem NTM- Entstehungspunkt die zugehörige Trigger-Instabilität zugeordnet wurde. Darauf basierend wird nicht nur der Einfluss der Rotation auf die Entstehung von NTMs untersucht, sondern auch der des Rotationsgradienten und der der differentiellen Rotation, bezüglich des Ortes der Insel und der Trigger-Instabilität. In Abhängigkeit von der Plasmarotation, normiert auf die Alfvén Geschwindigkeit, wird die Ausbildung einer oberen Grenze für die Entstehung von NTMs in Abhängigkeit vom Plasmadruck beobachtet. Dieser Grenzwert steigt mit wachsender normierter Rotation und ist unabhängig von der Rotationsrichtung. Diese Beobachtung impliziert, dass NTMs bei niedriger Rotation, wie in ITER, leichter destabilisiert werden können. Steile Rotationsprofile hingegen scheinen die Entstehung von NTMs zu erschweren. Als weiterer Aspekt wird der Einfluss von extern angelegten Störfeldern auf NTMs und die Plasmarotation an AUG untersucht. Die Störfelder werden von Spulen am Rand des Plasmagefäßes erzeugt. Die Theorie sagt vorher, dass die resonanten Komponenten des Störfeldes ein lokales Drehmoment im Bereich der Insel induzieren und zusätzlich die Amplitude dieser Insel beeinflussen. Die nicht resonanten Komponenten führen zu einem Abbremsen des gesamten Plasmas, beeinflussen jedoch die Stabilität der Insel nicht. Im Experiment wird das Abbremsen und „locken" von NTMs, jedoch nur ein geringer Einfluss auf die Inselampli-

tude, beobachtet. Diese experimentellen Beobachtungen können mit den Ergebnissen einer Modellierung basierend auf der Theorie verglichen werden. Die resonanten Effekte scheinen über die nicht resonanten Effekte zu dominieren, wobei die nicht Resonanten in den untersuchten Entladungen vernachlässigbar klein zu sein scheinen. Berücksichtigt man jedoch in der Modellierung nur die resonanten Komponenten am Ort der Insel, so kann die Entwicklung der Insel nicht beschrieben werden. Die Modellierung zeigt, dass die resonanten Effekte an verschiedenen Flächen berücksichtigt werden müssen. Diese Effekte summieren sich auf und führen in ihrer Gesamtheit zum Abbremsen des Plasmas und begleitend auch der Insel. Somit müssen, um die Entwicklung einer einzelnen Insel zu beschreiben, alle Flächen und die dazugehörigen resonanten Effekte mitberücksichtigt werden.

Abstract

Neoclassical tearing modes (NTM) are one of the most serious performance limiting instabilities in next-step fusion devices like ITER. NTMs are destabilised as a consequence of a seed perturbation (trigger) and are driven by a loss of helical bootstrap current inside the island. The appearance of these instabilities is accompanied with a loss of confined plasma energy. Additionally, these modes can stop the plasma rotation, lock to the vessel wall, flush out all plasma energy and terminate a discharge via a disruption. In ITER the confinement reduction will limit the achievable fusion power, whereas a disruption is likely to damage the vessel wall. In order to mitigate and control NTMs in ITER, extrapolations based on the present understanding and observations must be made. One key issue is the rotation dependence of NTMs, especially at the NTM onset. ITER will be operated at low plasma rotation, which is different from most present day experiments. No theory is currently available to describe this dependence. Experiments are therefore required to provide a basis for the theory to describe the physics. Additionally from the experiments scalings can be developed and extrapolated in order to predict the NTM behaviour in the parameter range relevant for ITER. Another important issue is the influence of externally applied magnetic perturbation (MP) fields on the NTM stability and frequency. These fields will be used in ITER primarily for the mitigation of edge instabilities. As a side effect they can slow down an NTM and the plasma rotation, which supports the appearance of locked modes. Additionally, they can also influence the stability of an NTM. This interaction has to be predicted for ITER, based on models validated at present day devices.

In this work the influence of plasma rotation on the NTM onset at the ASDEX Upgrade tokamak (AUG) is investigated. An onset database has been created in which the different trigger mechanisms have been identified. Based on this, the influence not only of the plasma rotation, but also of the rotation gradient and the differential rotation between the NTM and the radial location of the trigger perturbation, on the NTM stability is analysed. The formation of an upper NTM onset threshold, which depends on the plasma pressure, is observed in correlation with a plasma rotation normalised to the Alfvén velocity. This NTM onset threshold increases with normalised rotation and is independent of the direction of the plasma rotation. NTMs can therefore be more easily triggered at low plasma rotation, like in ITER. However, steeper rotation profiles seem to hamper the appearance of NTMs.

The effect of externally applied MPs on NTMs and the plasma rotation is investigated using coils mounted at the outboard side of AUG. Theory predicts that the resonant components of the applied MP field exert local torques and influence the stability of NTMs. The non-resonant components of the MP field do not influence NTMs directly but slow down the plasma rotation globally. In experiment the slowing down and locking of NTMs is observed. However, the mode amplitude remains almost unchanged. These experimental observations are compared to modelling results. The resonant effects seem to dominate over the non-resonant effects for the investigated discharges but the evolution of an island can not be described if only the resonant effects at the NTM surface are taken into account. The modelling reveals that the resonant torques at different surfaces act together as a global resonant torque that is responsible for the slowing down of the NTM. In oder to describe the evolution of a single NTM all instabilities present in the plasma and the impact of all resonant contributions at several surfaces must be taken into account.

Contents

Chapter 1

Introduction

1.1 Nuclear fusion

Nuclear fusion is the merging of light atoms, which collide at very high speed and form a new heavier atom. In this reaction the mass of the atoms is not conserved and energy is released according to $E = mc^2$, where m is the mass and c the speed of light. This energy release is caused by an interplay of the nuclear force, which keeps together the atomic nuclei, and the Coulomb force. The fusion of atoms with an atomic nucleus smaller than iron (^{58}Fe/^{56}Fe) has a positive energy balance. In contrast the more familiar, opposite process is the fission (splitting) of atoms with a mass higher than iron, which also releases energy.

Nuclear fusion is the process which powers the stars and also takes place in our sun. The fusion reaction in stars is the proton (p) - proton (p) chain, which converts hydrogen into helium and releases in total 26.7 MeV of energy [1].

$$^{1}\mathrm{H} + {}^{1}\mathrm{H} \rightarrow {}^{2}\mathrm{D} + e^{+} + \nu_e + 1.44\,\mathrm{MeV} \tag{1.1}$$

$$^{2}\mathrm{D} + {}^{1}\mathrm{H} \rightarrow {}^{3}\mathrm{He} + \gamma + 5.49\,\mathrm{MeV} \tag{1.2}$$

$$^{3}\mathrm{He} + {}^{3}\mathrm{He} \rightarrow {}^{4}\mathrm{He} + {}^{1}\mathrm{H} + {}^{1}\mathrm{H} + 12.86\,\mathrm{MeV} \tag{1.3}$$

The biggest limitation of a fusion process is the cross section (σ), which is a measure for the probability of a fusion reaction. The cross section of the whole p-p chain is limited due to the small reaction rate of reaction (1.1) to take place. The neutron is produced via the weak force, which does not depend on the temperature and is very unlikely. Therefore, in the sun it takes around $1.4 \cdot 10^{10}$ years until two protons fuse. Hence, this reaction can not be used to realise fusion on earth and another reaction has to be used. In general σ depends strongly on the temperature, which corresponds to the energy and velocity of the atoms. High temperatures (velocities) are needed to overcome the repelling Coulomb force of two nuclei, in order to bring them close enough together to make fusion possible. The reaction with the highest σ at the achievable temperatures on earth, is the fusion of deuterium (D) and tritium (T) (figure 1.1).

$$^{2}D + {}^{3}T \rightarrow {}^{4}He + n + 17.6\,\mathrm{MeV} \tag{1.4}$$

This reaction releases an energy of 17.6 MeV in total, which is carried by a neutron n and an α-particle (^{4}He) in the form of kinetic energy. Deuterium can be extracted in unlimited

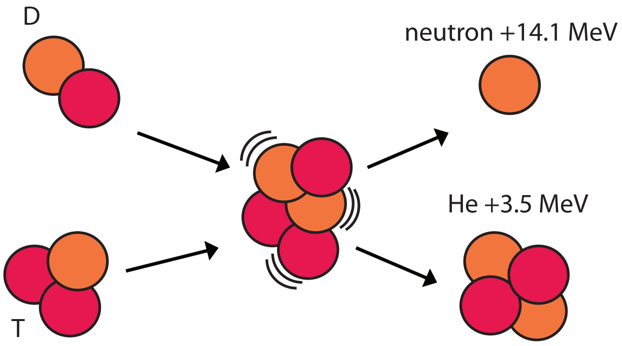

Figure 1.1: Fusion of deuterium (D) and tritium (T) which produces a ^{4}He (α-particle), a neutron and 17.6 MeV.

quantities from water, whereas tritium is not available naturally. In a future fusion device T can be made from the reaction of lithium (Li, 7.5%^{6}Li+92.5%^{7}Li) using the released neutron from the fusion of D-T in the breeding process:

$$n + {}^6\text{Li} \rightarrow {}^4\text{He} + \text{T} + 4.8\,\text{MeV} \quad (1.5)$$

$$n + {}^7\text{Li} \rightarrow {}^4\text{He} + \text{T} + n' - 2.5\,\text{MeV} \quad (1.6)$$

In future fusion devices this process takes place in the 'breeding' blankets, which will be installed directly behind the first wall. While D is not radioactive, T is a radioactive atom with a half-life of around 12.3 years.

1.2 Tokamak concept

At the high temperatures (10-100 keV) required to reach the maximal reaction rate for the fusion of D-T, all hydrogen atoms are fully stripped and form a plasma. Due to the high mass of the sun the plasma is confined via gravity. In a fusion reactor one possibility to confine a plasma is to use magnetic fields. In a plasma all particles are charged and gyrate in the applied magnetic field due to the Lorentz force. In this way, the transport perpendicular to the field lines can be reduced and the plasma can be confined. One concept to confine plasmas by imposing magnetic fields is the tokamak[1] configuration, illustrated in figure 1.2. In a tokamak a toroidal (B_{tor}) and a poloidal (B_{pol}) magnetic field are superimposed, which leads to a helical magnetic field structure of the total magnetic field (B_{tot}). The toroidal magnetic field is created by external magnetic field coils, which are distributed around the tokamak torus. The poloidal magnetic field is about one order of magnitude smaller than the toroidal field and it is produced by a toroidal current (I_{p}) flowing inside the plasma. This toroidal current is induced by ramping the flux in a transformer coil, which is situated in the centre of the torus. The direction of the toroidal and the poloidal magnetic field in a tokamak geometry, as it is normally used in the ASDEX Upgrade tokamak (AUG) (described in more detail in section 2.1) [2], as well as the radial profiles in a poloidal plane are illustrated in figure 1.3. Additionally, a tokamak coordinate system is shown in figure

---

[1] Russian abbreviation for 'toroidal chamber with magnetic coils'

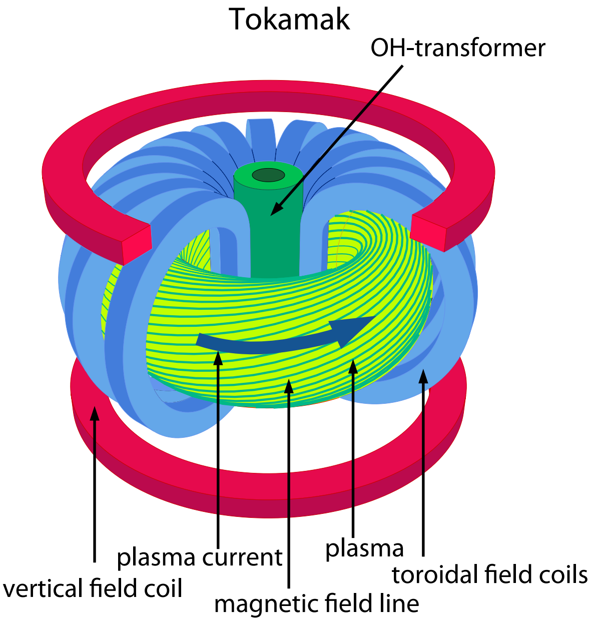

Figure 1.2: Schematic of a tokamak.

1.3 (a). The superposition of B_{tor} and B_{pol} results in an axisymmetric equilibrium, which consists of nested magnetic flux surfaces, as illustrated in figure 1.4 (a). This equilibrium is sustained when the magnetic force and the kinetic pressure gradient ($\vec{\nabla}p$) (figure 1.3 (b)) balance each other:

$$\vec{j} \times \vec{B} = \vec{\nabla}p \tag{1.7}$$

This condition implies that the plasma (kinetic) pressure is constant on a magnetic surface and that also the current sheets lie within a magnetic surface. In a tokamak equilibrium it is common to introduce the poloidal magnetic flux function Ψ, which is constant on a

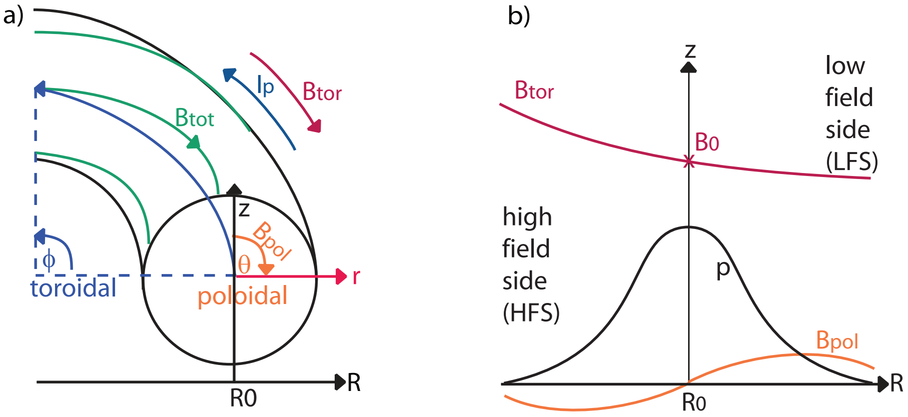

Figure 1.3: (a) Illustration of a typical AUG (tokamak) coordinate system, where all important directions are indicated, including the toroidal, the poloidal and the total magnetic field direction. The angle ϕ indicates the toroidal and θ the poloidal and r the radial direction. (b) Schematic radial profiles of B_{tor}, B_{pol} and the kinetic pressure p.

magnetic flux surface. The poloidal magnetic flux through a surface (dS) can be calculated from $\int B_{\mathrm{pol}} dS$. In a tokamak equilibrium the flux surfaces can be labelled with a normalised poloidal flux label ρ_{pol}, which also serves as radial coordinate, and is defined to be zero in the plasma core and one at the last closed flux surface (separatrix)

$$\rho_{\mathrm{pol}} = \sqrt{\frac{\Psi - \Psi_{\mathrm{core}}}{\Psi_{\mathrm{sep}} - \Psi_{\mathrm{core}}}}. \tag{1.8}$$

The helicity (pitch) of the magnetic field lines on a flux surface can be described by the safety factor q, which is defined as the number of toroidal turns per poloidal turn of one field line [3]. Using a cylindrical approximation this can be expressed as a ratio of the toroidal and poloidal magnetic field

$$q \approx \frac{r B_{\mathrm{tor}}}{R_0 B_{\mathrm{pol}}}, \tag{1.9}$$

with R_0 the major radius at the magnetic axis (figure 1.3). In standard operation q increases from the core ($q \approx 1$) towards the plasma edge ($q \rightarrow \infty$), which is denoted as 'positive shear'. From the stability point of view the rational q surfaces play an important role. At these surfaces a field line closes onto itself after m toroidal and n poloidal turns. At these surfaces q can be written as $q = m/n$, with m and n integers. At rational q surfaces a variety of magneto hydrodynamic (MHD) instabilities can develop, which break down the magnetic structure of nested flux surfaces and consequently enhance the radial transport of heat and particles.

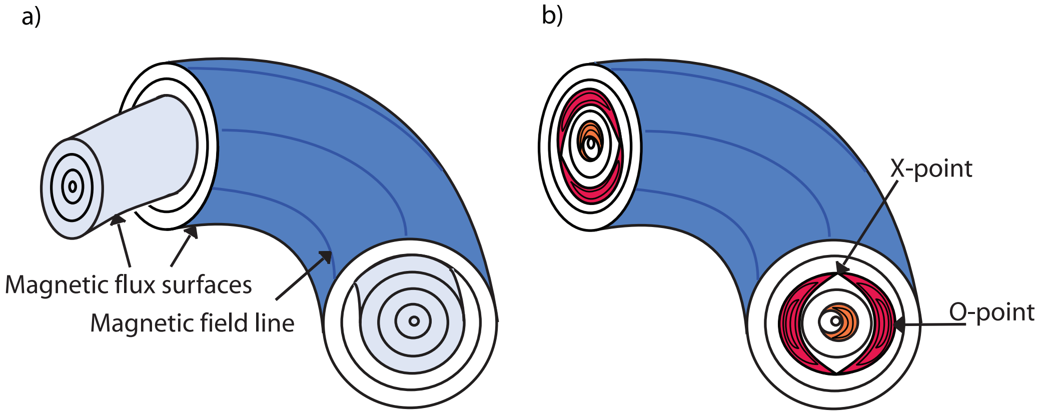

Figure 1.4: Magnetic flux surfaces and field lines in a tokamak geometry for two cases: (a) unperturbed equilibrium with nested flux surfaces and (b) perturbed equilibrium due to the presence of two magnetic islands at the q=2 and q=1 surface.

1.3 Magnetic islands

One prominent group of MHD instabilities are tearing modes. These are resistive MHD instabilities in that they grow slowly compared to ideal instabilities on the resistive time scale of the plasma. In the presence of tearing modes the topology of nested flux surfaces breaks down and, due to magnetic reconnection, island structures with its characteristic X- and O-points are formed. A magnetic island has a helical structure, which is centred at a resonant surface r_{res} and closes onto itself after n poloidal and m toroidal turns. This leads to the classification of an island according to its helical structure and location with respect to q, via m the poloidal and n the toroidal mode number. In figure 1.4 (b) a perturbed equilibrium is shown, with two reconnected flux surfaces in the presence of an (m/n)=(1/1) and (2/1) island.

Tearing modes are current driven instabilities. They are formed due to a current perturbation which changes the equilibrium in a way that the reconnection of field lines is energetically favourable. Classical tearing modes are driven by the gradient of the equilibrium current profile, characterised by the Δ' term, defined in chapter 3, equation (3.19). The formation of a magnetic island is accompanied by an enhanced radial transport across the island region. Particles and heat radially transit the island region by rapidly flowing along the field lines rather then slowly diffusing across the flux surfaces. This is equal to a short-circuit, which leads to a confinement degradation and a flattening of the pressure profile inside the island. In a plasma with low pressure the flattening of the pressure profile across the island leads only to a negligible loss of pressure and confinement, which has no further consequences. The plasma β is a typical parameter to characterise a plasma and the pressure therein present. The plasma β is defined as the ratio of kinetic to magnetic pressure $\beta = p/(2\mu_0 B^2)$. So the classical tearing modes are present in low β plasmas.

In a plasma with high β the situation is different. In these plasmas the flattening of the pressure profile across the island leads to a loss of 'bootstrap' current inside the island. The bootstrap current is a current which is proportional to the gradient of the pressure and has a neoclassical origin [4, 5]. This helical current hole perturbation exists only inside the island and leads to an additional drive of the mode, which now depends on β. These modes are called neoclassical tearing modes. NTMs are typically Δ' stable. Consequently, they should only occur growing out of a classical tearing mode. However, an initial trigger instability can perturb the equilibrium pressure profile at a resonant surface and generate a so-called seed island there. If this seed island and β are large enough the pressure profile is flattened initially, bootstrap current is lost and an NTM can be destabilised. The drive of an NTM is a non-linear process, which results in a rapid growth of the island. A bigger island leads to a larger region of flat pressure, therefore, more bootstrap current is lost, which increases again the island size. For an NTM both the triggering process as well as the NTM drive depends on the plasma β. The higher the β the stronger the NTM drive and therefore, NTMs grow fast in plasmas with high β. Additionally, at higher β even a weak trigger perturbation, producing a small seed island, can destabilise an NTM. As a consequence the NTM onset threshold decreases with increasing β.

The problem of NTMs is that every formation of an NTM in a high β plasma is accompanied with a substantial confinement degradation. The influence of an NTM with moderate size on an experimental temperature profile at AUG is shown in figure 1.5. The NTM leads to a reduction of T_{e} and also of the energy confinement time τ_{e} of around 20%. The energy

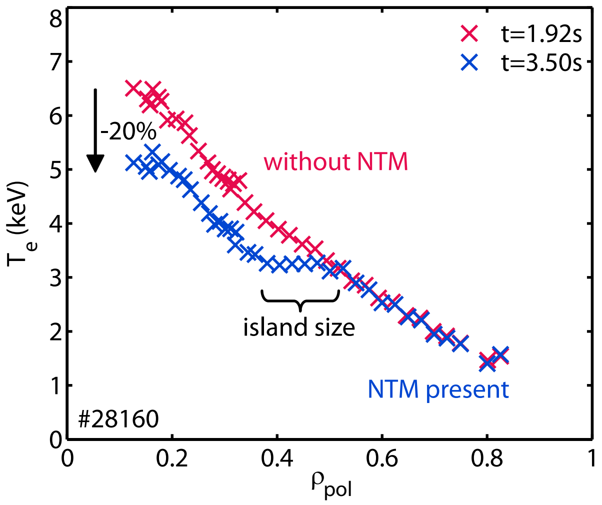

Figure 1.5: Electron temperature profile before and during the presence of an NTM. The flat region caused by the enhanced transport across the island gives information on the actual size of the island.

confinement time τ_e is the ratio of the total energy stored in the plasma and the supplied power. In the worst, case NTMs not only reduce the confinement but also stop the plasma rotation while they are growing and can eventually lock to the wall. During the locking phase they grow even faster. In most cases locked modes terminate the discharge via a disruption. Present day experiments can still operate when NTMs are present, but in future fusion devices the effects of NTMs will be even more dramatic. This is already expected to be a problem in ITER [6], the next step fusion device, which is under construction in Cadarache (France) as a collaboration of China, Europe, India, Japan, Russia, South Korea and USA. ITER has the scientific goal to produce 10 times more fusion power than it consumes as input heating power ($Q = P_{\mathrm{fusion}}/P_{\mathrm{heat}} = 10$).

The fusion power density scales with the pressure squared and, hence, it is strongly limited by the occurrence of NTMs. Another important figure of merit in fusion reactions is the triple product of density n, temperature T and energy confinement time τ_e. When this product exceeds a certain value all external heating mechanisms can be removed and the temperature in the plasma is maintained purely by the α-particles produced by the fusion reaction (i.e. ignition). For the D-T reaction this is described by the Lawson criterion, which predicts ignition for $nT\tau_e > 10^{21}\,\mathrm{keVs/m^3}$ [3]. However, if NTMs decrease the energy confinement time and also the plasma temperature, the triple product will be strongly limited when NTMs are present.

Besides the effects of the confinement reduction, the effects of a disruption caused by a locked mode will be even worse. The energy stored in the plasma will be released suddenly and the wall of a reactor is unlikely to be able to withstand this and the attendant forces without damage. Hence, NTMs are strongly performance limiting and have to be controlled or avoided.

1.4 Focus of this thesis

To be able to control NTMs and predict their behaviour it is necessary to extrapolate the present understanding to larger devices like ITER, which will be operated under different conditions. A key parameter for the NTM physics and predictions for ITER is the rotation dependence. Compared to present day devices with typically substantial rotation, ITER will be operated at low plasma rotation due to a low applied torque compared to the plasma viscosity. With these differences the question arises, how the NTM behaviour changes with rotation and if predictions can be made from present experiments? Especially the understanding of the seeding mechanism and the influence of rotation on the NTM onset threshold are an essential part for the control and avoidance of NTMs.

Another important issue is the influence of externally applied magnetic perturbation fields on the NTM stability and rotation frequency. In ITER external saddle coils are planned, necessary for the mitigation of instabilities at the edge (ELMs) [7] which would otherwise damage the wall. These coils produce magnetic perturbation (MP) fields consisting of resonant and non-resonant components. The resonant MP components penetrate the plasma and can create magnetic islands at the corresponding resonant surfaces. In addition, previously existing rotating modes can be influenced. They are slowed down and lock to the MP field. The non-resonant components mainly influence the plasma rotation via the neoclassical toroidal viscous torque (NTV), which further slows down the plasma rotation. Consequently, static MP fields support the appearance of locked modes, which in most cases lead to a disruption. In addition to the intrinsic behaviour of NTMs, also the influence of those external perturbation fields on NTMs has to be included in the predictions. The best way to achieve reliable predictions is a combination of an extrapolation of present data, by means of normalised quantities, and modelling results based on theoretical understanding. In this thesis both the influence of rotation on the NTM onset and the interaction of a rotating mode with externally applied error fields have been analysed.

In the first part of this thesis the influence of rotation on the NTM onset is studied, including a database consisting of around 70 data points for the NTM onset. The general dependence of the NTM onset threshold on rotation is analysed, where one focus is on the clarification of the origin of this dependence. Is it caused by an influence of rotation on the island stability or does the trigger mechanism depend on rotation? Furthermore, the influence of the characteristics of the rotation profile (like gradients or the differential rotation of different surfaces) has been analysed. Differences and agreements between the AUG results and other devices are pointed out and predictions and suggestions for ITER are made. To summarise the key questions addressed in this thesis:

- How does the plasma rotation influence the NTM onset?
- Is the dependence of the NTM onset threshold on rotation caused by the intrinsic NTM stability or the triggering process?
- How does the rotation profile in general, like the rotation gradient and differential rotation of different surfaces, influence the NTM threshold?

- Is the behaviour at AUG in agreement with observations at other devices?
- What do the scalings predict for ITER?

In the second part of this thesis the influence of externally applied MP fields on pre-existing rotating NTMs is investigated. The interaction of a rotating island with the MP field in experiments is analysed in detail. These observations are compared to the theoretical predictions of the influence of the resonant and non-resonant components. The influence of the resonant and non-resonant effects are estimated and compared. Additionally, the island frequency and width evolution are modelled. From the comparison of the modelling and the experiment, effects caused by the B-coils that are missing in the modelling are identified. To summarised the questions the thesis will address:

- How does a rotating island interact with an externally applied perturbation field in the experiment? What is observed?
- Which effects are dominant, resonant or non-resonant ones?
- Are the observations in agreement with theory and can they be modelled properly?
- What can be concluded from this comparison and are there effects caused by the perturbation fields missing in the modelling based on current theory?

To address these questions this thesis is structured as follows. In chapter 2 the AUG tokamak is presented, with its external heating systems and the diagnostics used for this thesis. In chapter 3 the basic tearing mode theory is described, including the formulae for the island stability and the equation of motion. In addition the theory of the externally applied magnetic perturbation field is introduced. Chapter 4 contains the results of the experimental studies concerning the influence of rotation on the NTM onset. In chapter 5 the influence of externally applied magnetic perturbations on NTMs is discussed. Finally in chapter 6 a general summary is given and an outlook is presented.

Chapter 2

ASDEX Upgrade, Heating systems and Diagnostics

2.1 The ASDEX Ugrade tokamak

This thesis was carried out at the ASDEX Upgrade tokamak (AUG) (**A**xial **S**ymmetric **D**ivertor **EX**periment) [2]. AUG is a medium size divertor tokamak with a major radius of $R_0 = 1.65\,\mathrm{m}$ and a minor radius of $a = 0.5\,\mathrm{m}$. It went in operation in 1990 at the Max Planck-Institut für Plasmaphysik (IPP) in Garching. AUG enables the study of experiments that meet future fusion requirements. Typically the plasmas in AUG are plasmas, which have an elliptical shape and form an X-point, as shown in figure 2.1. In Table 2.1 the main parameters are listed for standard operation scenarios.

At ASDEX Upgrade the toroidal component of the magnetic field is produced by 16 toroidal

major radius R_0	$1.65\,\mathrm{m}$
minor radius a	$0.5\,\mathrm{m}$
working gas	deuterium
tor. magnetic field B_{tor}	$1.8 - 2.6\,\mathrm{T}$
plasma current I_{p}	$0.6 - 1.2\,\mathrm{MA}$
pulse length	$\leq 10\,\mathrm{s}$
energy confinement time τ_{e}	up to $0.2\,\mathrm{s}$
electron density n_{e}	$3 - 10{\cdot}10^{19}\ \mathrm{m}^{-3}$
plasma temperature T	$5\,\mathrm{keV}$
auxiliary heating	max. NBI $20\,\mathrm{MW}$ max. ECRH $4\,\mathrm{MW}$ max. ICRH $7\,\mathrm{MW}$ ohmic$\leq 1\,\mathrm{MW}$

Table 2.1: Basic parameters of ASDEX Upgrade during normal operation

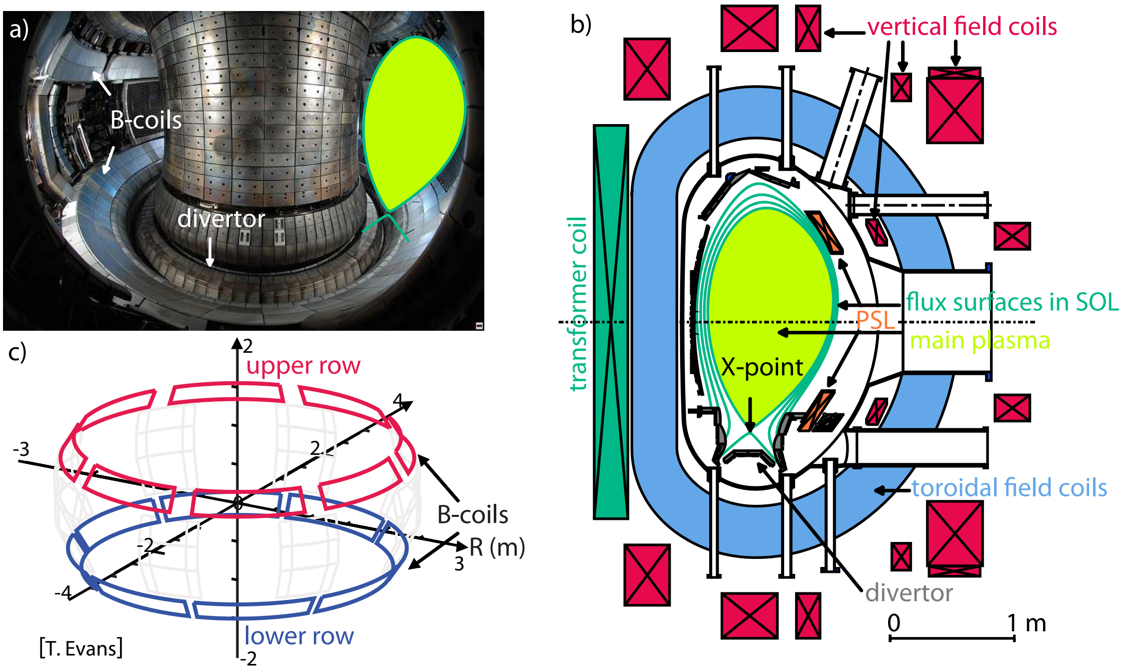

Figure 2.1: (a) A picture of ASDEX Upgrade with the tungsten coated inner wall. The divertor region and the position of the B-coils are indicated. (b) Poloidal cross section of ASDEX Upgrade showing all different coils, the divertor targets and the main plasma. In addition, magnetic surfaces in the scrape of layer (SOL), where the field lines hit the divertor plates and the X-point, are illustrated. (c) 3D view of the active magnetic perturbation coils (B-coils) installed in the vessel of AUG.

field coils. The poloidal magnetic field component is generated by a toroidal current flowing inside the plasma. This plasma current I_p is induced by a transformer coil in the centre of the tokamak. A schematic of the AUG tokamak is shown in figure 2.1. A set of 12 vertical field coils control the plasma position and its shape. The passive stabilising loop (PSL), made out of copper, damps the plasma movement in order to allow a plasma control on a technically feasible time scale of ms. Additionally, 2 vertical field coils are installed to control the plasma position on a time scale in the order of 2 ms. The plasma facing components are completely covered with tungsten. ITER will also have a metallic wall, which is a further aspect why AUG is important for studies concerning future fusion devices.

2.1.1 Magnetic perturbation coils (B-coils)

Since 2012 ASDEX Upgrade is equipped with a set of 16 in-vessel saddle coils, mounted at the low field side of the torus [8, 9, 10]. These coils, called B-coils, are installed in two rows, which consist each of 8 coils, below and above the mid-plane as illustrated in figure 2.1 (c). The B-coils are mounted in front of the Passive Stabilising Loop (PSL), as illustrated in figure 2.1 (a) and figure 2.3 (b). Each coil has five turns. Using these 16 coils a non-axisymmetric magnetic perturbation (MP) field can be produced. This MP field is highest at the edge in front of the B-coils and drops down rapidly. It contains components with a wide magnetic spectrum characterised by toroidal and poloidal mode numbers $B_{\mathrm{B-coils}} = \sum_{n,m} B_{\mathrm{n,m}}$. Due to

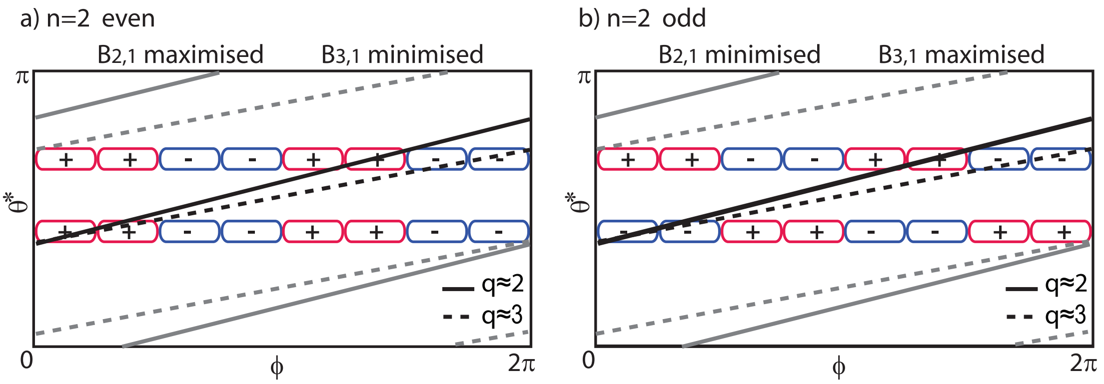

Figure 2.2: Schematic illustration of the alignment of the MP field with the q=2 and q=3 surface for two n=2 B-coil configurations with (a) even and (b) odd parity. The coil position and field lines are mapped in the ($\theta^* - \phi$) plane with θ^* the straight field line angle [11] and ϕ the toroidal angle. The radial field of the coils indicated with a positive/negative coil current points outward/inward. Field lines which cross coils with the same perturbation field direction are aligned and the according MP field component $B_{n,m}$ is maximised.

the regular distribution of the B-coils in the toroidal direction the fundamental toroidal mode number is mainly dominated by the coil pattern. With the 16 coils toroidal mode numbers of n=1,2 or 4 can be generated. Every coil is equipped with an individual power supply, which results in a wide range of different coil configurations being available. Depending on the actual plasma parameters the coil currents (current direction) can be adjusted to produce, a so-called, ‘resonant’ or ‘non resonant’ perturbation field (compare section 3.4). In a ‘resonant’ configuration the resonant MP components are maximised, in a ‘non resonant’ configuration the resonant components are minimised. A resonant component $B_{n,m}$ is a component which has the same helicity as a rational $q = m/n$ surface in the plasma. In a simple picture a resonant MP component is maximal when the corresponding q surface is aligned with the coil pattern. Depending on the q profile and the coil configuration the MP field contains several resonant and non resonant MP components. This is schematically illustrated in figure 2.2 for two different B-coil configurations, both n=2 but different phasing of the upper and lower row ((a) even and (b) odd parity). Two different surfaces inside the plasma (q=2 and q=3) are indicated. For the ‘even’ configuration the perturbation field is aligned with the $q = 2$ surface, hence the $B_{n=2,m=1}$ Fourier component of the MP field is maximal. For the ‘odd’ configuration the $B_{n=2,m=1}$ appears to be minimised, whereas the $B_{n=3,m=1}$ is maximised.
Due to $\vec{j} \times \vec{B}$ forces acting on the coils, their current is restricted to 1 kA at 2.5 T (1.2 kA at 1.8 T) per turn. The produced field is mainly in the radial direction and 10^{-3} smaller than the equilibrium magnetic field. So far, the B-coils can only be used in a static configuration, but a power supply which enables the generation of rotating MP fields is planned. At AUG the B-coils are mainly used for the mitigation of edge localised modes (ELMs), which has been shown successfully in [12, 10]. However, they can also influence the stability of other kinds of MHD activities as described in sections 3.4 and 5.

2.2 Plasma heating

The plasma current, which is induced by a transformer coil in the middle of the torus and is characteristic for a tokamak configuration, produces a poloidal magnetic field and also contributes to the plasma heating, through the ohmic resistance of the plasma [3]. The ohmic heating power density P_{oh} depends on the plasma resistivity η and the plasma current density $\vec{j}$ via $P_{\mathrm{oh}} = \eta j^2$. The resistivity in a plasma scales with $T_{\mathrm{e}}^{-3/2}$. Consequently, the ohmic heating is strongest at low temperatures. Additionally, $\vec{j}$ is limited due to stability requirements. In order to increase the temperature in a tokamak significantly, auxiliary heating methods have to be used.

Three different auxiliary heating systems are available at AUG: the neutral beam injection (NBI), the electron cyclotron resonance heating (ECRH) and the ion cyclotron resonance heating (ICRH). Depending on the requirements, a combination of these heating methods is used in the standard AUG operation. In order to vary the input torque for example a combination of different heating mixes was used in the dedicated discharges that were carried out for the investigation described in section 4. Low input torque and, consequently, low plasma rotation was achieved by combining ECRH and ICRH, while high plasma rotation and counter-current rotation was obtained by applying NBI. An overview of the three heating systems in the AUG geometry is shown in figure 2.3.

2.2.1 Neutral beam injection (NBI)

This heating method is based on the injection of neutral atoms into the plasma. These atoms are ionised due to collisions with plasma particles and are bound to the magnetic field. While gyrating along the field lines the ions, which carry most of the energy, transfer their energy to plasma electrons and ions due to Coulomb collisions. As a consequence the injected ions are slowed down until they are thermalised. This heating method dominantly heats the plasma, but, depending on the injection geometry, it also exerts a torque in the toroidal direction. For the temperature ranges, of ions and electrons, at ASDEX Upgrade, the NBI transfers its energy mainly to the plasma ions due to charge exchange collisions.

Two NBI systems are installed at AUG (see figure 2.3). Each consists of 4 neutral beam sources, which deliver typically in deuterium a total heating power of 20 MW. Both NBI boxes have a similar set up, however, with different extraction voltages and currents, which leads to a full injection energy E_{b} of 60 keV for box 1 and 93 keV for box 2. Each system

Table 2.2: Important parameters of the NBI system at ASDEX Upgrade

	Injector 1	Injector 2
max. extraction voltage (kV)	60	93
max. extraction current (A)	77	63
max. injection energy E_{b} (keV)	60	93
$R_{\mathrm{tang}}(m)$	0.54 / 0.93	0.84 / 1.29

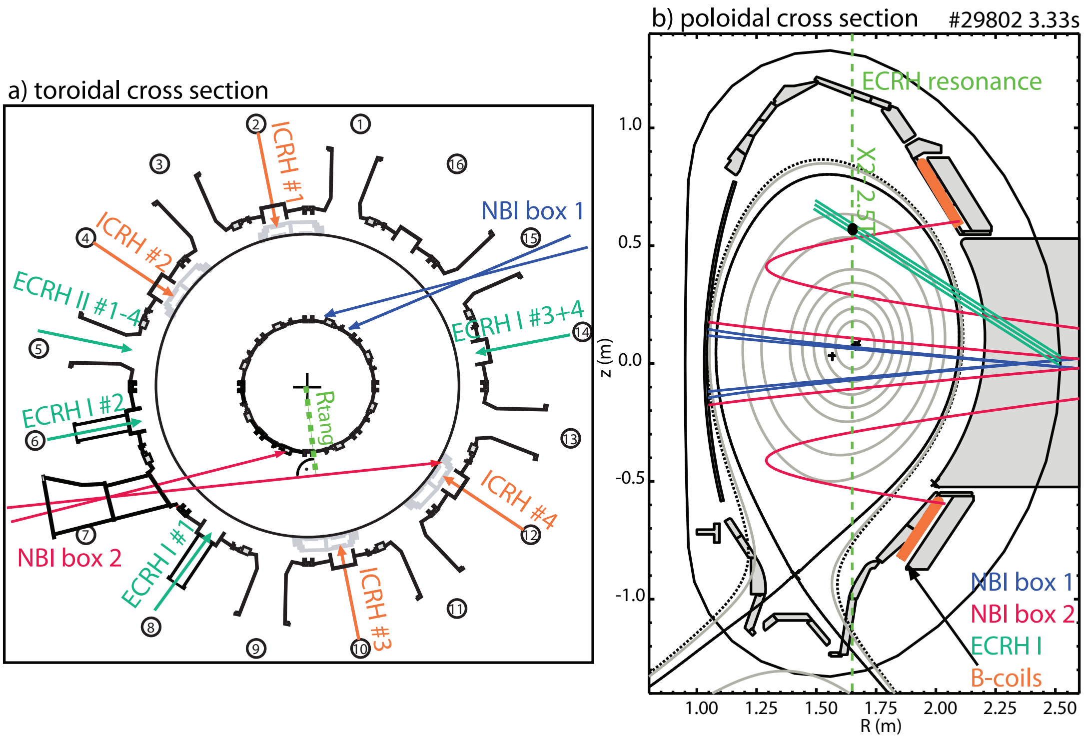

Figure 2.3: (a) Toroidal and (b) poloidal cross section of ASDEX Upgrade where the NBI beams, the ICRH and ECRH locations are shown. As example the tangential radius of one NBI beam is shown, which is needed to calculate the NBI input torque in chapter 4 (equation (4.6)) is shown in the toroidal plane . In the poloidal plane the ECRH I resonance close to the plasma axis for 2.5 T and 140 GHz is illustrated. Along this resonance the ECRH can be deposited at different radial locations, using steerable mirrors. In addition, the position of the B-coils is indicated in the poloidal plane.

is equipped with two beams, which inject the neutral atoms more radially and two which inject more tangentially. The total input torque per beam is around 1-2 Nm depending on the injection angle. Combining different beams of box 1 and 2, the toroidal input torque can be varied depending on the injection angle and the deposition location. An important parameter for the description of the beams, which is needed in section 4.3.1 to calculate the NBI input torque, is the tangential radius, R_{tang}, of each beam which is indicated for one beam in figure 2.3 (a). R_{tang} has the same value for two radial and tangential beams of each injector. All important parameters of the ASDEX Upgrade NBI system are summarised in table 2.2. The NBI source 3 of box 1 is additionally used as a diagnostic beam for charge exchange recombination spectroscopy illustrated in figure 2.4 (compare also section 2.3.7). In the toroidal plane the NBI is injected counter-clockwise, which is in standard operation (compare figure 1.3) in the direction of the plasma current, defined as co-current direction. Reversing the plasma current and the magnetic field (reversed $I_{\mathrm{p}}/B_{\mathrm{tor}}$ operation), the NBI is injected in counter-current direction. With this counter-current rotation can be achieved.

2.2.2 Electron cyclotron resonance heating (ECRH)

Electron cyclotron resonance heating (ECRH) is a wave heating method for electrons. Radio frequency waves in the frequency range of 140 GHz (105 GHz) are launched into the plasma, which accelerate the plasma electrons. These electrons then heat the plasma, due to collisions with the plasma particles. The resonance location is determined by the electron cyclotron frequency ω_{ce}, which depends on the magnetic field

$$\omega_{\mathrm{ce}} = \frac{eB_{\mathrm{tot}}}{m_{\mathrm{e}}}. \tag{2.1}$$

Here e is the elementary charge, B_{tot} the total magnetic field ($\simeq B_{\mathrm{tor}}$) and m_{e} the electron mass. In a tokamak B_{tor} decreases with $1/R$, R being the major radius, from the plasma centre to the edge (see figure 1.3 (b)), which results in a local deposition of the ECRH heating power. At AUG the second harmonic in X-mode is used. At 2.5 T and a given frequency of 140 GHz, the ECRH resonance is close to the magnetic axis at around R=1.65 m, as shown in figure 2.3 (b). Similar to the ECE diagnostic, the ECRH operation is limited by the ‘cut-off’ and the ‘shine through’ (see section 2.3.2), which, in the worst case, damage the in-vessel components.

To date, the ECRH consists of two systems. The old system uses 2 pairs of each two gyrotrons at 140 GHz which deliver 2 MW for 2 s. The new system consists of 4 individual gyrotrons which can be used at 140 GHz and 105 GHz for 10 s with around 1 MW each. The angle under which the power is injected into the plasma can be adjusted in the poloidal and toroidal direction for each transition line. This provides the opportunity to deposit the heating power at different radial locations at the same time. An advantage of the ECRH system is that the heating power can be deposited locally. In contrast to the NBI heating the ECRH heats the plasma without any torque input. However, applying ECRH leads to a decrease of the plasma rotation [13, 14, 15, 16], caused by changes in the electron and ion temperature profiles which lead to a change in the turbulent transport. Similar considerations hold for the ICRH.

2.2.3 Ion cyclotron resonance heating (ICRH)

A second wave heating method is the ion cyclotron resonance heating which heats the plasma with frequencies in the ion cyclotron frequency regime. The ion cyclotron waves at a frequency of around 30 to 120 MHz are coupled via antennas into the plasma. The waves propagate through the plasma and are absorbed at the position of the resonance depending on the ion cyclotron frequency

$$\omega_{\mathrm{ci}} = \frac{ZeB_{\mathrm{tot}}}{m_{\mathrm{i}}}, \tag{2.2}$$

with Z the atomic number and m_{i} the mass of the main ions. At ASDEX Upgrade the ICRH system consists of 4 generators. These generators are connected to 4 2-strap-antennas which are operated in pairs. The system can launch a heating power of up to 7 MW into the plasma. The ICRH heats the plasma ions and electrons, and, like the ECRH, it exerts no torque onto the plasma.

2.3 Diagnostics

In this section the basic principles of the diagnostics used in this thesis are presented. Radial profiles of characteristic parameters like the electron and ion temperature (T_e and T_i), the electron density n_e and the toroidal plasma rotation v_{tor} have been used to investigate the parameter dependences of NTMs in section 4. Diagnostics like the magnetic measurements (pick-up coils), the Soft X-Ray diagnostic and the electron cyclotron emission radiometry are useful tools to detect MHD events and afterwards analyse their structure like the toroidal and poloidal mode number or to determine their radial location. In figure 2.4 a poloidal and a toroidal cross section of AUG is shown, where the measurement position of the diagnostics used are indicated.

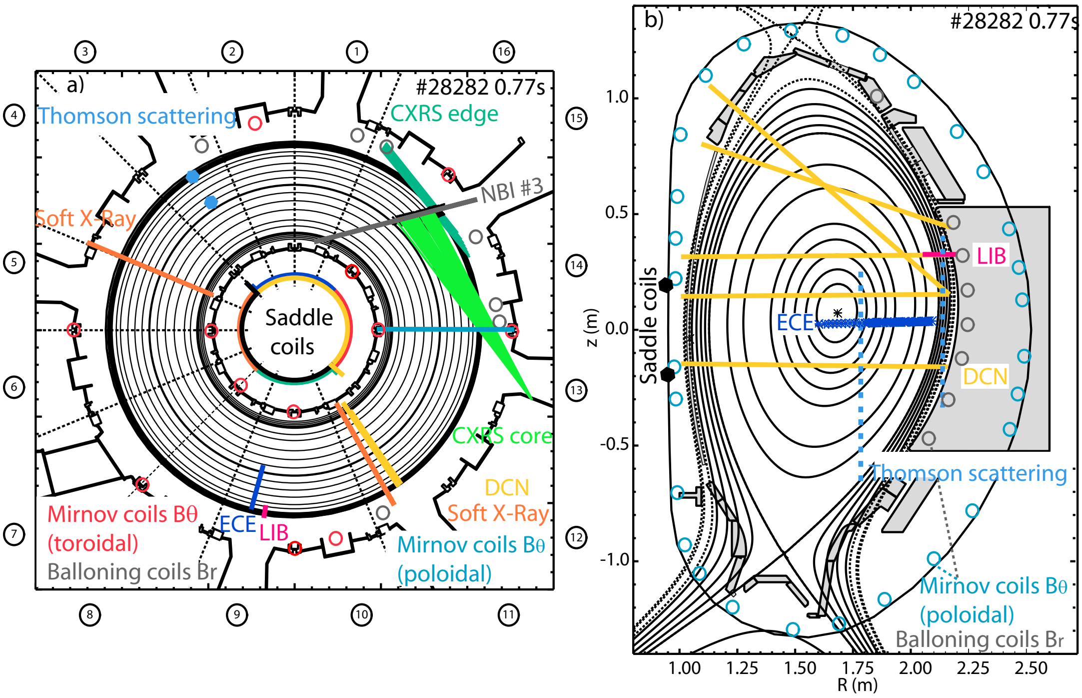

Figure 2.4: (a) Toroidal and (b) poloidal cross section of ASDEX Upgrade, where the measurement locations of all diagnostics used in this thesis are indicated.

2.3.1 Equilibrium reconstruction

In a tokamak one important tool is the reconstruction of the magnetic equilibrium. It contains the information of the structure of the nested magnetic flux surfaces, which is important for the analysis of MHD modes as well as for the mapping of diagnostics at different positions in the toroidal and poloidal plane. The equilibrium reconstruction is done using codes like CLISTE [17], which solves the Grad-Shafranov equation including different constraints either from theory or from measurements. The Grad-Shafranov equation is the differential equation for the poloidal flux function Ψ for an axi-symmetric equilibrium. Usually only magnetic measurements are included in the calculation, however, in dedicated studies also kinetic profiles, like the electron and ion density and temperature, can be taken

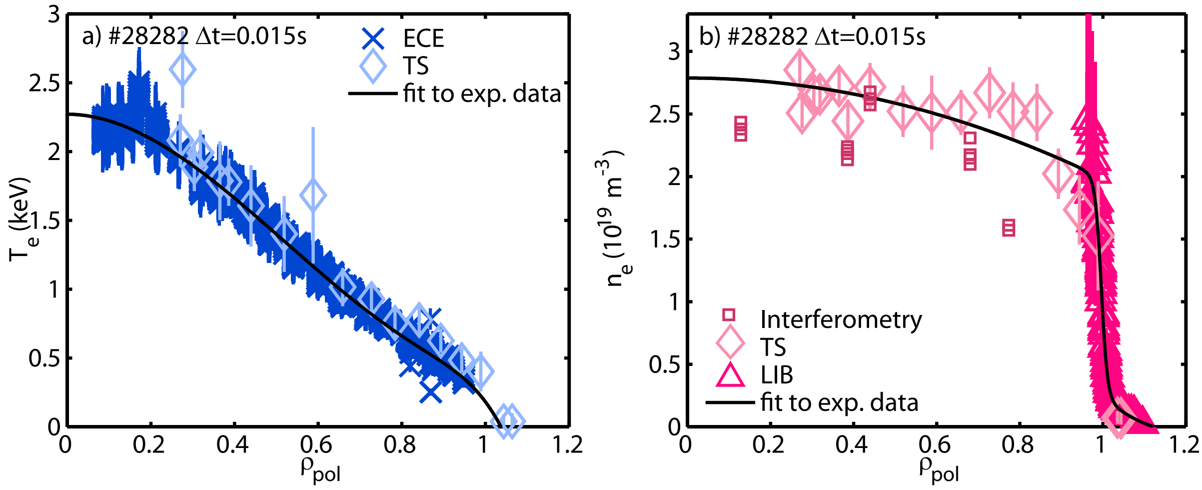

Figure 2.5: (a) Electron temperature profile measured with ECE and Thomson scattering. (b) Electron density profile measured with Thomson scattering and the lithium beam diagnostic. Also the line integrated density from interferometry is shown.

into account to prescribe the pressure profile [18]. The calculation effort increases with the number of constraints. This is the reason why the latter method is only applied for dedicated discharges. The generic equilibrium reconstruction delivers good results for the edge region, whereas the uncertainties towards the core region increase significantly.

From the equilibrium reconstruction a poloidal flux matrix in the poloidal cross-section can be evaluated, which allows the calculation of radial coordinates depending on the poloidal flux as ρ_{pol} (see equation (1.8)). Additionally, one gets the q profile, which is an important parameter for the analysis of MHD events. Unfortunately, in most of the cases the reliability of q in the core is insufficient for the determination of gradients dq/dr. It is also difficult to localise MHD modes from the q profile alone.

2.3.2 Electron cyclotron emission (ECE)

One of the routinely used diagnostics to measure the T_{e} profile at ASDEX Upgrade is the Electron Cyclotron Emission radiometry (ECE) which is a passive technique (figure 2.5 (a)). In a tokamak electrons gyrate in the presence of the applied magnetic field and emit electromagnetic radiation. This radiation is emitted at the characteristic electron cyclotron frequency ω_{ce} and its low n harmonics. This radiation frequency is proportional to the magnetic field strength B

$$\omega = n\omega_{\mathrm{ce}} = n\frac{eB_{\mathrm{tot}}}{m_{\mathrm{e}}}. \tag{2.3}$$

Since B_{tot} is dominated by the toroidal magnetic field B_{tor}, which depends on $1/R$, the emitted frequency can be associated with a distinct radial position R and a spatially resolved measurement is possible

$$\omega \approx n\frac{eB_0R_0}{m_{\mathrm{e}}R}. \tag{2.4}$$

The magnetic field B_0 is the toroidal magnetic field at the plasma centre R_0.
Normally the plasma is optically thick for the electron cyclotron frequency and its low harmonics. Then it behaves like a black body and follows the Planck curve. The electron emission in plasmas occurs at long wave length, therefore, the intensity distribution $I_n(\omega)$ can be described by the Rayleigh-Jeans law. In this case, the radiation temperature reflects the electron temperature

$$I_n(\omega) = \frac{\omega^2 T_\mathrm{e}}{8\pi^3 c^2}, \tag{2.5}$$

where c is the speed of light. At low densities especially at the edge, the plasma is optically thin and the assumption of a black body is not valid. According to this, the measured radiation temperature is not the local electron temperature anymore [19]. This phenomenon is called 'shine-through'. Another limitation of the ECE is the so-called 'cut-off' [20]. Only waves with a frequency higher than the cut-off frequency can propagate in the plasma otherwise they are reflected inside the plasma volume and do not reach the receiver at the plasma edge. Since the cut-off density (for extraordinary modes (X-mode)) depends on ω_ce and the plasma frequency ω_p $(=\sqrt{n_\mathrm{e} e^2/\epsilon_0 m_\mathrm{e}})$, this sets an upper limit for the density and a lower limit for the magnetic field.
At AUG the second harmonic extraordinary mode (X-mode) is used for the T_e measurements. The diagnostic system is a multichannel heterodyne receiver which allows ECE measurements at frequencies between 89 GHz and 187 GHz, corresponding to local magnetic fields from 1.6 T to 3.4 T. It has 60 channels, which measure at different frequencies and deliver radially distributed measurements, as shown in figures 2.4 and 2.5. The standard time resolution is 32 kHz with a spatial resolution of around 1 cm. A newly installed acquisition system provides an even higher time resolution of up to 1 MHz.

2.3.3 Thomson scattering diagnostic (TS)

Another routinely used diagnostic at ASDEX Upgrade is the Thomson scattering (TS) diagnostic, shown in figure 2.4. With this active method the electron temperature T_e and density can be measured, as illustrated in figure 2.5. A laser beam is launched through the plasma. The laser light accelerates free electrons in the plasma, due to $m_\mathrm{i} >> m_\mathrm{e}$, which act as dipoles and radiate. The scattered laser wave is two times Doppler shifted due to the movement of the free electrons relative to the incident wave $(\vec{k}_\mathrm{in})$ and the scattered wave $(\vec{k}_\mathrm{out})$

$$\Delta\omega = (\vec{k}_\mathrm{in} - \vec{k}_\mathrm{out})\vec{v}. \tag{2.6}$$

From the degree of Doppler broadening of this incoherent scattered light T_e can be determined. Additionally, the intensity is proportional to the electron density n_e, which enables a simultaneous measurement of T_e and n_e. In tokamaks the TS detectors are usually located at a scattering angle of 90°. At ASDEX Upgrade a core and an edge TS system are installed (figure 2.4) [21]. Both systems (core (edge)) use a multi pulse Nd:YAG laser (neodymium yttrium aluminium garnet) which is vertically launched through the plasma with a repetition rate of 20 Hz. The scattered light is spectrally analysed and detected by 16 (10) four channel polychromators equipped with avalanche photo diodes. Interference filters are additionally installed in front of the detectors, which suppress efficiently the direct laser light. The TS systems deliver T_e and n_e profiles every 12.5 ms (8.3 ms) with a radial resolution of 25 mm (3 mm).

2.3.4 Lithium Beam (LIB)

The electron density profile (n_e profile) at the edge can be measured with the lithium beam impact excitation spectroscopy diagnostic (figure 2.5 (b)). A neutral lithium beam is injected horizontally into the plasma and the LiI(2p→2s) resonance line at 670.8 nm is measured [22, 23]. The injected lithium atoms collide with the plasma particles and the lithium atoms get excited. As a consequence, the measured line emission intensity depends on the plasma density. However, the beam is additionally attenuated due to ionisation and charge exchange processes, which leads to a restriction of this method to the edge region ($\rho_\mathrm{pol}>0.95$). The electron density can be calculated from the emission profile via a collisional-radiative model. This model includes electron-impact excitation, ionisation and charge exchange processes.
At ASDEX Upgrade the lithium atoms are injected into the plasma near the horizontal mid plane (figure 2.4) with an energy of 30-60 keV and a current of around 2-4 mA. The spatial resolution of around 5 mm is determined by the aperture of the optical setup. Optical fibres transfer the light to the acquisition system which consists of interference filters and photo multipliers. Usually a temporal resolution of 5-20 ms is chosen. In special cases, for example to measure fast transient events, the time resolution can be increased to 50 µs. To subtract the background radiation from the measured signal the beam is chopped periodically, 56 ms beam on and 24 ms beam off [24].

2.3.5 Interferometry

A third method to measure the electron density n_e is laser interferometry (figure 2.5 (b)). This method is based on the interaction of an electromagnetic wave with the plasma electrons due to refraction. If the frequency of the laser ω_0 is higher than the plasma frequency ω_p, the refraction index N of the plasma depends on the density

$$N = \sqrt{1 - \frac{\omega_\mathrm{p}^2}{\omega_0^2}} \approx 1 - \frac{\omega_\mathrm{p}^2}{2\omega_0^2} = 1 - \frac{e^2}{2\epsilon_0 m_\mathrm{e} \omega_0} n_\mathrm{e}, \tag{2.7}$$

A laser crossing the plasma undergoes a phase shift ($\Delta\phi$) along its way l through the plasma, depending on the line integrated density

$$\Delta\phi \approx \frac{e^2}{2c\epsilon_0 m_\mathrm{e} \omega_0} \int_l n_\mathrm{e} dl. \tag{2.8}$$

The phase difference $\Delta\phi$ can be determined, via interferometry, by comparing the phase of a wave, which propagates through the plasma, to the phase of a wave which propagates through vacuum. As shown in 2.8, the density measured with interferometry is not spatially

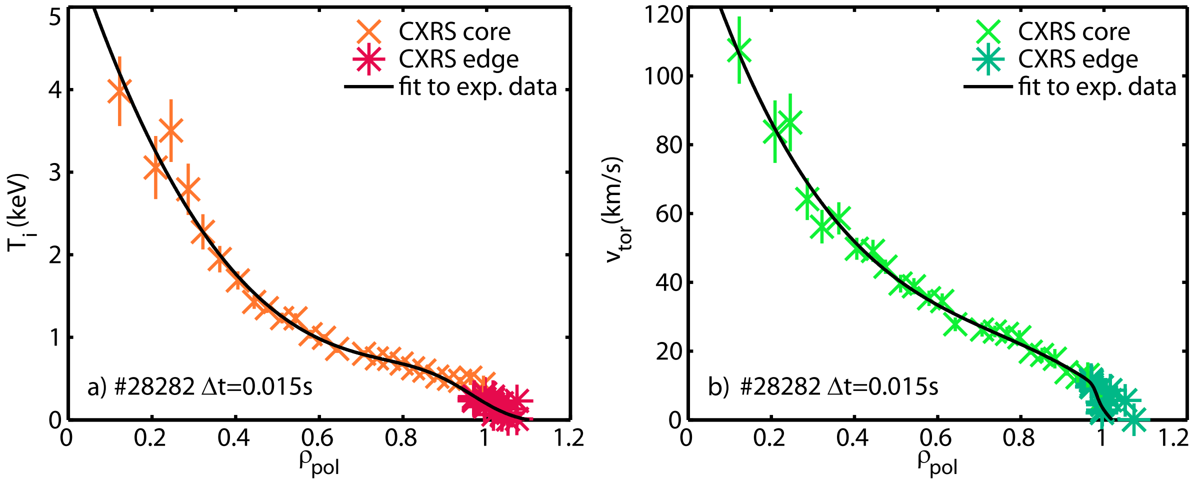

Figure 2.6: (a) Ion temperature and (b) toroidal velocity profile of the impurity ions measured with CRXS.

resolved. However, using different lines of sight the density profile can be reconstructed via inversion algorithms. At AUG a DCN laser at 195 µm is used and a phase modulated Mach-Zehnder-type interferometer with a heterodyne detection system to measure the phase shift [25]. Five lines of sight are installed at different radial locations as illustrated in figure 2.4. The beams cross the plasma, are reflected at mirrors at the inner column, cross the plasma again and leave the vessel at almost the same position as they entered. The temporal resolution of the system is 300 µs. This diagnostic is often used to get a quick overview of the temporal evolution of the density and especially of differences in the temporal behaviour of the core and the edge region using different lines of sight.

2.3.6 Integrated data analysis (IDA)

At AUG also a combined analysis of the ECE, the TS, the LIB and the interferometry data is possible [26]. This integrated data analysis (IDA) provides T_e and n_e profiles via forward modelling with the constrain to match the raw measured signals of the included coherent diagnostics. With this analysis method the individual interpretation and analysis of all different measured data can be replaced by one combined analysis. Additionally the profile quality can be improve.

2.3.7 Charge exchange recombination spectroscopy (CXRS)

A common method to measure the ion temperature T_i and the rotation velocity of impurity ions in the toroidal and poloidal direction (v_tor and v_pol) is charge exchange recombination spectroscopy (CXRS) (figure 2.6). This diagnostic uses the analysis of spectral light emitted by low Z impurity ions (Z is the atom number) due to charge exchange collisions with a neutral ion in the plasma.

In a typical fusion plasma low Z impurity ions are fully stripped and do not emit line radiation. In the cross-section with a neutral beam, which is one of the heating beams at ASDEX Upgrade (see figure 2.4), these low Z impurity ions collide with the neutral ions and receive an electron. The recombined impurity ions are in an excited state and in the following subsequent de-excitation, they emit line radiation at a characteristic wave length, which can be observed with spectrometers. These measured spectra contain local information on the impurity ions. The Doppler width of the measured spectra is proportional to the ion temperature while the rotation velocity of the impurity ions can be obtained from the Doppler shift. Additionally, the density of the impurities can be determined from the radiance of the measured spectral line.

At ASDEX Upgrade several charge exchange systems with poloidal and toroidal views are installed at the high and at the low field side [27]. In this work mainly one of the toroidal core systems was used with a radial and temporal resolution of about 2.0 cm and up to 3.5 ms, respectively.

2.4 Analysis tools for MHD activities

2.4.1 NTM detection and mode number analysis with Soft X-ray radiation (SXR)

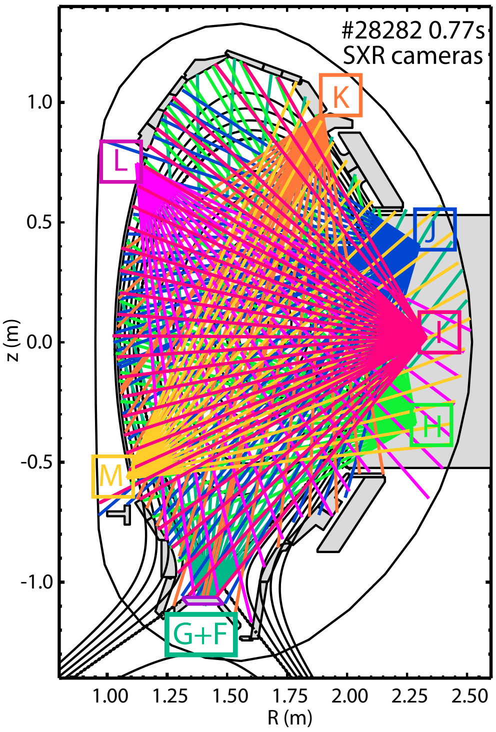

Figure 2.7: Poloidal cross section, where all lines of sight of the SXR cameras are indicated.

The Soft X-ray (SXR) diagnostic is an ideal tool to investigate MHD activities in the plasma, especially in the core. MHD instabilities in the plasma cause changes in the emitted SXR radiation, which can be detected via pinhole SXR cameras. At ASDEX Upgrade 8 pinhole cameras are installed, which are equipped with 75 µm curved beryllium filters. The installed lines of sight cover the whole plasma volume as illustrated in figure 2.7. This diagnostic can be used to determine the mode frequency and the poloidal mode number, but it also provides information on the radial location of MHD events. A tomographic reconstruction additionally provides further information on the mode structure [28]. The poloidal mode number and the location of the modes can be determined from the signal of only one camera. In this thesis the SXR diagnostic is mainly used to analyse 1/1 modes. In figure 2.8, an example is illustrated for the I-camera. The I-camera is situated at the low field side and covers the whole plasma, but it is mainly focused on the central region of the plasma, as illustrated in figure 2.7 (red). The 1/1 mode can be detected via a spectrogram of one central channel of the I-camera, as illustrated in figure 2.8 (a). The raw SXR signal is Fourier decomposed. In figure 2.8 the spectrum contains only one dominating frequency and some harmonics, which correspond to the analysed 1/1 mode (fig. 2.8 (c)). The FFT amplitude of the selected frequency has a modulation minimum around the centre (figure 2.8 (d)) and two maxima on the left and the right hand side. At the same time a phase jump of π is observed at the location of the minimum in the amplitude (figure 2.8 (e)). This is the typical signature of an $m = 1$ mode [29], which passes the lines of sight with its single O- and single X-point. In figure 2.8 (b) a 1/1 mode is illustrated in three different phases together with three example lines of sight of camera I. From figure 2.8 (b) it is obvious that the blue and green line detect a large amplitude oscillation due to the rotating mode, which corresponds to a maximum in the amplitude modulation (2.8 (d)). Additionally, when the blue line detects a maximum the green line sits in an emissivity minimum, which corresponds to a phase shift of those two lines of around π, shown in 2.8 (e). At the same time the red line measures almost the same emissivity during all three phases, which corresponds to an amplitude modulation of almost zero (fig. 2.8 (d)). As indicated in figure 2.8 (d), the edges of the amplitude distribution determine the position of the mode, which is the $q = 1$ surface in this example. This explains the characteristic signals of a 1/1 mode, whereas for higher mode numbers similar considerations can be made. In general, for peaked emissivity profiles, the number of minima in the FFT amplitude corresponds to the poloidal mode number, if at the same position a phase jump is observed. The toroidal mode number was confirmed using the magnetic signals (compare next section 2.4.2).

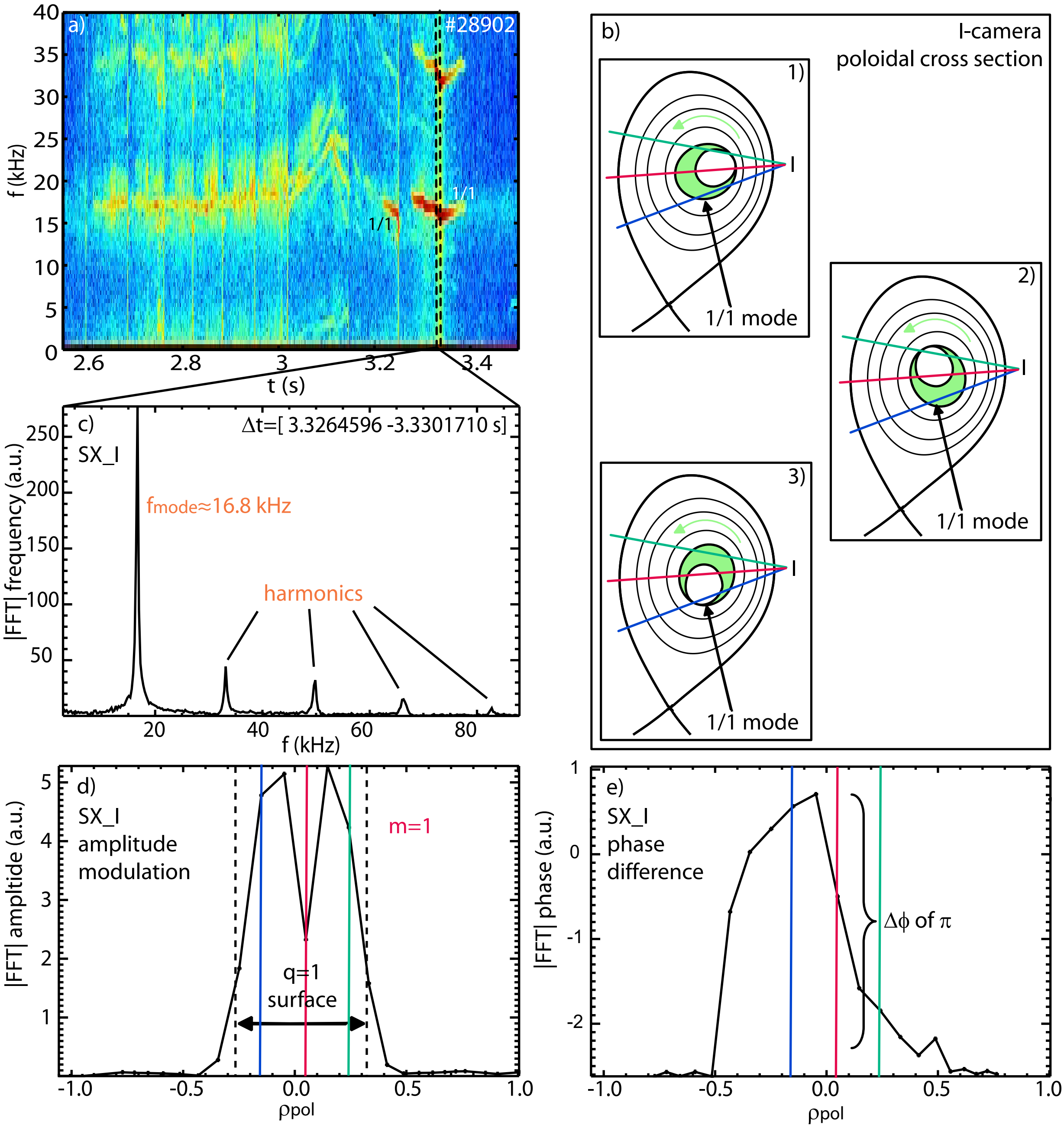

Figure 2.8: Schematic of the determination of the poloidal mode number of an m=1 mode via the SXR diagnostic: (a) Spectrogram of one SXR channel, (b) 1/1 mode during three different phases together with three example line of sight of camera I in a poloidal cross section , (c) Fourier analysis of raw signal, where mode frequency and harmonics are clearly visible (d) amplitude modulation corresponding to selected frequency and (e) phase from FFT.

2.4.2 NTM detection and mode number analysis with magnetic measurements

AUG is equipped with a large set of pick-up coils (38 Mirnov and 36 ballooning coils) located all around the torus. These coils detect changes in the poloidal ($\dot{B}_{\rm pol}$) and radial ($\dot{B}_{\rm r}$) magnetic field, respectively. The locations of the Mirnov and ballooning coils in the toroidal and poloidal plane are indicated in figure 2.4. These coils are able to detect even small B-field perturbations everywhere inside the plasma, provided they rotate in the laboratory frame fast enough. Therefore, these coils are an ideal tool to detect and study MHD activities. From a single coil signal the mode frequency and amplitude can be determined. The time evolution of a mode amplitude can be depicted in a spectrogram, illustrated in figure 2.9 (a). This is an easy way to get an overview of the MHD activity present in the plasma.

A Fourier decomposition of the raw data, as shown in figure 2.9 (d), gives information about the different modes present in the plasma at one specific short time interval. In this short time interval (figure 2.9 (c)) for one selected frequency (figure 2.9 (d)) the toroidal (n) and poloidal (m) mode numbers can be determined, via the phase differences of several coil signals, which are distributed in toroidal or poloidal direction. The measured phase difference of a mode $\Delta\alpha$ in toroidal direction is $n\Delta\phi$. For given coil positions the toroidal mode number n can be determined via $n = \Delta\alpha/\Delta\phi_{coil}$, and similarly for the poloidal mode number m. This is shown schematically in figure 2.9 (e).

Taking the filtered coil signal, which contains the information of only one selected frequency, and following the points of similar phase, e.g. the minima, from coil to coil gives information on the toroidal mode number (n). The number of minima, in this case 2, which fit into one toroidal turn (360°), determine n. The same principle holds for m, which can be determined from different poloidally distributed pick-up coils. However, the determination of m is not as robust as the one of n, due to the different field line angles along the poloidal angle θ. This has to be taken into account in the analysis in order to get correct results, which at the same time implies that the equilibrium reconstruction has to be reliable.

2.4.3 NTM localisation due to $T_{\rm e}$ fluctuations

In section 2.3.2 the basic principle of the $T_{\rm e}$ measurements via the ECE diagnostics has been discussed. The ECE can additionally be used to determine the location of MHD events in the plasma and is especially used for the localisation of NTMs.

Normally an island is rotating in the toroidal direction with respect to the location of the locally fixed ECE resonances. This leads to a $T_{\rm e}$ profile flattening inside the island when the O-point is passing, while $T_{\rm e}$ is almost unperturbed, with normal gradients, at the X-point. The ECE channels detect these $T_{\rm e}$ fluctuations due to the island's X- and O-points passing by. The fluctuation amplitude is different for every radial channel across the island and has two maxima close to the island's separatrices (see figure 3.1). Additionally, a phase reversal is observed at the position of the fluctuation minimum. So the island location can be determined by the position of the flattening in the $T_{\rm e}$ profile, accompanied with a minimum in the $T_{\rm e}$ fluctuations and a phase shift of π at the same position, illustrated in figure 2.10.

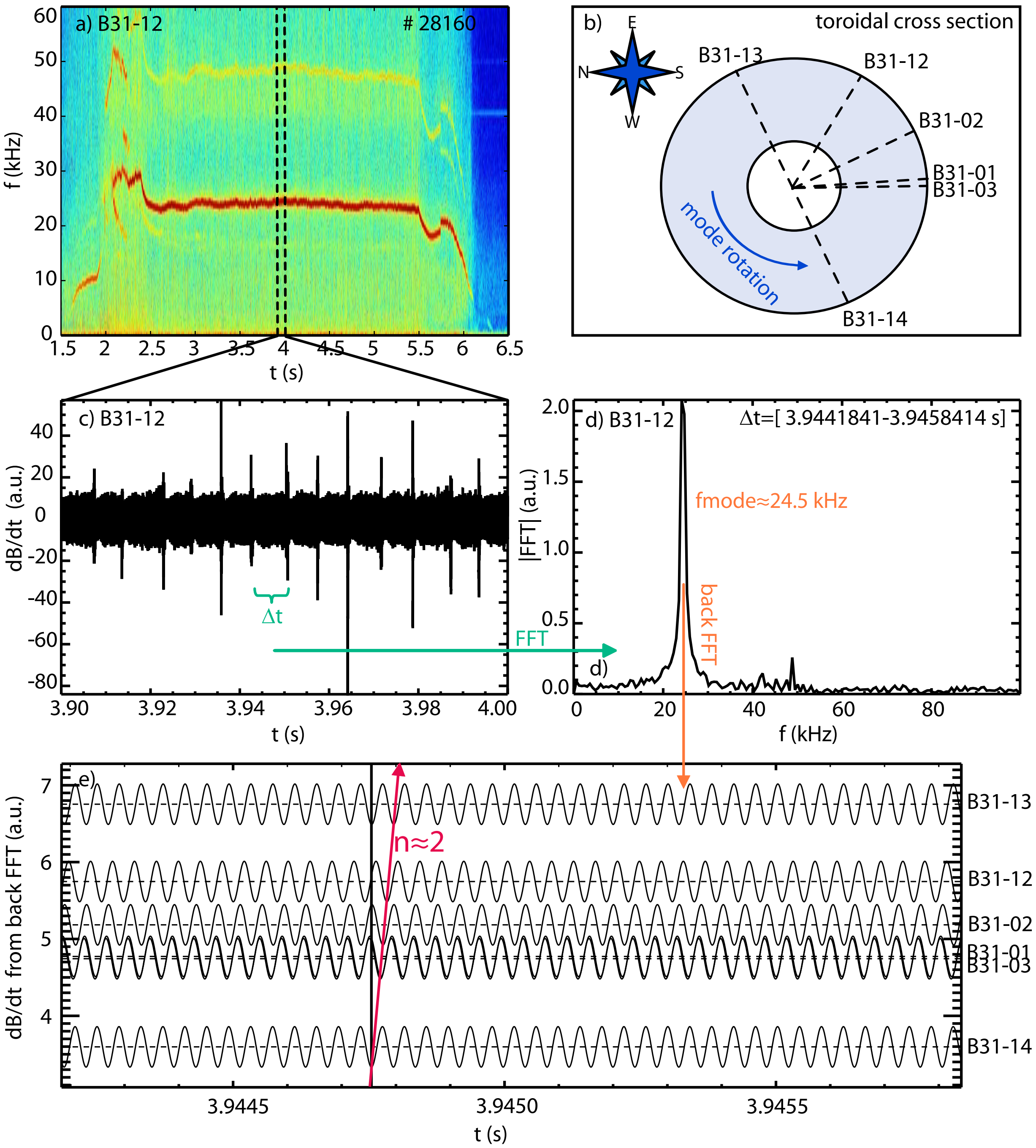

Figure 2.9: Schematic of the determination of the toroidal mode number of an n=2 mode via the pick-up coils ($\dot{B}_\mathrm{r}$) at the edge of the plasma: (a) Spectrogram of one pick-up coil, (b) set of toroidally distributed pick-up coils in the toroidal plane used for the analysis, (c) raw signal of one pick-up coil while the $n = 2$ mode is present, (d) Fourier analysis of the raw signal, where the mode frequency is clearly visible and (e) back FFT of the frequency filtered signal which contains only the modulation due to the specific mode. The red line connects the points, which have the same phase for the different coils in toroidal direction. Two coils which are located 180° apart from each other detect the same phase. Thus, the toroidal mode number n is equal to 2.

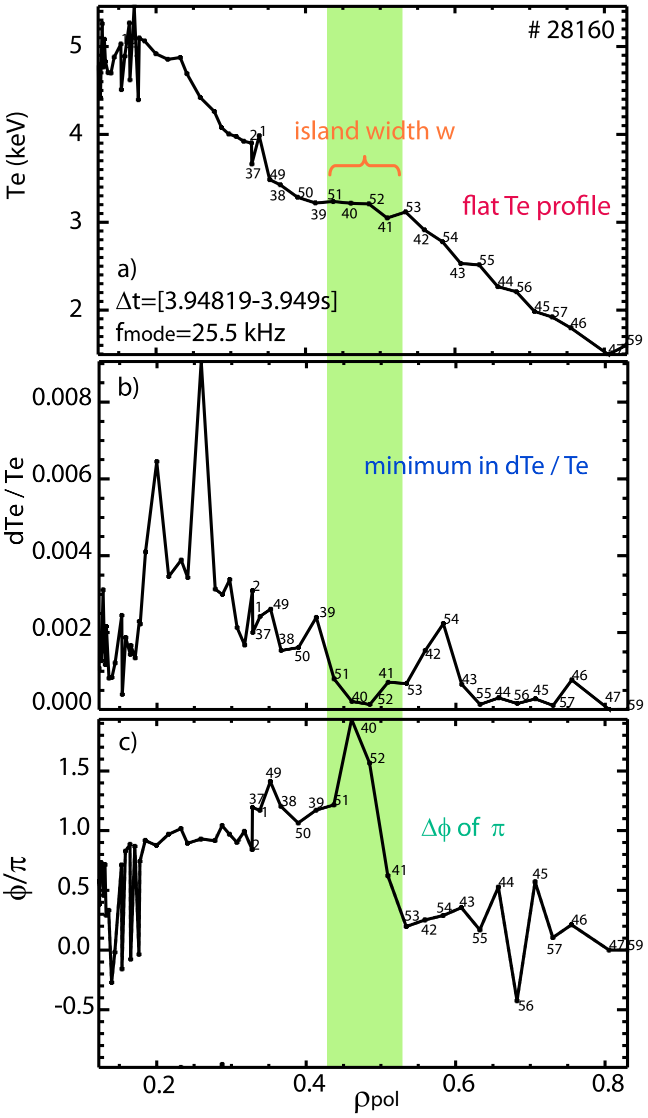

Figure 2.10: Schematic of the determination of the island location via (a) a flattening of the T_e profile, (b) a corresponding fluctuation minimum and (c) a phase shift of π at the same position in the ECE signals.

2.4.4 NTM localisation with a correlation of T_e and dB_{pol}/dt

A more advanced method to determine the NTM location is the ECE correlation analysis. This method is based on the same idea as described in section 2.4.3. It was mainly developed for the NTM stabilisation experiments with ECCD (electron cyclotron current drive) [30]. This method is based on the cross correlation of a combined signal of different toroidally distributed Mirnov coils ($\dot{B}_{pol}$) and the radial channels of the fast ECE with a sampling rate of 1 MHz, as introduced in section 2.3.2. The cross correlation of the magnetic signal and the ECE channels detects a phase jump of π in between the island's separatrices, while at the same position a local minimum in the ECE fluctuations is detected. The used correlation technique is very robust and the NTM localisation can be reliably determined despite additional noise, that can arise due to radiation or other perturbations and fluctuations present in the plasma. The results delivered by this method are presented in figure 2.11.

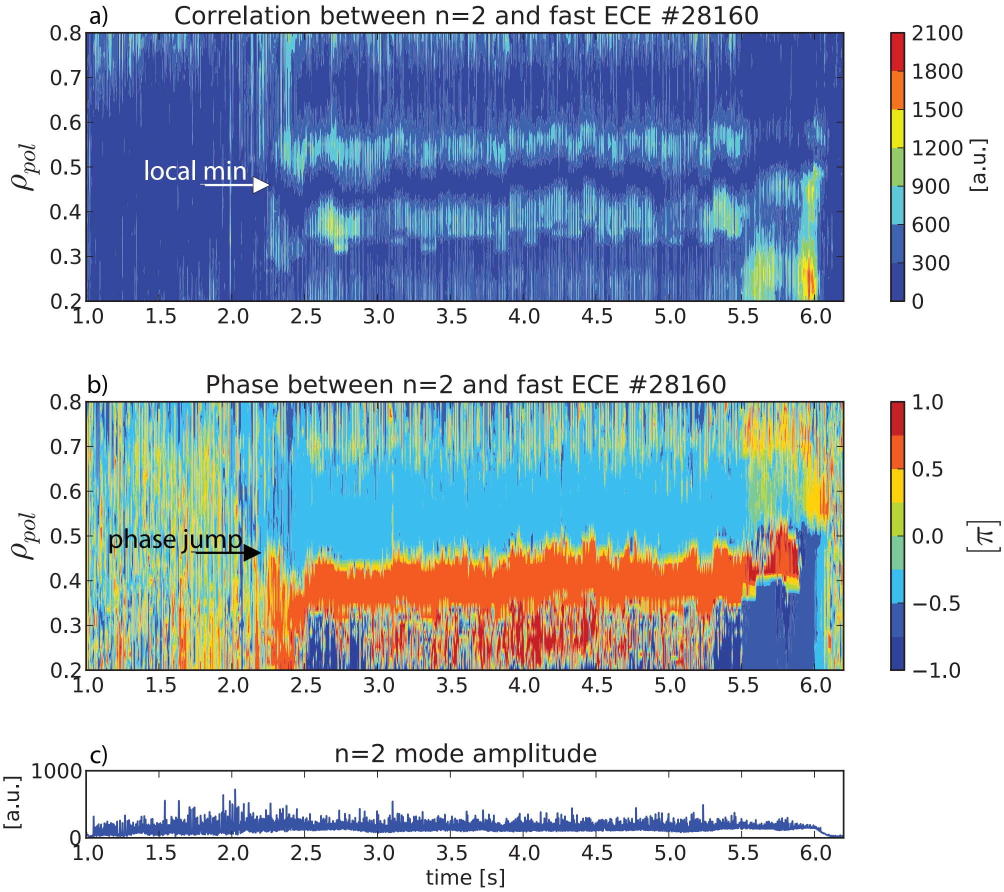

Figure 2.11: (a) Correlation amplitude of the Mirnov coil signal and the ECE. The local minimum is clearly visible. (b) Phase between the ECE and the Mirnov coil signals. The location of the phase jump of π agrees with the location of the local minimum in (a). (c) Estimation of the island size of a n=2 NTM via a combined Mirnov signal.

2.4.5 Locked mode detection

Locked NTMs which are not rotating anymore can no longer be detected with the standard pick-up coils at the plasma edge. For this purpose two independent systems of saddle coils are installed at the high field side of AUG, which are able to detect locked $n = 1$ modes (figure 2.4) [31]. These systems are mainly used as locked mode detectors, to be able to ramp down the plasma before a disruption occurs. The new system consists of two pairs of saddle coils shifted around 90° with respect to each other. The old system consists of only one pair, as illustrated in figure 2.4 (yellow and black). The time-integrated signal of each coil corresponds to the temporal variation of the radial magnetic field perturbation. The difference of the signal of two opposite coils cancels out the $n = 2$ components and gives information about the radial perturbation field of the $n = 1$ modes. With the combined signal of two coil pairs ('ew' east-west coil signal and 'ns' north-south coil signal) [31]

$$B_{\mathrm{r}}^{\mathrm{ew}} = \int \left(\frac{dB_{\mathrm{r}}^{\mathrm{e}}}{dt} - \frac{dB_{\mathrm{r}}^{\mathrm{w}}}{dt} \right) dt \tag{2.9}$$

$$B_{\mathrm{r}}^{\mathrm{ns}} = \int \left(\frac{dB_{\mathrm{r}}^{\mathrm{n}}}{dt} - \frac{dB_{\mathrm{r}}^{\mathrm{s}}}{dt} \right) dt, \tag{2.10}$$

the amplitude $\delta B_{\mathrm{r}}^{n=1}$ and the position/phase α of a locked mode at the high field side (HFS) can be determined [31]

$$\delta B_{\mathrm{r}}^{n=1} = \sqrt{\left(B_{\mathrm{r}}^{\mathrm{ew}}\right)^2 + \left(B_{\mathrm{r}}^{\mathrm{ns}}\right)^2} \tag{2.11}$$

$$\alpha^{\mathrm{HFS}} = \arctan\left(\frac{B_{\mathrm{r}}^{\mathrm{ns}}}{B_{\mathrm{r}}^{\mathrm{ew}}} \right). \tag{2.12}$$

Chapter 3

Theory of magnetic islands

In magnetically confined plasmas a large set of instabilities is observed. One group is the magneto hydrodynamic (MHD) instabilities. In MHD theory the plasma is described as a gas of charged particles. These particles are reacting to magnetic ($\vec{B}$) and electric ($\vec{E}$) fields according to Ampère's and Faraday's law, respectively:

$$\nabla \times \vec{B} = \mu_0 \vec{j} \tag{3.1}$$

$$\nabla \times \vec{E} = -\frac{\partial \vec{B}}{\partial t}, \tag{3.2}$$

with μ_0 the magnetic constant and $\vec{j}$ the current density. The plasma fluid can thus be described by the balance of the pressure gradient and the Lorentz force, yielding the momentum equation:

$$\rho \left(\frac{d\vec{v}}{dt} \right) = -\vec{\nabla} p + \vec{j} \times \vec{B}, \tag{3.3}$$

with ρ the mass density of the plasma, $\vec{v}$ the velocity of the plasma fluid and d/dt the derivation $\partial/\partial t + \vec{v} \cdot \nabla$. The electric field $\vec{E}$ can be linked to the other variables via Ohm's law

$$\vec{E} + \vec{v} \times \vec{B} = \eta \vec{j}, \tag{3.4}$$

with η the plasma resistivity. In the ideal MHD theory the plasma is assumed to be ideally conducting and η is set to zero.

According to this, MHD instabilities in particular can be classified into ideal and resistive MHD instabilities, where only the latter ones are accompanied with changes in the magnetic topology due to finite resistivity. One of the most common resistive MHD instabilitiy in a tokamak is the tearing mode. Due to their characteristic changes in topology these instabilities are also called magnetic islands. Magnetic islands are current driven instabilities[2], whose evolution can be described by the modified Rutherford equation, resulting from MHD theory. They grow slowly compared to ideal instabilities on the resistive time-scale τ_{res}, which is in the range of ms in ASDEX Upgrade.

---

[2] In a tokamak, (part of) the drive is also given by the non-linear pressure perturbation in fact by the island itself, as explained in section 3.2.2

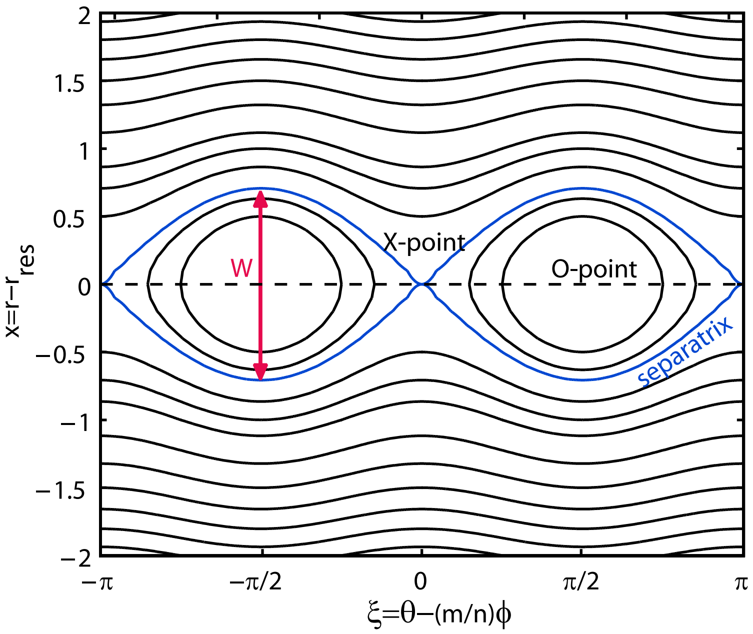

Figure 3.1: Flux function of an $m = 2$ island plotted as a function of the helical angle ξ and the distance from the rational surface. The island width, X- and O-points are indicated.

3.1 Magnetic reconnection and island topology

The formation of a magnetic island with mode number (m, n) is caused by a helical current perturbation with the same helicity. When an island forms, the geometry of nested flux surfaces breaks down and, due to magnetic reconnection, the typical island structure forms. This is accompanied by the formation of X- and O-points, as illustrated in figure 3.1. The magnetic island has a helical structure, which is centred at the resonant surface r_{res} and closes into itself after n poloidal and m toroidal turns. To describe the island geometry it is useful to introduce a helical coordinate ξ, which follows the helical mode structure and is defined as

$$\xi = \theta - q(r_{\text{res}})\phi, \tag{3.5}$$

with θ and ϕ the poloidal and toroidal angle, respectively and $q(r_{\text{res}}) = m/n$. This coordinate is perpendicular to the equilibrium field line, which connects the island O-points. Together with the radial component r and the poloidal angle θ a new coordinate system is thus provided (r, θ, ξ), which is suitable to describe the magnetic island topology.

Resistive MHD instabilities in general are associated with changes in the plasma topology. In a region where opposing magnetic fields meet ($B^* < 0$ and $B^* > 0$), the intrinsic energy of the system can be reduced due to reconnection of field lines. Along $B^* = 0$ a chain of magnetic islands forms. This is accompanied by the formation of topologically separated regions, where the plasma streams into, at the X-points. This is schematically illustrated in figure 3.2. In the confined plasma region of a tokamak (inside the separatrix) no location of opposing magnetic fields exists. Nevertheless, reconnection takes place at the resonant surfaces, due to the fact that the superposition of the toroidal and the poloidal magnetic

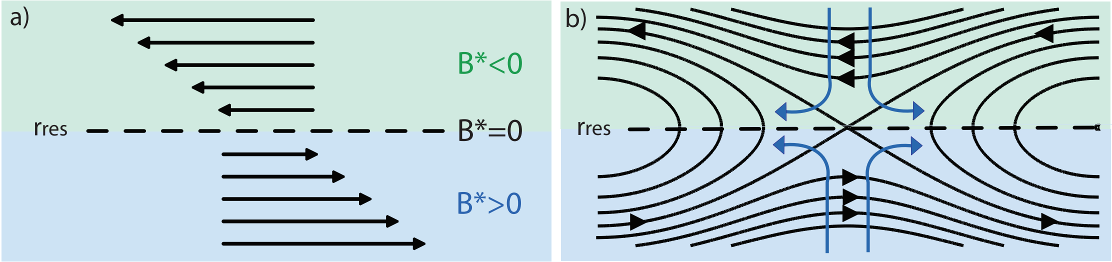

Figure 3.2: Schematic illustration of magnetic reconnection in the region of opposite magnetic fields

field leads to a shearing of the total magnetic field, which generates a similar situation [32]. A quantity to describe this shearing is q, defined in equation (1.9), which describes the flux surface averaged pitch of the field lines. In the following a monotonically increasing q profile is assumed. As stated before, following a helical field line at a resonant surface, this field line closes onto itself after m toroidal and n poloidal turns at the same (initial) poloidal angle (starting point). This is illustrated for the $q = 2$ surface in figure 3.3 (a) by the blue line. After two poloidal turns a field line closer to the core at a lower q, ends at a larger poloidal angle (green line). In contrast the field line further outside, at a higher q, has a smaller pitch and, thus, ends at a smaller poloidal angle (red line) compared to the starting point. This consideration shows that in a helical coordinate system centred on a rational surface a poloidal component of the magnetic field B^* exists, which changes sign at the resonant surface due to the different field line pitch (figure 3.3 (b)). This enables reconnection at the resonant surfaces. This helical field B^*, according to the above considerations, is mainly in the poloidal direction and can be approximated by $B^* \approx B_{\mathrm{pol}}(r) - B_{\mathrm{pol}}(r_{\mathrm{res}})(r/r_{\mathrm{res}})$ [32]. In the following, the changes in the topology of the magnetic flux due to reconnection are calculated. In this calculation all equilibrium fields are denoted with 0. The perturbed parameters are indicated with 1.

The topological changes of the magnetic flux in the presence of a magnetic island can be calculated by superimposing the equilibrium flux Ψ_0 and the perturbed flux Ψ_1 in the vicinity of the resonant surface. In the following all fluxes Ψ are normalised to R and, hence, are fluxes per unit length. The perturbed flux can be defined as follows:

$$\Psi_1 = \hat{\Psi}_1 \cos(m\xi) \tag{3.6}$$

Assuming $\hat{\Psi}_1$ to be constant over the island region, which is the so called 'constant Ψ approximation' [33] and valid to some extent for islands with $m > 1$, the total helical magnetic flux can be defined as the sum of the equilibrium and the perturbed flux [32, 34]

$$\Psi^* = \Psi_0(r_{\mathrm{res}}) + \Psi_1. \tag{3.7}$$

In the shifted helical coordinate system the equilibrium helical field B^* is set to 0 at the resonant surface, which implies that $\partial\Psi_0/\partial r$ is zero at the resonant surface. Therefore, the equilibrium flux Ψ_0 can be approximated by a parabola [32]. This results in the following

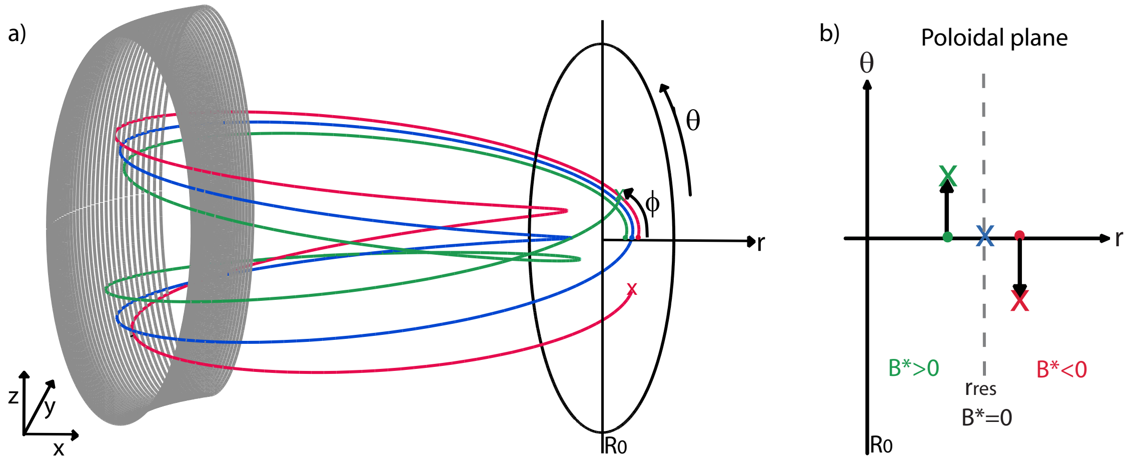

Figure 3.3: Schematic illustration of the conditions in a tokamak, which make magnetic reconnection possible. (a) Three radially distributed field lines at different q-surfaces, which end after one toroidal turn at different poloidal angles. (b) Poincare plot of one poloidal plane in (θ, r) for the three field lines.

expression for the helical flux:

$$\Psi^* = \Psi_0(r_{\mathrm{res}}) + \frac{1}{2}\Psi_0''(r - r_{\mathrm{res}})^2 + \hat{\Psi}_1 \cos(m\xi) \tag{3.8}$$

The equation for the new flux surfaces can be derived by reforming equation (3.8)

$$x = \sqrt{\frac{2}{\Psi_0''}(\Psi^* - \Psi_0(r_{\mathrm{res}}) - \hat{\Psi}_1 \cos(m\xi))}, \tag{3.9}$$

with $x = r - r_{\mathrm{res}}$. This expression is similar to the expressions derived in [35] and [36]. The flux surfaces in the vicinity of the resonant surface for an $m = 2$ island are illustrated in figure 3.1, where the island structure, including the X- and O-points and the island separatrix, are visible. The flux is most strongly perturbed close to the location of the island. For positive shear ($dq/d\Psi = q' > 0$) the minimum in the perturbed flux Ψ^* is found at the O-point ($\xi = \pi/2$), where the perturbed current flows opposite to the equilibrium current and the island has its full width W. In the X-points the flux perturbation is maximal ($\xi = 0$). The island width can be determined by calculating the island separatrix at the X- and O-points where (ξ, x) are (0,0) and $(\pi/2, W)$, respectively. Identifying both expressions delivers an equation for W [32, 34]

$$W = 4\sqrt{\frac{\Psi_1}{\Psi_0''}}. \tag{3.10}$$

Using the relation $\Psi_1 = -B_1(r_{\mathrm{res}})r_{\mathrm{res}}/m$ and the approximation $\Psi_0'' \approx -B_{0,\mathrm{pol}}q'/q$ [34] the island width can be calculated using parameters which can be gained from the experiment (compare also [35] and [36])

$$W = 4\sqrt{\frac{B_1(r_{\mathrm{res}})r_{\mathrm{res}}q}{mB_{0,\mathrm{pol}}q'}}. \tag{3.11}$$

3.2 Island evolution equation

In cylindrical geometry the tearing mode equation for the linear growth of an island can be derived. Using the large aspect ratio approximation ($\epsilon = a/R << 1$, with a the minor and R the major plasma radius) the perturbed magnetic field can be written as $\vec{B}_1 = \vec{\nabla}\Psi \times \vec{e}_\phi$, with $\vec{e}_\phi$ being the unit vector in toroidal direction. It is additionally assumed that the helical direction is almost toroidally, hence $\vec{e}_\xi \approx \vec{e}_\phi$. In the ideal region plasma inertia can be neglected, which results in $\vec{\nabla}p = \vec{j} \times \vec{B}$ according to equation (3.3). Using the identity that the curl of a gradient is zero ($\nabla \times \vec{j} \times \vec{B}$=0), expressing $\vec{B}$ in terms of Ψ and linearising the toroidal component of the resulting equation yields: [37, 3]

$$\frac{\partial}{r\partial r}\left(r\frac{\partial \Psi_1}{\partial r}\right) - \frac{m^2}{r^2}\Psi_1 + \frac{\mu_0 j'_{0,\phi}}{B_{0,\mathrm{pol}}(1-q(r)n/m)}\Psi_1 = 0, \tag{3.12}$$

with $j_{0,\phi}$ the equilibrium current in toroidal direction. This tearing mode equation describes the perturbation of the plasma equilibrium due to a perturbed flux at $r = r_{\mathrm{res}}$ in the linear regime. This is valid if the island is small compared to the linear layer width δ_{layer} ($W << \delta_{\mathrm{layer}}$), defined as the region in which non-ideal effects are negligible. The island is driven by the gradient of the perturbed equilibrium current. The perturbed equilibrium flux Ψ_1 in the linear regime can be determined by integrating equation (3.12) for ($r_{\mathrm{core}} \rightarrow r_{\mathrm{res}} - \varepsilon$) and ($r_{\mathrm{wall}} \rightarrow r_{\mathrm{res}} + \varepsilon$), using appropriate boundary conditions for the plasma core and the wall. Equation (3.12) has a singularity at $q_{\mathrm{res}} = m/n$, since the resistivity is neglected in this case. Nevertheless continuous solutions can be found, and the step in $d\Psi_1/dr$ at r_{res} corresponds to a current flowing at the resonant surface, which corresponds to the definition of Δ'_0 [38, 36, 35, 32]

$$\Delta'_0 = \lim_{\varepsilon\rightarrow 0}\left[\frac{1}{\Psi_1}\frac{d\Psi_1}{dr}\right]_{r_{\mathrm{res}}-\varepsilon}^{r_{\mathrm{res}}+\varepsilon}. \tag{3.13}$$

Using this equation the current flowing at the resonant surface for a **infinitesimal small island**, which grows **linearly** can be determined. The parameter Δ'_0 is the so called 'Delta prime' and is a property of the plasma equilibrium. It is a measure for the total perturbed parallel current inside the island. The Δ'_0 can be seen as the free energy which is available for supporting magnetic reconnection and generating a magnetic island [39]. If Δ'_0>0 then the growth of a tearing mode is supported by the plasma equilibrium.

The evolution equation for the island width, in terms of the poloidal flux Ψ, for a **large island**, which grows **non-linearly**, can be calculated on the basis of the expressions derived in section 3.1 and Ohm's law (equation 3.4) which takes into account the resistivity η in the vicinity of an island in a layer with width W. Based on this, an expression for the perturbed flux, in the non-linear regime can be found [35, 36, 32]

$$\frac{\partial \Psi_1}{\partial t} = E_\xi + \nabla_\xi \varphi = \eta j_\xi - (\vec{v} \times \vec{B})_\xi + \nabla_\xi \varphi, \tag{3.14}$$

in terms of E_ξ the inductive electric field and φ the electrostatic potential with ∇_ξ the derivation in helical direction. Assuming that the dominant contribution is due to currents flowing along the field lines, $(\vec{v} \times \vec{B})$ can be neglected. Additionally, the dependence on φ can be eliminated by averaging over the flux surfaces, denoted with $\langle\rangle$

$$\langle X \rangle = \frac{\int\int XJd\theta d\phi}{\int\int Jd\theta d\phi}, \tag{3.15}$$

with J the Jacobian of the system and X an example variable. This yields

$$\frac{\partial \Psi_1}{\partial t} = \langle E_\xi \rangle = \langle \eta j_\xi \rangle. \tag{3.16}$$

According to Ampère's law (equation (3.1)) the helical current j_ξ can be determined from the jump of the tangential component of the perturbed helical field B^* across the island, assuming a small island, and the current to be localised inside this small layer [32]

$$\begin{aligned} j_\xi &= \frac{1}{\mu_0 W}(B^*(r_{\text{res}}^-) - B^*(r_{\text{res}}^+)) \qquad (3.17) \\ &= \frac{1}{\mu_0 W}(\Psi_1'(r_{\text{res}}^+) - \Psi_1'(r_{\text{res}}^-)) = \frac{\Psi_1(r_{\text{res}})}{\mu_0 W}\Delta'(W). \qquad (3.18) \end{aligned}$$

As in the linear case, the parameter $\Delta'\Psi_1$ defines the jump in $d\Psi_1/dr$ across the island with $r_{\text{res}}^- = r_{\text{res}} - W/2$ and $r_{\text{res}}^+ = r_{\text{res}} + W/2$, matching the solution for Ψ_1 for $r < r_{\text{res}}^-$ and $r > r_{\text{res}}^+$ at the island separatrix, which can be calculated assuming an ideal plasma [38, 36, 35, 32]. This leads to the expression for Δ' in the non-linear regime

$$\Delta' = \left[\frac{1}{\Psi_1}\frac{d\Psi_1}{dr}\right]_{r_{\text{res}}^-}^{r_{\text{res}}^+}. \tag{3.19}$$

Together with equation (3.16) this leads to the equation for the perturbed flux [32]

$$\frac{\partial \Psi_1}{\partial t} = \frac{\eta}{\mu_0}\frac{\Psi_1(r_{\text{res}})}{W}\Delta'(W) \tag{3.20}$$

This matching condition can also be expressed as an integral over the island region [35, 36]

$$\Delta'\hat{\Psi}_1 = 2\mu_0 R \int_{r_{\text{res}}^-}^{r_{\text{res}}^+} dx \oint \langle j_\xi \rangle d\xi = 2\mu_0 R \int_{-\infty}^{\infty} dx \oint j_{||}\langle \cos(m\xi)\rangle d\xi. \tag{3.21}$$

The parameter x is again defined as $r - r_{\text{res}}$. Here is important to note, that only the helical component of the current, which is the $\cos(m\xi)$ component of the current parallel to the field lines $j_{||}$, contributes to the tearing mode evolution.

3.2.1 Rutherford equation

Rutherford introduced a simple model to calculate the island evolution, where the inductive contribution to $j_{||}$ is assumed to be the dominant one [38], as already assumed in the previous section. The corresponding electric field and current are generated by the time dependent growth of the island and are proportional to $d\Psi_1/dt$, according to equation (3.16) [35]. The classical Rutherford equation for the tearing mode evolution in terms of the island width W is obtained, substituting the relation for W and Ψ according to equation (3.10), in equation (3.20) [38]

$$a_1 \tau_{\mathrm{res}} \frac{dW}{dt} = r_{\mathrm{res}}^2 \Delta'. \tag{3.22}$$

The current diffusion time or resistive time-scale τ_{res} is defined as $\mu_0 r_{\mathrm{res}}^2/\eta$. The parameter $a_1 \approx 0.82$ results from the integration and is connected to the island geometry. According to equation (3.22), for positive Δ' a tearing mode is destabilised and is growing. Negative Δ' implies that the plasma is stable against tearing modes, hence, no free energy is available to support magnetic reconnection. For small islands Δ' is assumed to not depend on the island width as assumed in equation (3.13). Bigger islands with width W influence the toroidal current distribution and change Δ' itself, such that Δ' decreases with increasing island width. This leads to an island growth until it reaches the saturated island width $W = W_{\mathrm{sat}}$. This effect is included in the following approximation for Δ' [32, 40]

$$\Delta' = \Delta_0' \left(1 - \frac{W}{W_{\mathrm{sat}}}\right), \tag{3.23}$$

and describes the evolution of a classical tearing mode.

3.2.2 Modified Rutherford equation

In general not only the inductive contribution influence the island evolution. All currents which exist in the island region and contain a helical component in the $\cos(m\xi)$ direction contribute to the parallel current $j_{||}$ and alter the island evolution equation (equation (3.21)). In a tokamak the flux surface averaged perturbed parallel current $\langle j_{||}\rangle$ consists of an inductive part $(\eta E_{||})$, a neoclassical contribution (j_{neo}) and can also contain diverse internally or externally driven contributions (j_{div}) [36]

$$\langle j_{||}\rangle = \frac{1}{\eta}\langle E_{||}\rangle + \langle j_{\mathrm{neo}}\rangle + \langle j_{\mathrm{div}}\rangle. \tag{3.24}$$

These currents stabilise the mode when they are directed parallel to the perturbed current, and destabilise the mode when they are directed in opposite direction. In the following some of those currents are presented.

One important contribution to the evolution of magnetic islands is the perturbation of the bootstrap current. This current is a neoclassical effect, already indicated in equation (3.24). This contribution drives the neoclassical tearing modes (NTMs) [41, 42]. Another helical current perturbation, important for this work, is the current induced by external magnetic perturbation coils which also can alter the island evolution. This contribution is discussed in detail in section 3.4. Another contribution, also discussed in the following, is induced by the resistive wall, described in section 3.6.2. Both these contributions enter in j_{div} in equation (3.24). A variety of further contributions exist, which are not discussed here.

Perturbed bootstrap current

In a tokamak the toroidal magnetic field decreases with $1/R$. A particle following a field line encounters regions of higher magnetic field. In these regions the velocity component perpendicular to the field lines $v_\perp$ is increased and, in order to conserve magnetic moment, the parallel velocity $v_{||}$ of the particle is decreased. Particles with a sufficiently high velocity parallel to the field line, still follow the field lines and circulate around the torus. These are called passing particles. All other particles with a smaller initial parallel velocity, return at a certain position ($v_{||} = 0$) and are trapped at the outboard side (low field side) in the so-called magnetic mirrors for $v_{||} \leq \epsilon^{1/2} v_\perp$ [3]. The superposition of several drifts (i.e the curvature and $\vec{\nabla} B$ drift) leads to trapped particle obits which, mapped to the poloidal plane, have a banana shape (banana orbits). The bootstrap current hence is a non-inductive current, which arises from collisions of trapped particles, that are confined on banana orbits, with passing particles. It is proportional to a linear combination of the radial gradient of temperature and density, which can be simplified as a dependence on the pressure gradient, and the fraction of trapped particles ($\epsilon^{1/2}$). In the limit of a small inverse aspect ratio (ϵ=r_{res}/R) this current can be written as [35, 43]

$$j_{\mathrm{bs}} \approx -\frac{\epsilon^{1/2}}{B_{\mathrm{pol}}} \frac{dp}{dr}. \tag{3.25}$$

A more accurate expression was introduced in [44], where the actual dependences on the gradients of the ion and electron temperature and the electron density are considered separately:

$$\delta j_{\mathrm{bs,Sauter}} = R B_{\mathrm{tor}} p_{\mathrm{e}} \frac{\left[(-0.5)\frac{p}{p_{\mathrm{e}}}\frac{\partial \ln p}{\partial \psi} + 0.2 \frac{\partial \ln T_{\mathrm{e}}}{\partial \psi} + (-0.25)\frac{\partial \ln T_{\mathrm{i}}}{\partial \psi}\right]}{\sqrt{\langle B^2 \rangle}}. \tag{3.26}$$

When a sufficiently large island forms, the heat flux across the island is enhanced due to an effective short-circuit of the field lines indicated in figure 3.1. Particles and heat cross the island by rapidly flowing along the field lines. Since the pressure can be seen as a flux surface quantity, the pressure profile will flatten inside the island and the pressure gradient is removed. According to equations (3.25) and (3.26) this leads to a loss of bootstrap current inside the island. This ‘helical hole’ in the bootstrap current in the vicinity of the island exhibits the required $\cos(m\xi)$ component to contribute to the perturbed parallel current $j_{||}$ and influences the island width evolution. Taking the inductive and neoclassical contributions ($j_{\mathrm{neo}} \hat{=} j_{\mathrm{bs}}$) into account and substituting this expression for $j_{||}$ in equation (3.21) and using the expression for the island width (equation (3.10)) gives the modified Rutherford equation [35, 43, 45, 46, 35, 41, 42]:

$$a_1 \tau_{\mathrm{res}} \frac{dW}{dt} = r_{\mathrm{res}}^2 \Delta'(W) + r_{\mathrm{res}}^2 \Delta_{\mathrm{bs}} \tag{3.27}$$

$$\Delta_{\mathrm{bs}} = a_2 \epsilon^{1/2} \frac{L_q}{L_{\mathrm{p}}} \frac{\beta_{\mathrm{pol}}}{W} \tag{3.28}$$

The plasma β in this formula is the β_{pol} defined as $(2\mu_0\langle p\rangle/B_{\mathrm{pol}}^2)$ with p the total pressure and $\langle B_{\mathrm{pol}}\rangle$ the flux- surface averaged poloidal magnetic field strength at the resonant surface. The magnetic shear length is defined as $L_q = q/q'$, while the gradient length of the pressure is $L_{\mathrm{p}} = -p/p'$, due to the negative pressure gradient. In normal operation this leads to $L_q/L_{\mathrm{p}} > 0$. So the loss of bootstrap current contributes to the drive of NTMs, whereas for NTMs the effect of the equilibrium current (Δ') is normally assumed to be stabilising. The parameter a_2 is a left over from the spatial integral in equation (3.21) and of the order of unity.

Small island effects

According to equation (3.27) all islands whose resonant surface is present in the plasma would be unstable and grow. Since this is not observed in experiment, additional effects, which are mainly important at small island size, must play a role. These effects lead to a threshold for the island growth (NTM threshold).

The first important effect is a transport effect due to radial diffusion [45]. For large islands the flattening of the temperature T for example can be described by the following equation

$$\chi_{||}\nabla_{||}^2 T + \chi_{\perp}\nabla_{\perp}^2 T = 0, \tag{3.29}$$

with $\chi_{||}$ and $\chi_{\perp}$ being the parallel and perpendicular heat conductivities. For these islands the ratio of $\chi_{||}/\chi_{\perp}$ can be seen as infinite and T is a flux surface function. This is not true for small islands. Approximating $\nabla_{||}$ with $\sim W$ and $\nabla_{\perp}$ with$\sim 1/W$ yields a dependence of $\chi_{||}/\chi_{\perp}$ on W^4. Hence, for islands smaller than a critical island width W_χ the ratio of $\chi_{||}/\chi_{\perp}$ is finite. This means that the parallel transport does not dominate over the perpendicular one and both are of the same order of magnitude. This leads to an incomplete temperature (pressure) flattening inside the island and reduces the drive due to the loss of bootstrap current.

The second small island effect is a finite orbit width effect [46, 47, 48]. In general, a small island is rotating with respect to the surrounding plasma, due to torques acting on the island. These torques are caused by currents in the vicinity of the island, which have a component proportional to $\sin(m\xi)$, compared to currents contributing to the island growth depending on $\cos(m\xi)$. The resulting differential rotation is connected with an electrostatic potential in order to satisfy the ideal MHD condition $E_{||} = 0$. This leads to an $\vec{E} \times \vec{B}$ flow along the magnetic surface. This flow is faster around the island's O-points, which leads to an acceleration of the plasma around the island from the X-point to the O-point. According to equation (3.3), this plasma flow is balanced by a current perpendicular to the magnetic surface, the polarisation current. The polarisation current is mainly carried by the ions due to a smaller cyclotron frequency. Since the plasma is incompressible ($\vec{\nabla} \cdot \vec{j} = 0$) this perpendicular polarisation current gives rise to a current streaming parallel to the magnetic surface, which varies with $\cos(m\xi)$ and thus, alters the modified Rutherford equation (3.21). This effect is proportional to $1/W^3$ (compare equation (3.33)) and, hence, is mainly important for small islands. The polarisation current effect depends strongly on collisionality [46, 49] and is enhanced for high ion collision frequencies with respect to the mode rotation $\nu_{\mathrm{ii}}/\omega > 1$. In this work the following expression for the ion-ion collision time τ_{ii} is used [5]

$$\tau_{\mathrm{ii}} = 1/\nu_{\mathrm{ii}} = \frac{12\pi^{3/2}}{\sqrt{2}} \frac{m_{\mathrm{i}}^{1/2} T_i^{3/2} \epsilon_0^2}{n_{\mathrm{i}}(eZ)^4) \ln \Lambda}, \tag{3.30}$$

with $\ln \Lambda$ the Coulomb logarithm. Depending on the island rotation frequency ω this contribution can be stabilising or destabilising. In most of the cases it is assumed to be stabilising, in order to explain the stability of small islands refereed to above which leads to a threshold in the island growth. Including both of these small island effects in the island evolution equation leads to a final expression for the modified Rutherford equation [35]:

$$a_1 \tau_{\mathrm{res}} \frac{dW}{dt} = r_{\mathrm{res}}^2 \Delta'(W) + r_{\mathrm{res}}^2 \Delta_{\mathrm{bs}} + r_{\mathrm{res}}^2 \Delta_{\mathrm{pol}} \tag{3.31}$$

$$\Delta_{\mathrm{bs}} = a_2 \epsilon^2 \frac{L_q}{L_{\mathrm{p}}} \frac{\beta_{\mathrm{pol}}}{W} \left[\frac{W^2}{W^2 + W_\chi^2} \right] \tag{3.32}$$

$$\Delta_{\mathrm{pol}} = -a_3 g(\epsilon, \nu_{\mathrm{ii}}) \left(\rho_{\theta \mathrm{i}} \frac{L_q}{L_{\mathrm{p}}} \right)^2 \frac{1}{W^3} \tag{3.33}$$

The parameter $\rho_{\theta\mathrm{i}} = \sqrt{2 m_{\mathrm{i}} k_{\mathrm{B}} T_{\mathrm{i}}}/e B_{\mathrm{pol}}$ is the ion poloidal gyro radius, with k_{B} the Boltzmann constant. The collisionality dependence of the ion polarisation current is included via the factor $g(\epsilon, \nu_{\mathrm{ii}})$ [50] which is $\epsilon^{3/2}$ for 'collisionless' plasmas ($\nu_{\mathrm{ii}}/\epsilon\Omega_{\mathrm{e}}^* << 1$) and equal to 1 in the 'collisional' case. The frequency Ω_{e}^* is the electron diamagnetic drift frequency defined later on in equation (3.54). The coefficient a_3 is again connected to the integral in equation (3.21) and is of the order of unity.[3]

Stability diagram

In figure 3.4 the dependence of the island growth rate dW/dt on the island width W, according to equation (3.31), is illustrated for three different β_{pol} values assuming a stabilising contribution of Δ'.

For high β_{pol}, shown in red, the evolution shows two zeros ($dW/dt = 0$). The first one is due to the small island effects, which lead to a threshold for the island onset. The growth rate is positive only if W exceeds a critical island width W_{crit}. Thus, a 'seed' perturbation is needed, which induces a seed island with $W_{\mathrm{seed}} \geq W_{\mathrm{crit}}$ to destabilise an NTM. As β_{pol} increases, $W_{\mathrm{crit}}(\beta_{\mathrm{pol}})$ decreases. Therefore, destabilising an NTM requires a smaller W_{seed} at higher β_{pol}. If W exceeds W_{crit} the island will grow until it reaches the saturated island width W_{sat}, which corresponds to the second zero of dW/dt. Also W_{sat} increases with increasing β_{pol}. However, W_{sat} can increase such that any further rise in β_{pol}, e.g. due to an increase of heating power, leads to island growth. This flattens the pressure over a larger region and results in a confinement degradation, thus cancels the initial increase in β_{pol}. It is therefore not possible to increase β_{pol} further, which can be seen as a 'soft β-limit' [46]. For very large

---

[3] More recent results have shown that the polarisation current is likely smaller than expected from equation (3.33), see references [51, 52, 48]

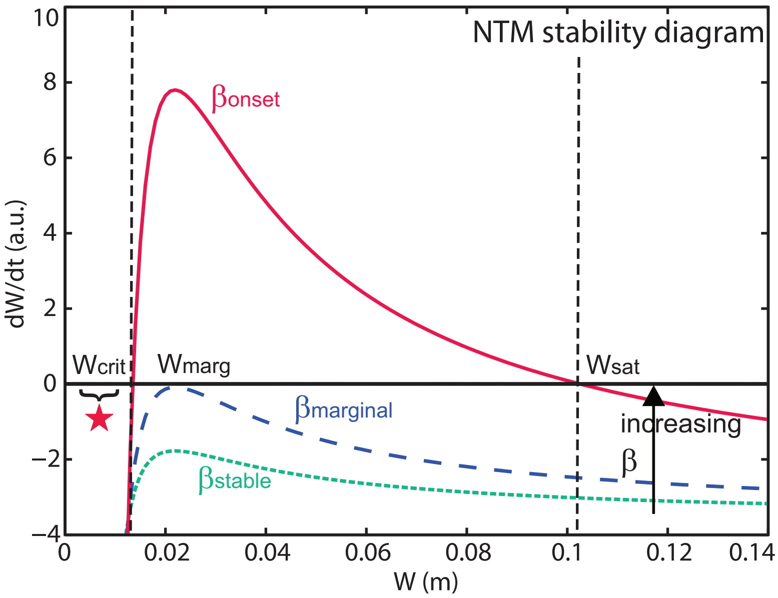

Figure 3.4: Island growth rate (including the Δ' , the bootstrap current and the ion polarisation current term) according to equation (3.31), versus the island width for three different β_{pol}.

islands the whole process can also terminate in a disruption ('hard β limit').

The island can be stabilised by decreasing β_{pol}, e.g. ramping down the heating power, towards the marginal point (β_{marg}). Once β_{marg} is reached (blue curve in figure 3.4), the island decays rapidly independently of β_{pol}.

For $\beta_{\mathrm{pol}} < \beta_{\mathrm{marg}}$, shown in green, no W exists for which dW/dt is positive and the plasma is stable against NTMs.

To conclude, the NTM growth requires a β_{pol} larger than β_{marg} and a 'seed' island with a width W_{seed} that exceeds $W_{\mathrm{crit}}(\beta_{\mathrm{pol}})$. These are the reasons why NTMs mainly appear in plasmas with high pressure.

3.3 Trigger mechanisms

According to equation (3.31), the plasma is linearly stable against NTMs if no seed perturbation is present which leads to a seed island with $W_{\mathrm{seed}} > W_{\mathrm{crit}}(\beta_{\mathrm{pol}})$ Only the appearance of a seed perturbation leads to a nonlinearly unstable situation and the onset of an NTM. Typically, the trigger mechanisms of the most common m/n=3/2 and 2/1 NTMs are MHD instabilities with different mode numbers. These instabilities, or their harmonics, couple toroidally to the resonant surface and induce a seed perturbation at this location. For example, the $m \mp 1$ component of (the second harmonic of) a 1/1 instability at the $q = 1$ surface, can induce a seed perturbation at the q=2/1 or q=3/2 surface. This can lead to the onset of a 2/1 or 3/2 NTM, respectively [43]. Flat rotation profiles between the triggering and the island surface support the triggering process due to the absence of shielding effects, which are more pronounced for a high shear in rotation and in the magnetic field. At ASDEX Upgrade the typical trigger mechanisms are sawtooth crashes, fishbones and edge localised modes (ELMs) [53]. NTMs, which appear without any visible trigger, start as classical tearing mode but later on evolve into an NTM driven additionally by the loss of bootstrap current. In principle, externally applied magnetic perturbations can also lead to the seeding of an NTMs, see next section 3.4. The three triggering processes mentioned above are illustrated in figure 3.5. Here the typical time traces, which are used to identify the corresponding trigger mechanism at the NTM onset are illustrated for (a) a sawtooth crash, (b) a fishbone and (c) an ELM. The onset of each NTM is clearly visible in the increase of the amplitude of a pick-up coil signal (dB/dt) (second row from top) and in the according spectrograms (bottom row). All NTMs are accompanied by a loss in the normalised plasma $\beta_{\mathrm{N}} = \beta_{\mathrm{tor}}/(I_{\mathrm{p}}(\mathrm{MA})/(a(\mathrm{m})B_{\mathrm{tor}}(\mathrm{T})))$, shown in the topmost row. The toroidal β_{tor} is defined like β_{pol} but using the toroidal magnetic field. In figure 3.5 (a) the onset of a 3/2 and a 2/1 NTM is shown, both of which are triggered by a sawtooth crash. A sawtooth is a (resistive) 1/1 MHD instability in the plasma core and characterised by a collapse of the central pressure and temperature. Figure 3.5 (b) shows a 3/2 NTM triggered by a fishbone crash. The fishbone instability, driven by a fast ion population which then gets lost during the crash, is identified with the typical 'fishbone' pattern in the Soft X-Ray signal and the characteristic down shifting frequency evolution visible in the spectrogram. Figure 3.5 (c) illustrates the triggering by an ELM, which is characterised by a collapse of the density and temperature pedestal and the corresponding flushing out of particles and heat into the scrape-off layer, which is then detected by divertor shunt currents (ELM monitor).

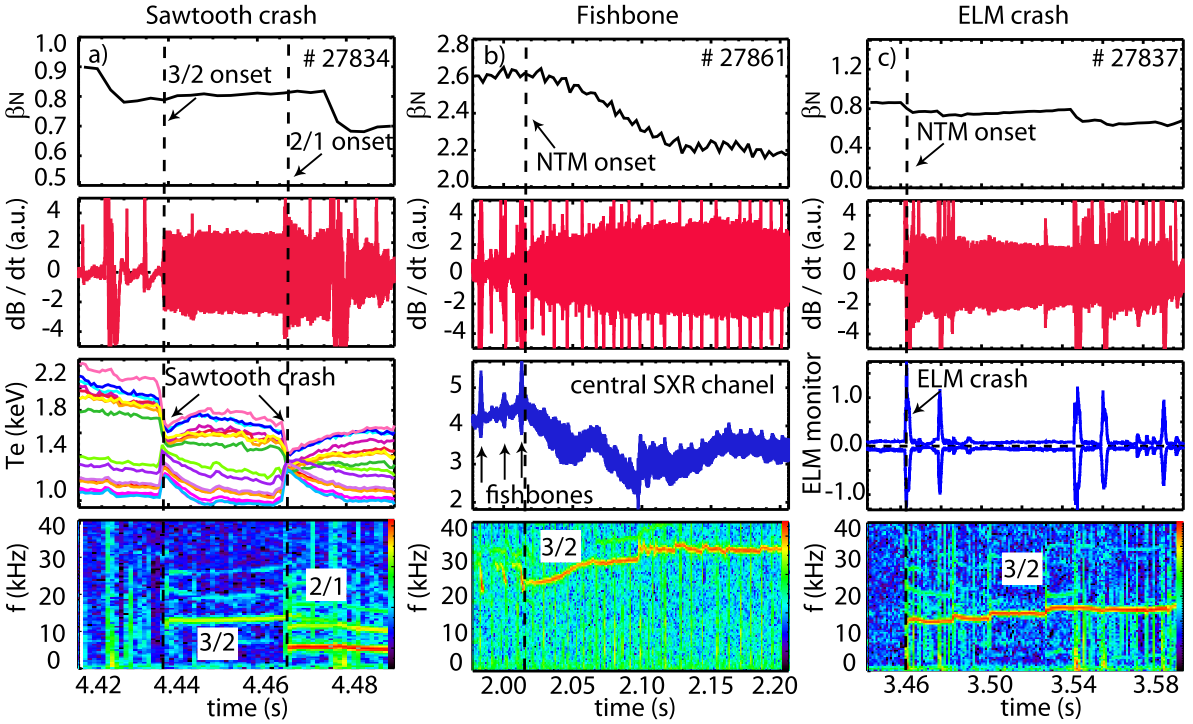

Figure 3.5: (3,2) Neoclassical tearing modes at ASDEX Upgrade triggered by (a) a sawtooth crash (b) a fishbone and (c) an ELM with corresponding typical time traces to illustrate the onset evaluation and the trigger correlation

3.4 External perturbation fields

In addition to perturbations inside the plasma, NTMs can also be influenced by externally applied magnetic perturbations (MPs). These perturbation fields are, for example, generated by currents flowing in external coils. At ASDEX Upgrade these perturbation coils are called B-coils (section 2.1) and are installed inside the vessel. The B-coils can be used in 'resonant' and 'non-resonant' configurations, adjusted by the phasing of the upper and lower coil row. Both configurations contain resonant and non-resonant magnetic field components, which act differently on the plasma and mode stability.

The resonant components of the MP field can penetrate into the plasma and provoke magnetic reconnection at a resonant surface which is accompanied by the generation of a small magnetic island at this surface. This small island can act as seed island for a neoclassical tearing mode. Static resonant magnetic perturbations can, therefore, produce a locked mode which, in most cases, leads to a disruption. Pre-existing rotating modes can also interact with the resonant MP fields. They are slowed down and lock to the MP field. The non-resonant components of the error field do not influence MHD modes directly but instead induce a global torque, the neoclassical toroidal viscous torque, and thus also support the appearance of locked modes [54]. Both effects are present in every B-coil configuration. The difference is that in a 'non-resonant' configuration the resonant components are minimised while in a 'resonant' configuration they are maximised. This is illustrated in figure 3.6, where the perturbed magnetic fields (vacuum plots) of an $n = 2$ 'non-resonant' (a) and 'resonant' (b) configuration in a poloidal cross section are shown. These vacuum plots are the result of a superposition of the perturbation field, caused by the B-coils and calculated using the vacuum field approximation, and the equilibrium field. This superposition leads to the formation of vacuum islands at the various resonant surfaces. The size of these vacuum islands depends on the magnitude of the resonant components of the perturbed flux Ψ_{vac}, according to equation (3.10) [37]. Hence, the magnitude of a resonant MP field component can be parametrised via the size of the vacuum island

$$W_{\mathrm{vac}} = 4\left(\frac{R_0 q}{B_{\mathrm{tor}}}\right)^{\frac{1}{2}} \left|\frac{\Psi_{\mathrm{vac}}}{(q'/q) r_{\mathrm{res}}}\right|^{\frac{1}{2}} . \tag{3.34}$$

In both figures vacuum islands are visible, hence, resonant components are present, but the vacuum islands are considerably larger in the 'resonant' case (fig. 3.6 (b)), especially at the q=3/2 and 4/2 surface.

3.4.1 Resonant magnetic field components

The resonant component of the perturbation field exhibits a discontinuity in the perturbed helical poloidal flux at a resonant surface, which implies the existence of a helical current being present at this surface [37]. This approach is analogue to a more compact description based on the formation of an island at a resonant surface in the vacuum magnetic field (superposition of the equilibrium and the perturbation field) induced by the resonant component of the magnetic perturbation field. The plasma response to the formation of this

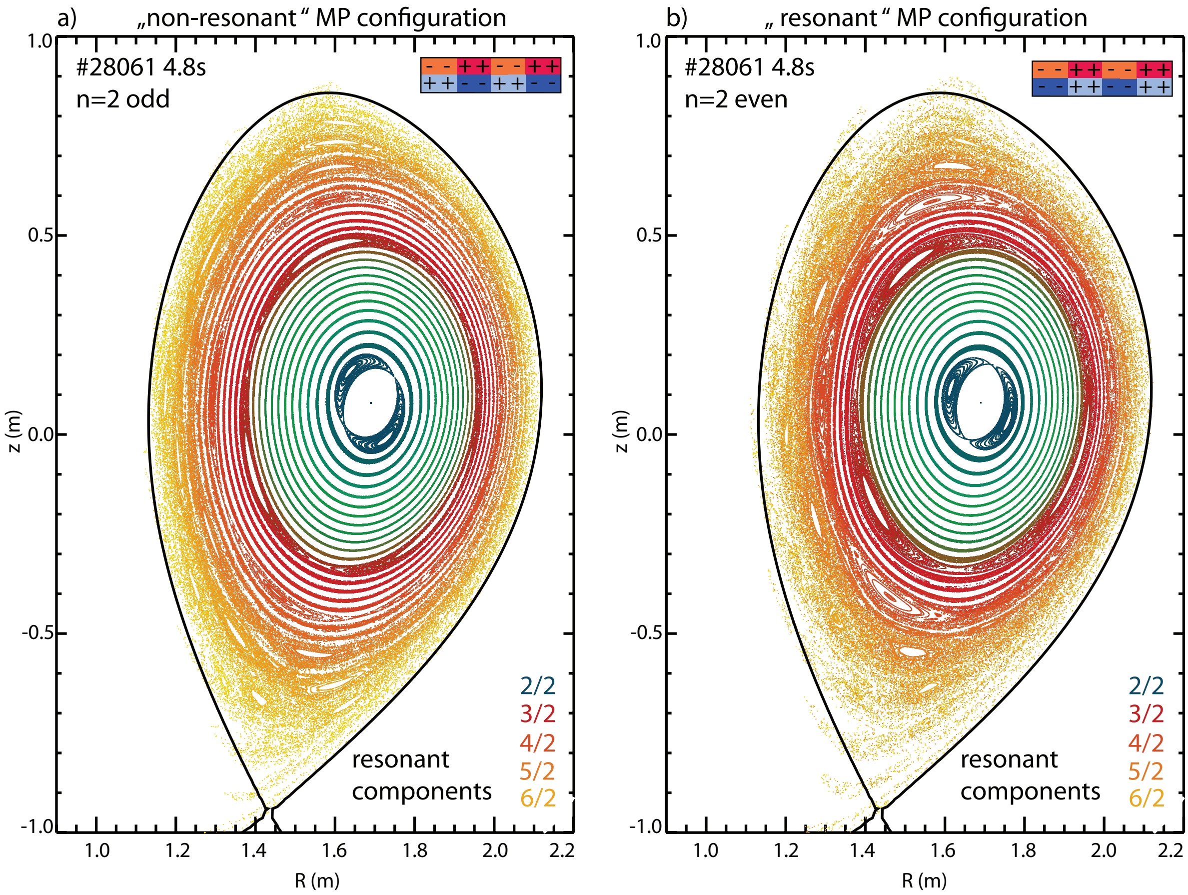

Figure 3.6: Vacuum plots resulting from the superposition of an equilibrium magnetic field, taken from #28061 at 4.8 s, with (a) a 'non-resonant' and (b) a 'resonant' $n = 2$ B-coil configuration.

vacuum island leads to the generation of a helical shielding current at this surface. The helical current generated at a resonant surface, according to both approaches, influences a magnetic island in two ways: it modifies the island width evolution due to an influence on the island stability, which can be described by the modified Rutherford equation. This interaction takes place for the component of the current that is in phase with the magnetic island ($\cos(\Delta\phi)$). Secondly the $\sin(\Delta\phi)$ component of the current causes a $(\vec{j} \times \vec{B})$ torque, which acts on the island in order to change the frequency of the mode to match the frequency of the perturbation field. The phase difference $\Delta\phi$ is defined as the difference of the toroidal location of the O-point of the magnetic island and the vacuum island [37].

Non-linear regime

In this work mainly the influence of static MPs on pre-existing large rotating islands is discussed. Large islands are not allowed to slip through the plasma; rather they rotate together with the plasma fluid. Their response to the MPs is non-linear. Therefore, the appropriate boundary conditions for the plasma flow ('non-slip theory') in the region of the island have to be used [37]. This provides the following equation for the contribution of the resonant MPs on the island stability in a cylindric geometry [37]

$$\Delta_{\mathrm{ext}} = \frac{2m}{r_{\mathrm{res}}} \left(\frac{W_{\mathrm{vac}}}{W} \right)^2 \cos(\Delta\phi), \tag{3.35}$$

and the extended modified Rutherford equation:

$$a_1 \tau_{\mathrm{res}} \frac{dW}{dt} \quad = \quad r_{\mathrm{res}}^2 \Delta'(W) + r_{\mathrm{res}}^2 \Delta_{\mathrm{bs}} + r_{\mathrm{res}}^2 \Delta_{\mathrm{pol}} + r_{\mathrm{res}}^2 \Delta_{\mathrm{ext}} \tag{3.36}$$

The toroidal perturbation caused by the externally applied magnetic fields is parametrised by the size of the vacuum island W_{vac}. The width W_{vac} can directly be calculated from the perturbed magnetic flux ψ_{vac} via equation (3.34) and can therefore be linked to the perturbed radial magnetic field at the resonant surface ($B_{\mathrm{r}} = -m\psi_{\mathrm{vac}})/r$). In addition to the influence on the island evolution, the resonant MPs exert a $(\vec{j} \times \vec{B})$ torque in the vicinity of the island, which tries to alter the mode frequency ω to match that of the MPs [37]. The toroidal component of this torque is

$$T_{\phi,\mathrm{jxB,non-linear}} = -4\pi^2 R_0 \frac{mn}{\mu_0} \ C^2 \ W_{\mathrm{vac}}^2 \ W^2 \ \sin(\Delta\phi). \tag{3.37}$$

The parameter C contains equilibrium quantities and is defined as:

$$C = \frac{r_{\mathrm{res}} B_{\mathrm{tor}} \left| q' \right|}{16 q^2 R_0}. \tag{3.38}$$

Equation (3.35) and (3.37) predict that the larger and the slower the island is, the stronger is the effect of the MPs on the island. Additionally, the influence on a rotating island in the non-linear phase is modulated. Assuming a large rotating island with initial size W_0 and initial frequency ω_0, figure 3.7 illustrates the modulation of dW/dt and $d\omega/dt$ according to the external field described by equations (3.35) and (3.37). It is visible in figure 3.7 that, due to the 'non-slip' condition for large islands, the mode frequency and width vary periodically and not in phase, which leads to the following situation: During the phases in which the mode is slowed down (figure 3.7 (b), red shadowed region), the island width is larger compared to W_0, whereas during the phases in which the mode is accelerated (figure 3.7 (b), orange shadowed region) the island is smaller compared to W_0. At the same time, in the phases where the mode is stabilised (figure 3.7 (a), green shadowed region), it is slower compared to the initial frequency ω_0. Therefore, the island stays longer in the region where it is stabilised. According to the applied theory, a rotating island experiences a net stabilising effect and is slowed down due to the MPs. Both effects are linked. Therefore, without the modulation of the island width no braking takes place and vice versa. As soon as the island locks ($\Delta\phi$=constant) this theory predicts a strong increase of the island width.

In order to calculate a time averaged $(\vec{j} \times \vec{B})$ torque, which is acting on the island in the non-linear regime, it can be assumed that the modulation of the island frequency is small. Hence, the island is rotating almost uniformly, which is valid in any case for substantially fast rotating islands. Additionally, it is assumed that the contribution of the perturbation field (equation (3.35)) is the dominant term in the modified Rutherford equation. In this

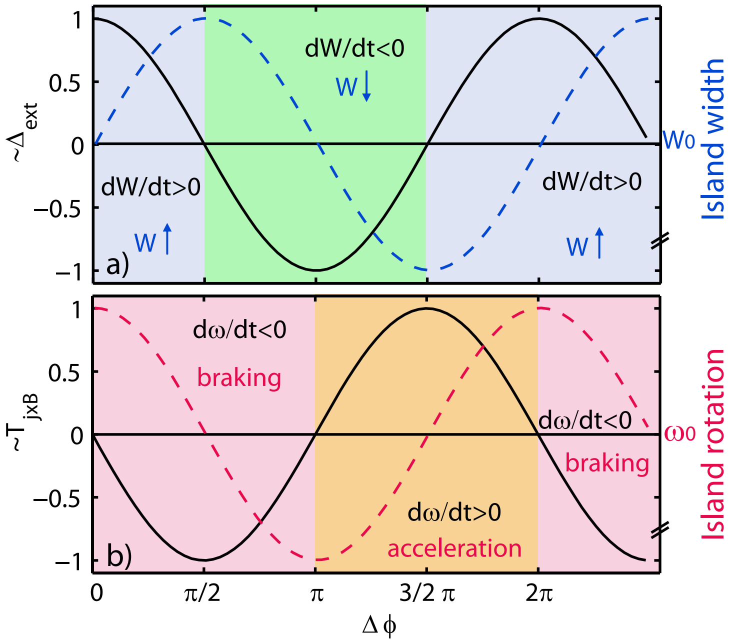

Figure 3.7: Modulation of the island width and phase evolution due to MPs as a function of the phase difference $\Delta\phi$ of the magnetic and the vacuum island. In (a) the evolution of the island width in terms of $dW/dt \sim \Delta_{\rm ext}$ is shown in black. The resulting island width W with respect to the initial island width W_0 is shown in blue (dashed line). In (b) the evolution of the island frequency in terms of $d\omega/dt \sim T_{j\times B}$ is shown in black. The resulting island frequency ω with respect to the initial island frequency ω_0 is shown in red (dashed line).

limit the modified Rutherford equation can be integrated analytically which yields for static perturbation fields [55]

$$W(t) \simeq \tilde{W}_0|\sin(\omega t)|^{1/3} \tag{3.39}$$

$$\tilde{W}_0 = 1.939\ m^{1/3}\left(\frac{W_{\rm vac}^2/r_{\rm res}^2}{\omega\tau_{\rm res}}\right)^{1/3} r_{\rm res}, \tag{3.40}$$

with ω the actual mode frequency (almost constant in time) and $\tilde{W}_0$ the maximal island width during one period (for $\Delta\phi = \pi/2$). The steady $(\vec{j}\times\vec{B})$ torque in toroidal direction is hence given by: [55]

$$\langle T_{\phi,{\rm jxB,non-linear}}\rangle = -4\pi^2 R_0\frac{mn}{\mu_0}\ 0.05356\ C^2\ W_{\rm vac}^2\ \tilde{W}_0^2(\omega) \tag{3.41}$$

Linear regime

This work is mainly focused on the interaction of externally applied MPs with pre-existing large rotating modes. Therefore the linear theory, valid for small islands e.g. in the case of mode penetration, is only briefly discussed for the particular case of static perturbation fields.

The linear theory applies for islands smaller than the linear layer width. These small islands are allowed to ‘slip’ through the plasma frame and do not necessarily rotate with the electron

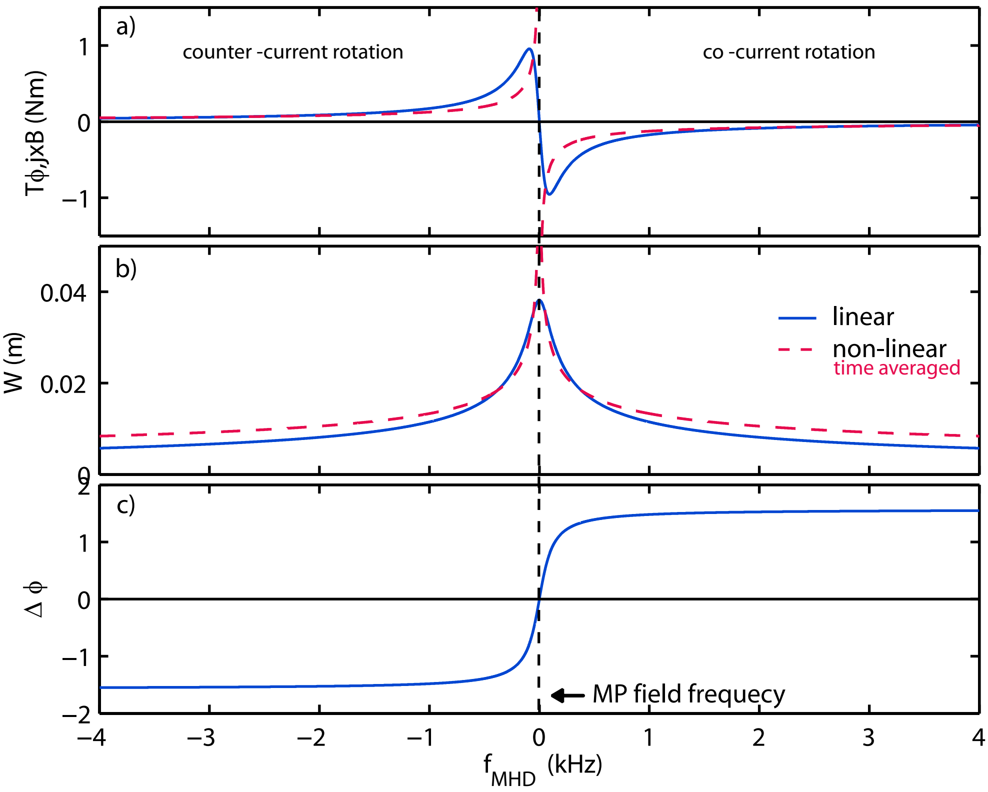

Figure 3.8: Example of (a) the $(\vec{j} \times \vec{B})$ torque, (b) the island width W and (c) the phase difference $\Delta\phi$ for the linear and non-linear theory at a $q = 2$ surface. The input parameters are listed in table 5.3.

fluid (see section 3.5). In the following the rotation of small modes in the unperturbed case (without B-coils) is defined as the unperturbed tearing frequency $\omega_{0,\mathrm{MHD}}$ [37]. Hence, static MPs induce a small island which is also not rotating but has a constant phase shift ($\Delta\phi$) with respect to the vacuum island due to the plasma flowing around it. This phase shift depends on $\omega_{0,\mathrm{MHD}}$ and due to the fact that it is constant the MPs exert a steady $(\vec{j} \times \vec{B})$ torque in the vicinity of the resonant surfaces.

In the following, the formulae for the visco-resistive limit are presented. This limit is valid for $\omega_{0,\mathrm{MHD}} << \tau_{\mathrm{V}}^{1/3}\tau_{\mathrm{H}}^{-2/3}\tau_{\mathrm{res}}^{2/3}$ with [37, 40]

$$\tau_V = \frac{r_{\mathrm{res}}^2}{D_\phi} \tag{3.42}$$

$$\tau_H = \frac{R_0\sqrt{\mu_0\rho(r_{\mathrm{res}})}}{B_{\mathrm{tor}} n(r_{\mathrm{res}}/L_q(r_{\mathrm{res}}))}, \tag{3.43}$$

where D is the momentum diffusion coefficient, ρ the ion mass density, τ_H the local hydromagnetic time-scale and τ_V the viscous diffusion time-scale at the corresponding resonant surface. In this limit the viscosity and the resistivity play the dominant role in the island region, while the inertia is neglected. When the island is smaller than the visco-resistive linear layer width ($W < \delta_{\mathrm{VR}} = (\tau_{\mathrm{H}}^{1/3}\tau_{\mathrm{res}}^{-1/6}\tau_{\mathrm{V}}^{-1/6}r_{\mathrm{res}})$) the steady torque $T_{\phi,\mathrm{jxB,linear}}$, the induced island width W and the phase shift $\Delta\phi$ are given by [37, 40]

$$\begin{aligned} T_{\phi,\mathrm{jxB,linear}} &= -4\pi^2 R_0 \frac{2m^2 n}{\mu_0 |\Delta_0' r_{\mathrm{res}}|} \frac{\omega_{0,\mathrm{MHD}}\ \tau_{\mathrm{rec}}}{1+(\omega_{0,\mathrm{MHD}}\ \tau_{\mathrm{rec}})^2}\ C^2\ W_{\mathrm{vac}}^2 && (3.44)\\ W^2 &= \frac{1}{\sqrt{1+(\omega_{0,\mathrm{MHD}}\ \tau_{\mathrm{rec}})^2}} \frac{2m}{|\Delta_0' r_{\mathrm{res}}|} W_{\mathrm{vac}}^2 && (3.45)\\ \Delta\phi &= \arctan(\omega_{0,\mathrm{MHD}}\ \tau_{\mathrm{rec}}), && (3.46) \end{aligned}$$

with Δ_0' the stability parameter in the linear regime, described by equation (3.13), and τ_{rec} the reconnection time-scale in the visco-resistive limit defined as

$$\tau_{\mathrm{rec}} = \frac{2.1036}{|\Delta_0' r_{\mathrm{res}}|} \frac{\tau_{\mathrm{H}}^{1/3} \tau_{\mathrm{res}}^{5/6}}{\tau_{\mathrm{V}}^{1/6}}. \tag{3.47}$$

In figure 3.8 the torque $T_{\phi,\mathrm{jxB}}$, the island evolution W and the phase shift $\Delta\phi$ at a q=2 surface according to an n=2, m=4 MP field in the linear case with respect to $f_{\mathrm{MHD}} = \omega_{0,\mathrm{MHD}}/(2\pi)$ are illustrated. The phase shift $\Delta\phi$ increases with increasing tearing frequency (for static MPs) which accordingly leads to a strong decrease in $T_{\phi,\mathrm{jxB}}$ and W. The time averaged non-linear torque and the non-linear island width evolution, according to equation (3.41) and (3.40), with respect to the NTM frequency ($\hat{=} f_{\mathrm{MHD}}$), are also shown. The linear and non-linear torque are of the same order of magnitude and show a similar behaviour. In both theories the island width and torque are largest if f_{MHD} is close to the MP field frequency ($f_{\mathrm{B-coils}}$) which is zero at AUG. When f_{MHD} differs from $f_{\mathrm{B-coils}}$ the torque acts in the direction to adapt f_{MHD} to $f_{\mathrm{B-coils}}$.

3.4.2 Non-resonant magnetic field components

The non-resonant components of the MPs only give rise to the neoclassical toroidal viscous torque (NTV) and do not influence the island stability directly. The NTV torque contributes to the plasma rotation damping generated by a non-ambipolar radial flow of trapped particles induced by the error field. The externally applied magnetic perturbations break the axisymmetry of the magnetic field, which leads to a distortion of the flux tubes [56]. However, the flux conservation leads to a modulation of the magnetic field; an increased magnetic field exists in regions with a decreased cross-section and vice versa. This modulation of the magnetic field in turn leads to a modulation of the ratio of parallel to perpendicular pressure. Due to collisions, the modulation of the flux tube and the pressure are not in phase and a radial drift of trapped particle arises. This leads to a radial current and hence, a ($\vec{j} \times \vec{B}$) torque caused by the non-resonant components of the error field arises. The NTV torque can be calculated in the relevant collisionality regime from the relation between the radial ion particle flux and the toroidal forces. In particular, the toroidal ($\vec{e}_\phi$ direction) viscous stress $\langle \vec{e}_\phi \nabla \cdot \overset{\leftrightarrow}{\pi}_i \rangle$ is important [57, 58], with $\overset{\leftrightarrow}{\pi}_i$ the viscosity tensor. This connection can be made by solving the flux surface averaged ion momentum equation in the toroidal direction: [58] [49]

$$\langle \vec{e}_\phi \frac{\partial}{\partial t} \rho \vec{v}_{\mathrm{i}} \rangle = -\langle \vec{e}_\phi \nabla \cdot \overset{\leftrightarrow}{\pi}_i \rangle + ..., \tag{3.48}$$

with ρ the ion mass density and $\vec{v}_\mathrm{i}$ the rotation velocity of the ion fluid, and the force-friction relation:

$$Ze\Gamma_i = \langle \vec{e}_\phi \nabla \cdot \overset{\leftrightarrow}{\pi}_i \rangle = -t_\mathrm{NTV} \tag{3.49}$$

yielding the NTV torque density t_NTV with Γ_i a radial non-ambipolar ion particle flux, defined as $\langle n_i \vec{v}_i \vec{e}_\mathrm{r} \rangle$.
In the core region plasmas are mainly in the low-collisitionality banana regime. In this regime the particles finish at least one banana orbit before they collide with another particle and therefore, the effective ion-ion collision frequency is less than the banana bounce frequency ($\nu_\mathrm{i}^* = \nu_\mathrm{ii}/(\epsilon\omega_\mathrm{b}) \ll 1$, with $\omega_\mathrm{b} = \epsilon^{1/2} v_\mathrm{th}/(qR)$ and v_th the thermal velocity). In the banana regime trapped particles dominate the transport. Two collisionality regimes exist within the banana regime. These two sub-regimes are: the $1/\nu$ regime for ($\nu_\mathrm{ii}/\epsilon > q\omega_\mathrm{ExB}$) and the ν regime for ($\nu_\mathrm{ii}/\epsilon < q\omega_\mathrm{ExB}$) with ω_ExB the $\vec{E} \times \vec{B}$ drift frequency defined as E_r/rB_{tor}, with E_r the radial electric field. In the investigated plasmas, the core region is mainly near the transition from the $1/\nu$ and ν regime. In the following and in section 5.3 the formulae and parameter definitions for the $1/\nu$ regime are used. In the regimes valid for higher collisionality for example at the edge, like the plateau and Pfirsch-Schlüter regime [3], the drift of trapped particles is reduced - due to less trapped particles. Therefore, the presented calculation, valid for the banana regime, provides an upper limit for the NTV torque.
The radial ion flux Γ_i can be calculated in the relevant collisionality regime. It is connected to the toroidal viscous stress and the corresponding NTV torque density t_NTV. Calculating the radial ion particle flux for the $1/\nu$ regime leads to the generic formulation for the toroidal NTV torque density [59, 60, 49]

$$t_\mathrm{NTV} \simeq m_\mathrm{i} n_\mathrm{i} \frac{\epsilon^{3/2} v_\mathrm{th,i}}{\nu_{ii} \langle R^2 \rangle} \left(\frac{\delta B}{B_0} \right)^2 \langle R^2 \rangle \left(\Omega_\phi - \Omega_\mathrm{NC}^* \right), \tag{3.50}$$

with m_i and n_i the ion mass and density, $v_\mathrm{th,i}$ the thermal ion velocity ($\sqrt{2T_\mathrm{i}/m_\mathrm{i}}$), ν_{ii} the ion-ion collision frequency, Ω_ϕ the plasma rotation frequency and Ω_NC^* a neoclassical offset frequency. Additionally the NTV depends on the ratio of the perturbation field (δB) and the equilibrium field (B_0). The NTV acts as drag and tries to slow down the plasma rotation Ω_ϕ towards Ω_NC^*. The offset rotation Ω_NC^* is in the counter-current direction for static MPs and depends on the ion temperature gradient [61, 62]. The detailed dependence is given in equation (5.26). The total torque can be calculated by integrating t_NTV over the plasma volume V. A detailed calculation of the NTV can be found in section 5.3. This is done by taking into account that the B-coils produce a perturbation field which is located mainly at the low field side and that the plasmas are divertor plasmas. This is not taken into account in most of the calculations at other devices, where a helical perturbation and a cylindrical plasma is assumed.

3.5 Mode rotation

In addition to the evolution of the island width, the evolution of the phase of a mode is also important. In the laboratory frame an island structure rotates with the electron fluid, which differs in rotation frequency from the main plasma rotation frequency Ω_i. The plasma rotation in the case of AUG is dominated by the toroidal ion rotation frequency $\Omega_{i,\phi}$ ($=v_{\mathrm{tor}}/R$) which can be measured by means of the CXRS diagnostic (cf. section 2.3.7). It is assumed that the poloidal ion plasma rotation is strongly damped [63] and that only the toroidal plasma rotation is important. In contrast, the poloidal and toroidal rotation of a magnetic island are always coupled via the safety factor q. At the resonant surface the balance between the electromagnetic field and the pressure gradient leads to a rotation of the magnetic island with the electron perpendicular velocity $v_{\perp,\mathrm{e}}$. In general, for both the electron and ion fluids, only the rotation perpendicular to the magnetic field lines are important. $v_{\perp,\mathrm{e}}$ is the sum of the $\vec{E}\times\vec{B}$ drift velocity $\vec{v}_{\mathrm{ExB}}=\vec{E}\times\vec{B}/B^2$ and the electron diamagnetic drift velocity $\vec{v}_{\mathrm{e}}^*$, which leads to the following relation for the mode frequency

$$\omega \approx \vec{k}(\vec{v}_{\mathrm{ExB}}+\vec{v}_{\mathrm{e}}^*) \tag{3.51}$$

$$\tag{3.52}$$

with the wave vector $\vec{k}$ defined as $(n/R\vec{e}_\phi + m/r\vec{e}_\theta)$. The diamagnetic drifts are caused by the existence of a pressure gradient ($\vec{v}^* = \vec{\nabla}p\times\vec{B}/(qnB^2)$) and give rise to a diamagnetic current via $\vec{j}_{\mathrm{dia}} = ne(\vec{v}_{\mathrm{i}}^* - \vec{v}_{\mathrm{e}}^*)$. Neglecting the poloidal component of the plasma rotation and assuming that the diamagnetic drift frequency $\Omega_{\mathrm{i,e}}^*$ for ions and electrons is mainly in the poloidal direction yields

$$\omega \;=\; n\Omega_{i,\phi} - m\Omega_{\mathrm{i}}^* \tag{3.53}$$

$$\Omega_{\mathrm{i}}^* = -\Omega_{\mathrm{e}}^* \;=\; -\frac{\nabla p_{\mathrm{e,i}}}{|q_{\mathrm{e,i}}|n_{\mathrm{e,i}}B_{\mathrm{tor}}r}. \tag{3.54}$$

The rotation ω of a small magnetic island in the laboratory frame, where the local radial magnetic field is zero, differs from $\Omega_{i,\phi}$ by about the poloidal component of the ion diamagnetic drift frequency $\Omega_{\mathrm{i}}^* = v_{\mathrm{i}}^*/r$ [64]. For normal operation, with a co-current rotating plasma, the ion diamagnetic frequency is positive and the mode rotates slower compared to the plasma. The propagation of a small island with respect to the plasma frame is the same mechanism that gives rise to the polarisation current, which influences the island stability as already discussed in section 3.2.2. For large islands the pressure gradient at the resonant surface vanishes and, hence, $\Omega_{\mathrm{i}}^* = 0$. So large islands rotate with the plasma and do not 'slip' trough the plasma.

3.6 Equation of motion

The time evolution of the island frequency can be described by the equation of motion, including all torques acting on the island. Assuming that the Ω_{i}^* is constant, changes in the island rotation are caused by changes in the plasma rotation at the resonant surface. Again, assuming poloidal flow damping [63], the poloidal component of the equation of motion can be neglected and from the toroidal component of the equation of motion, the mode rotation can be derived:

$$I\frac{d\omega}{dt} = \sum T_\phi \tag{3.55}$$

Any torque which is not balanced by other torques contributes to the inertia $I = m_{\text{plasma}} R_0^2$, which gives rise to a change in the mode frequency, with m_{plasma} the mass of the plasma.

3.6.1 Viscous torque

In addition to the $(\vec{j} \times \vec{B})$ and NTV torques caused by the externally applied magnetic perturbations (section 3.4), the viscous torque T_{vs} and the NBI input torque T_{NBI} (see section 2.2.1) also strongly influence the island rotation.
The plasma cross-sections (referred to as 'plasma shells' with volume dV and width dr) are radially coupled via a perpendicular plasma viscosity. This gives rise to a viscous torque, where the toroidal component can be described as [37, 40]

$$T_{\phi,\text{vs}}|_{dV} = 4\pi^2 R_0 \left[(D_\phi \rho r R_0^2) \frac{\partial \Omega}{\partial r} \right]_{r-dr/2}^{r+dr/2}, \tag{3.56}$$

with D_ϕ the momentum diffusion coefficient and ρ the mass density, where the product of both is proportional to the perpendicular viscosity. A radial gradient in the rotation profile gives rise to a restoring torque between the different plasma shells along r with the Volume $dV = V(r + dr/2) - V(r - dr/2)$. For a large island, which is not allowed to 'slip' through the plasma ($\Omega_\text{i}^* \approx 0$), only the deviation from its natural frequency ω_0 is important. The natural frequency is defined as the mode rotation in a steady-state situation where the global viscous and NBI input torque balance each other. Every deviation of ω from ω_0 is opposed by the perpendicular viscosity which gives rise to the corresponding restoring torque. The torque can be derived from the following approximation, assuming that changes in the mode rotation are caused by changes in the toroidal plasma rotation Ω_ϕ [40]

$$T_{\phi,\text{vs}} = A \Delta \Omega_\phi = A \frac{1}{n} (\omega - \omega_0). \tag{3.57}$$

The parameter A depends on viscosity and properties of the natural velocity profile.

3.6.2 Resistive wall torque

In addition also the existence of a resistive wall can influence a magnetic island. This influence is described in this section, following the derivation in [65]. The resistive wall is important mainly for slowly rotating islands. The presence of a resistive wall results in a $\vec{j}_{\text{wall}} \times \vec{B}(r_{\text{wall}})$ torque. The wall is located at $r = r_{\text{wall}}$ with a finite conductivity σ. At the resonant surface, inside a magnetic island, a perturbed helical current j_1 is flowing. Its phase varies in time ($\sim e^{i(m\xi - \omega t)}$) with respect to the wall, according to the mode frequency ω, with m the poloidal mode number. Outside the resonant surface the perturbed current is zero. Consequently, the perturbed field in these regions ($r \neq r_{\text{res}}$) can be described by Ampère's law (see equation (3.1)). The poloidal and radial component of $\vec{B}_1$ can be calculated by including the correct boundary conditions for the radial and tangential component of $\vec{B}_1$ in the three regions ($0 < r < r_{\text{res}}$), ($r_{\text{res}} < r < r_{\text{wall}}$) and ($r_{\text{wall}} < r < \infty$). Here, additionally, the perturbed current flowing at the resonant surface has to be taken into account. In order to determine the shielding current j_{wall} induced in the wall by the rotating mode, the tearing mode equation has to be solved, accounting for the above described boundary conditions. An approximation for j_{wall} can be calculated from Faraday's law, using the perturbed radial magnetic field $B_{1\mathrm{r}\infty}$ in the outer region $r_{\mathrm{wall}} < r < \infty$:

$$j_{\mathrm{wall}} = \frac{r_{\mathrm{wall}}\omega\sigma_{\mathrm{wall}}}{m} B_{1\mathrm{r}\infty} \tag{3.58}$$

$$B_{1\mathrm{r}\infty} = -\frac{B_1}{i_\omega \tau_{\mathrm{wall}}} \left(\frac{r_{\mathrm{res}}}{r}\right)^{m+1} e^{i(m\xi - \omega t)} \tag{3.59}$$

The time τ_{wall} is the resistive time of the wall with width d, defined as $\tau_{\mathrm{wall}} = \mu_0 d r_{\mathrm{wall}} \sigma_{\mathrm{wall}}/(2m)$. The ASDEX Upgrade vessel wall is made out of steel ($\sigma_{\mathrm{wall}} = 10^7\, 1/m\Omega$) and located at a minimum radius r_{wall} of 0.5 m with a thickness of around $d = 15\,\mathrm{mm}$ on average. In a circular approximation this results in τ_{wall} of 50 ms for a mode with $m = 1$.
The force acting on the island can be calculated using equation (3.58) and (3.59) via

$$F_{\mathrm{wall}} = \vec{j} \times \vec{B} = \frac{1}{2} j_{\mathrm{wall}} B^{*}_{1\mathrm{r}\infty}, \tag{3.60}$$

with $B^{*}_{1\mathrm{r}\infty}$ the conjugated of $B_{1\mathrm{r}\infty}$. This results in the equation for the toroidal component of the resistive wall torque $T_{\phi,\mathrm{rw}}$ [65, 34, 37]

$$T_{\phi,\mathrm{rw}} = -4\pi^2 R_0^2 \frac{m^2}{\mu_0 r_{\mathrm{res}}} \left(\frac{r_{\mathrm{res}}}{r_{\mathrm{wall}}}\right)^{2m} \frac{(\omega\tau_{\mathrm{wall}})}{1 + (\omega\tau_{\mathrm{wall}})^2} C^2 W^4 \frac{1}{\sqrt{(\epsilon/q)^2 + 1}}. \tag{3.61}$$

The parameter C is defined in equation (3.38). The last term in equation (3.61) results from the extraction of the toroidal component from the total helical torque, which contains both a poloidal and a toroidal component.
Since the helical current flowing in the wall contains a component which is in phase ($\cos(m\xi)$ component) with the perturbed flux, the resistive wall can also contribute to the island evolution [37]

$$\Delta_{\mathrm{rw}} = -\frac{2m}{r_{\mathrm{res}}} (\omega\tau_{\mathrm{wall}})^2 u \frac{[1-u]}{1 + (\omega\tau_{\mathrm{wall}})^2 [1-u]}. \tag{3.62}$$

The parameter u is defined as $u = (r^{+}_{\mathrm{res}}/r_{\mathrm{wall}})^{2m}$. This contribution adds to the modified Rutherford equation:

$$a_1 \tau_{\mathrm{res}} \frac{dW}{dt} = r_{\mathrm{res}}^2 \Delta'(W) + r_{\mathrm{res}}^2 \Delta_{\mathrm{bs}} + r_{\mathrm{res}}^2 \Delta_{\mathrm{pol}} + r_{\mathrm{res}}^2 \Delta_{\mathrm{ext}} + r_{\mathrm{res}}^2 \Delta_{\mathrm{rw}} \tag{3.63}$$

3.7 Summary

The evolution of a magnetic island can be characterised by the evolution of the island width and its phase. The evolution of the island width can be described by the modified Rutherford equation. Every parallel current with a $\cos(m\xi)$ component can influence the island evolution, either stabilising or destabilising. Modes that are driven by the equilibrium current profile (Δ' unstable) are called classical tearing modes. Neoclassical tearing modes are typically Δ' stable, and are driven by the loss of bootstrap current. Additionally, due to small island effects a threshold for the mode onset exists. This implies the requirement of a 'seed' island at the resonant surface, which can be induced by a trigger instability at a different surface. Including all contributions discussed in the previous sections in the modified Rutherford equation that describes the evolution of the island width W yields:

$$0.82\tau_{\mathrm{res}}\frac{dW}{dt} = r_{\mathrm{res}}^2\Delta'(W) + r_{\mathrm{res}}^2\Delta_{\mathrm{bs}} + r_{\mathrm{res}}^2\Delta_{\mathrm{pol}} + r_{\mathrm{res}}^2\Delta_{\mathrm{ext}} + r_{\mathrm{res}}^2\Delta_{\mathrm{rw}} \tag{3.64}$$

The frequency evolution of a magnetic island can be derived from the equation of motion by including all torques acting on the island. Assuming poloidal flow damping, only the toroidal components of the torques influence the island evolution. These are summarised in the following equation of motion for the island frequency ω:

$$I\frac{d\omega}{dt} = T_{\phi,\mathrm{vs}} + T_{\phi,\mathrm{NBI}} + T_{\phi,\mathrm{jxB}} + T_{\mathrm{NTV}} + T_{\phi,\mathrm{rw}} \tag{3.65}$$

These equations are used in the following to discuss the influence of rotation on the NTM onset (chapter 4) and to model the influence of MPs on the NTM evolution (chapter 5).

Chapter 4

Influence of rotation on the NTM onset

4.1 Introduction

As already introduced in chapter 3 neoclassical tearing modes (NTMs) are resistive MHD-instabilities. They are driven by a loss of helical bootstrap current which is caused by a flattening of the pressure profile across the magnetic island due to enhanced transport around the island. Once a seed island of sufficient size is generated, this mechanism reinforces itself and the NTM grows. In present devices the occurrence of NTMs degrades the confinement and limits the maximal achievable β. NTMs can decrease the plasma rotation and can even lead to disruptions in particular at low q_{95}, deifned as q at 95% of the poloidal flux Ψ. In large devices like ITER NTMs are likely to be performance limiting if they are not mitigated or avoided. To be able to control NTMs it is necessary to extrapolate the present understanding to larger devices with different conditions. A key parameter for the NTM physics and extrapolation is the rotation dependence. Compared to present devices, which typically have substantial rotation, ITER will be operated at low plasma rotation due to a low applied torque compared to the plasma viscosity. With these differences the question arises, how the NTM behaviour changes with rotation and, if predictions can be made from present understanding. In addition to this, the general dependence of NTMs on different plasma parameters, especially the understanding of the seeding mechanism and the dependences at the NTM onset are an essential part for the control and avoidance of NTMs. The main part of this chapter has already been published in [66].

4.2 Role of rotation and previous work

In the following, the question of how the plasma rotation influences the onset and the trigger process of NTMs is adressed. Several possibilities of how plasma rotation can influence the NTM behaviour.

- It has been proposed that changes in rotation or rotation shear can reduce the normally stabilising effect of the classical tearing stability index Δ', due to a change in the interaction of the resonant surfaces or reduction of rotation shear in the vicinity of the resonant surface [67].

- Rotation can also influence the stability of NTMs by means of small island effects. The ion polarisation current for example depends explicitly on rotation and can be influenced by changes of the mode rotation in the plasma frame, to either stabilise or destabilise the island [68, 50]. Of course this rotation effect depends strongly on the general impact of the ion polarisation current on the mode stability compared to other small island effects.

- A further important issue is the effect of rotation on the trigger mechanism. On the one hand, the trigger instability itself can depend on plasma rotation as already found for the sawtooth instability [69, 70]. On the other hand the seeding process due to magnetic coupling can be influenced by the differential rotation between the two resonant surfaces [71]. The formation of a seed island will be hampered at high differential rotation because the seed perturbation is shielded.

- Finally, rotation can influence the island stability due to changes of the impact of error fields on the island or due to changes in the interaction between the island and the vessel wall, as already introduced in section 3.4 and section 3.6.2, respectively. Changes in the island structure due to rotation are also possible.

Studies concerning the rotation dependence of NTMs have already been performed at several other fusion experiments e.g. DIII-D [73], NSTX [74], JET [72, 67].
At DIII-D, experiments with co- and counter-current injected beam torque were done. At NSTX only co-rotation data are available, which were obtained from experiments in which the plasma rotation was varied via different co-injected beam torques and with an externally applied error field that acts as a drag on the plasma rotation. The JET database also contains only co-rotation data achieved with a mix of NBI and ICR heating. In all three devices it was found that with decreasing co-rotation or rotation shear the NTM onset threshold decreases and that the role of rotation shear on the NTM stability is more important than that of rotation alone. At DIII-D, the NTM onset threshold decreases further with increasing counter-rotation, shown in figure 4.1. Similarly, for decreasing rotation shear, the onset threshold decreases continuously, also when entering the region of negative rotation shear,

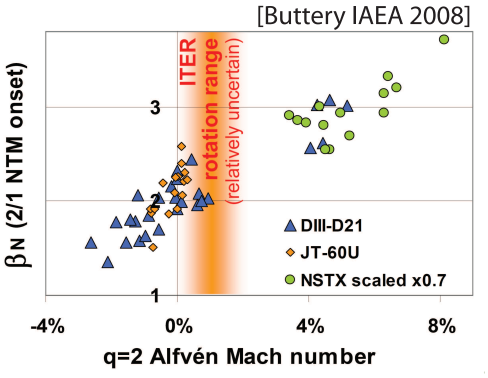

Figure 4.1: Figure taken from Buttery IAEA 2008 [72]. Rotation dependence of 2/1 NTM β_N limit.

which is related to counter-rotation. This raised the question of whether a sign effect is responsible for the different behaviour with co- and counter-rotation or, if the minimum onset threshold is shifted towards negative rotation which would indicate that an 'offset' exists which is caused by diamagnetic drifts [67]. If this is the case, it is possible that this minimum in rotation has not been reached yet at DIII-D. Even stronger counter-current rotation data are needed to cross this minimum. Further, in [73] and [74] experiments were performed which exclude the influence on the ion polarisation current on the NTM onset threshold. Results from DIII-D and NSTX suggest that an influence of rotation or rotation shear on the underlying tearing stability (Δ') exists which is responsible for the rotation dependence of the NTM onset threshold [73, 67].

In the following the corresponding results from AUG for the (3,2) NTM onset are presented which differ in some respect from those at DIII-D and NSTX.

4.3 Experimental approach

The growth of an NTM can be described by the modified Rutherford equation [38, 75] as already introduced in section 3.2.2. The drive of the NTMs, which determines the NTM threshold, is mainly caused by the loss of bootstrap current inside the island. In the following analysis an NTM threshold is defined with respect to $\mu_0 L_\mathrm{q} \delta j_\mathrm{bs}/B_\mathrm{pol}$ according to [74]. Since at AUG the q profile measurements are insufficient to reliably detect changes in dq/dr, the dependences on $q(r)$ are not included in all following definitions (meaning L_q=constant).

According to equation (3.31), except for the ion polarisation current, which is not responsible for the rotation dependence at the mode onset as already mentioned and discussed in [73, 67], no explicit rotation dependence is included in the modified Rutherford equation.

In the experimental analysis different trigger mechanisms have been distinguished which, due to magnetic coupling, induce a seed island at the resonant surface (see section 3.3). For most of the discharges the trigger mechanism could be identified unmistakably as either an ELM, a fishbone or a sawtooth crash. This was extended to clarify if there exists a clear correlation between the NTM onset and the characteristic features of each trigger mechanism (see figure 3.5). The cases, in which the mode grows without any visible trigger, possibly destabilised by the T_e gradient [76], are also common. For some NTM onsets (1,1) activity was observed but the trigger mechanism could not be specified. In those cases in which multiple events took place at the mode onset the trigger mechanism is labelled as 'unclear'.

For some islands also the marginal point could be determined (figure 3.4). Dependences at the marginal point are exclusively caused by effects included in the modified Rutherford equation and are therefore independent from the seeding physics. The trigger mechanism does not influence the behaviour at the marginal point. In consequence by analysing the NTM behaviour at the marginal point effects attributed to the trigger mechanism and the NTM stability can be disentangled.

During the decay phase of stored energy and hence β_pol, e.g. due to ramping down the heating power, also the island width decreases, as illustrated in figure 3.4. At the marginal point the island width evolution decouples from β_pol and decays away independent of β_pol.

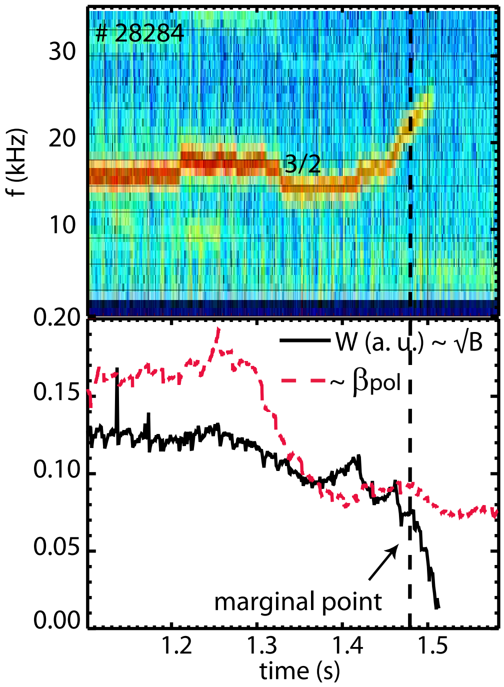

Figure 4.2: Illustration of the marginal point determination of a (3,2) neoclassical tearing mode by the decoupling of $\beta_{\rm pol}$ and the island width evolution

This is illustrated for one case in figure 4.2. For simplicity in this investigation the time evolution of the global $\beta_{\rm pol}$ is used and not the local one at the resonant surface like in all other analyses.

The marginal point can be determined best, when $\beta_{\rm pol}$ decreases very slowly. Therefore in all dedicated experiments a slow power ramp down was included.

At AUG the (m,n)=(3,2) NTM is the most common NTM and hence a large data set of (3,2) NTM onset points with a wide range of plasma rotation is available. To extend the database, especially in the low rotation regime and with counter-rotation, dedicated experiments have been carried out. In these experiments the plasma rotation was varied by using different heating mixes. Two wave heating methods, ECRH (electron cyclotron resonance heating max. 4 MW) and ICRH (ion cyclotron resonance heating max. 6 MW) are available, neither of which apply a direct torque on the plasma. The torque input can be varied by using the neutral beam injection (NBI max. 20 MW) and combining radial and tangential beams. The experiments carried out to achieve the lowest possible rotation were done with a dominant fraction of wave heating and only one neutral beam that is necessary for rotation measurements. The beam was operated at reduced beam voltage, which reduces the input power and also the input torque. In standard operation the NBI is oriented in the co-direction relative to the plasma current. Experiments with counter-rotation can be obtained by reversing the plasma current and the magnetic field direction. In this setup the NBI is oriented in the counter-current direction. The experiments with counter-rotation were limited in NBI heating power due to impurity influx created by enhanced first orbit losses in reversed $I_{\rm p}/B_{\rm tor}$ operation. This is caused by the fact, that in counter-current direction more ions are born at non-confined orbits. In reversed $I_\mathrm{p}/B_\mathrm{tor}$ operation the drift direction of trapped particles is changed towards the outboard side, while in normal operation these drifts are towards the plasma core. As a consequence, the range of achievable counter-rotation data was limited. For the following investigations all parameters are taken at the location of the magnetic island. The radial island location has been determined by using the SXR diagnostic (section 2.4.1) and a localisation method, which is based on the correlation of the ECE channels measuring the electron temperature T_e with a sampling rate of 1 MHz and the magnetic signals dB/dt [30] (section 2.4.4). The second method is very reliable and accurate and works satisfactorily for most of the discharges. The toroidal plasma rotation v_tor is measured via charge exchange recombination spectroscopy (CXRS) (section 2.3.7).

4.3.1 Machine limit

In one of the following analysis the normalised β_N threshold at the NTM onset is compared to the maximal achievable β_N, which is only limited by the achievable heating power and other plasma parameters, like I_p, B_t and n_e which are all set as input to the experiment. Since the used heating power does not only influence β_N, but also determines the plasma rotation, a trivial dependence of both parameters could be expected.

Therefore, the machine limit is introduced, which in this context is the hypothetical achievable data range of β_N and plasma rotation. This predicted limit can hence be compared to the analysis result in order to exclude trivial dependences and to illustrate the influence of NTMs on the overall plasma performance. The hypothetical data range is predicted by taking into account scalings and simple formulae depending only on parameters which are set from outside, such as the available heating power P_heat, I_p, B_tor and density n_e.

The achievable β_N is defined as [3]:

$$\beta_\mathrm{N} = \frac{\beta_\mathrm{tor}}{I_\mathrm{p}(MA)/(a(m)B_\mathrm{tor}(T))} = \frac{1}{I_\mathrm{p}(MA)/(a(m)B_\mathrm{tor}(T))}\frac{< p_\mathrm{tot} >}{B_\mathrm{tor}^2/2\mu_0} \tag{4.1}$$

where the definition of β_tor, defined as $< p > /(B_\mathrm{tor}^2/2\mu_0)$, has been used. The pressure $< p_\mathrm{tot} >$ can be determined from the stored energy W_tot, which on the other hand depends on the total power and the energy confinement time τ_e [3]:

$$W_\mathrm{tot} = \tau_\mathrm{e} P_\mathrm{tot} = \int 3/2 p_\mathrm{tot} dV \tag{4.2}$$

The ITERH-98P(y,2) confinement scaling [77] is used to determine the energy confinement time, assuming an H_{98} factor of 1 ($H_{98} = \tau_\mathrm{e}/\tau_\mathrm{scal}$).

$$\tau_\mathrm{scal} = 0.0526 P_\mathrm{tot}^{-0.69} B_\mathrm{tor}^{0.15} I_\mathrm{p}^{0.93} \kappa^{0.78} n_\mathrm{e}^{0.41} \epsilon^{0.58} R^{1.97} M^{0.19} \tag{4.3}$$

For the elongation κ (=0.74), the inverse aspect ratio ϵ (=a/R=0.3), and the mass number M (=2), typical AUG values are used, indicated in brackets. The total power P_tot is assumed to be dominated by the total externally applied heating power $P_\mathrm{heat} = P_\mathrm{NBI} + P_\mathrm{ICRH} + P_\mathrm{ECRH}$.

Combining equation (4.1), (4.2) and (4.3) leads to a prediction for β_{N} depending only on parameters, which can be set in the experiment

$$\beta_{\mathrm{N}} = \frac{2/3\ \tau_{\mathrm{scal}} P_{\mathrm{heat}}}{I_{\mathrm{p}}[mA] B_{\mathrm{tor}}/(a2\mu_0)} \frac{1}{V}. \tag{4.4}$$

The plasma rotation is determined by the intrinsic rotation and the applied torque. It is assumed that the intrinsic rotation is negligible and that only the NBI applies a torque to the plasma. The decrease of rotation due to ECRH and ICRH observed in experiment is not included explicitly, but the trend of decreasing plasma rotation with increasing wave heating power is taken into account, as will be described later. The torque balance equation delivers an expression for the plasma rotation frequency ω, which depends on the NBI input torque and the momentum confinement time τ_Φ:

$$T_{\mathrm{NBI}} = \frac{m_{\mathrm{plasma}} R^2 \omega}{\tau_\Phi} \tag{4.5}$$

The NBI input torque is the sum of the individual beams i with power $P_{\mathrm{NBI,i}}$ which can be approximated according to [78] and [79]

$$T_{\mathrm{NBI}} = P_{\mathrm{NBI,i}} \sqrt{\frac{2 m_{\mathrm{beam}}}{E_{\mathrm{b}}}} R_{\mathrm{tang}}, \tag{4.6}$$

with E_{b} the injection energy, m_{beam} the mass of the beam species and R_{tang} the tangential radius of the NBI beams. Detailed information on the AUG NBI system is given in section 2.2. Combining equation (4.5) and (4.6) delivers a prediction for the toroidal plasma rotation at the position $\langle R(q = 3/2)\rangle$, with the profile factor c=1.23 for the q=3/2 surface determined in previous studies by H. Zohm [78]

$$v_{\mathrm{tor}} = c \frac{T_{\mathrm{NBI}} \tau_{\mathrm{e}}}{m_{\mathrm{plasma}} R}. \tag{4.7}$$

For this calculation it is assumed that τ_Φ is equal to τ_{e}, which can be calculated using equation (4.3). As mentioned before, in this expression the trend of decreasing plasma rotation with increasing wave heating power is included implicitly in the following way: increasing the wave heating power, and leaving all other input quantities constant, yields a lower v_{tor} due to a lower $\tau_{\mathrm{e}} \propto P_{\mathrm{tot}}^{-0.69}$ whereas the β_{N} increases due to the direct dependence on P_{tot}.

Using equation (4.4) and (4.7) the machine limit can be determined, scanning through the achievable parameter range in β_{N} and v_{tor} varying the heating power while using different combinations of wave and NBI heating power. The maximal heating power consists of 20 MW NBI and additionally 10 MW delivered by ICRH and ECRH together. Additionally different combination of $B_{\mathrm{tor}}\,(T) = [2.0, 2.5]$, $I_{\mathrm{p}}\,(MA) = [0.8, 1.0]$ and $n_{\mathrm{e}}\,(10^{19}\,m^{-3}) = [4, 7, 10]$ are used.

4.4 Experimental results

In this section the influence of the toroidal rotation velocity on the NTM onset threshold is investigated, based on a data set including around 70 discharges. A statistical analysis

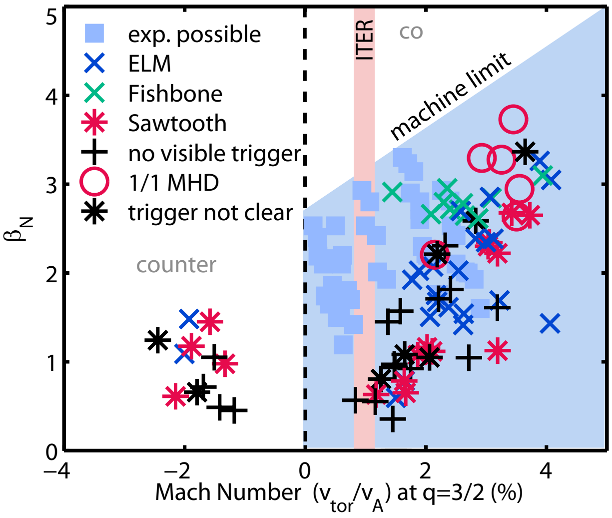

Figure 4.3: Normalised β_N at the onset of (3,2) NTMs versus the toroidal rotation velocity normalised to the Alfvén velocity at the resonant surface. The symbols indicate the different trigger mechanisms. The machine limit, indicating the hypothetical experimentally achievable data range is also shown. The grey-blue boxes indicate the experimentally possible data range.

of all dependencies shown in this section is presented in table 4.1, where all the correlation coefficients are listed for comparison. A correlation coefficient of 1 is the result of a clear linear dependence, which is represented by a straight line. A correlation coefficient of zero characterises a scattered cloud of points, hence indicates that no dependence exists. But, if the data set contains a too small amount of data points or if the data range is too small no statement from the correlation analysis can be made, hence the correlation analysis is 'insignificant'.

In the following, similar to studies at other devices, the rotation velocity is normalised to the Alfvén velocity ($v_\mathrm{A} \sim \langle B_\mathrm{tor}\rangle / \sqrt{\mu_0 n_\mathrm{i} m_\mathrm{i}}$, with B_tor the toroidal magnetic field, n_i the ion density, m_i the ion mass and μ_0 the magnetic vacuum permeability), due to the larger scatter in the dependence of the NTM onset threshold on toroidal rotation alone. This normalised quantity is defined as the Alvén Mach number Ma_A. In figure 4.3 the global β_N at the NTM onset is plotted against the normalised rotation. The hypothetical achievable parameter range in β_N and Ma_A (area below the machine limit), which is estimated according to section 4.3.1 is also indicated . The calculated data points are shown as grey-blue boxes in figure 4.3 which indicates the hypothetical experimentally achievable data range. In figure 4.3 the β_N at the NTM onset increases linearly with increasing normalised plasma rotation for co- and counter-rotation. This is more distinct for the co-current rotation data, which can also be seen from the correlation analysis presented in table 4.1, but however, the trend is also visible for counter-current rotation. Additionally, it is clearly visible that the NTMs limit the maximal achievable β_N and hence, limit the plasma operation below the machine limit. Heating with NBI not only increases β_N, but also exerts a torque on the plasma and increases plasma rotation. The fact that the machine limit is higher than the achievable β_N indicates that the linear dependence of the rotation velocity on β_N at the NTM onset is

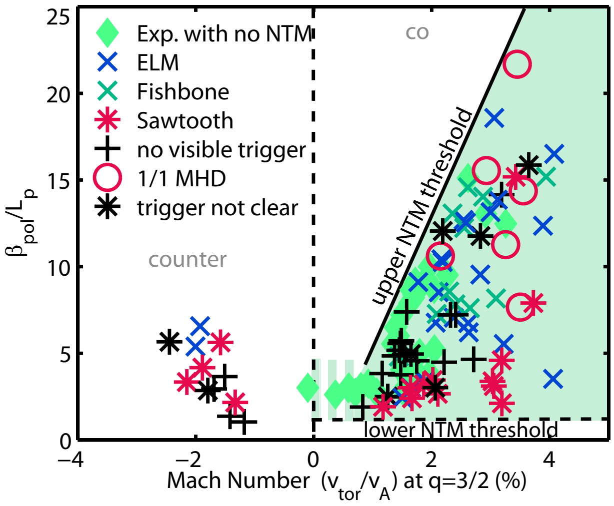

Figure 4.4: (3,2) NTM onset threshold, in terms of $\beta_{\text{pol}}/L_{\text{p}}$, versus the toroidal rotation velocity divided by the Alfvén velocity at the resonant surface. The symbols indicate the different trigger mechanisms. Additionally, data points without NTMs are shown as green diamonds.

not trivial. Considering that the NTM onset threshold can be described more accurately by the perturbation of the bootstrap current inside the island, which is proportional to $\beta_{\text{pol}}/L_{\text{p}}$, another analysis method using local parameters is shown in figure 4.4. In this plot additional data points from different discharges where no NTM is present are included. An upper NTM onset threshold is clearly visible in this analysis, which linearly increases with Ma_{A} in the region of high rotation. All of the data points, including the NTM onset data and the data without NTMs, are situated below this threshold in the metastable region. This means that plasma operation is ultimately limited by NTMs when this threshold is reached and that the region above this threshold cannot be realised in experiment. This is different when the resonant q surface is not present or the NTM is actively stabilised. The lower NTM threshold, which defines the minimum required drive for the occurrence of an NTM and can in principle be explained by the modified Rutherford equation, seems not to depend on rotation. In the region of low normalised rotation (<1 Ma_{A}), where the intersection of the upper and lower threshold should be, the upper threshold seems not to depend on rotation anymore. In this region of low rotation the discharges are mainly heated by wave heating, which seems to change the NTM stability behaviour or the trigger mechanisms and blurs the boundaries.

The scatter of the NTM onset data in the metastable region (green coloured area) is caused by the different trigger events. The trigger process is different for every NTM onset, even if the triggering instability is the same, and hence leads to different seed island sizes and in consequence different onset thresholds as long as $W_{\text{seed}} \geq W_{\text{crit}}$. Although the counter-current rotation data is limited, also with this analysis method a trend towards increasing co- and counter-rotation with increasing NTM onset threshold is visible. This leads to a minimum threshold in the region of zero rotation. For co-current rotation this trend can also be seen for all of the different trigger sub-sets (compare table 4.1). The increase with counter-current rotation disagrees with the experiments at DIII-D, where a further decrease of the

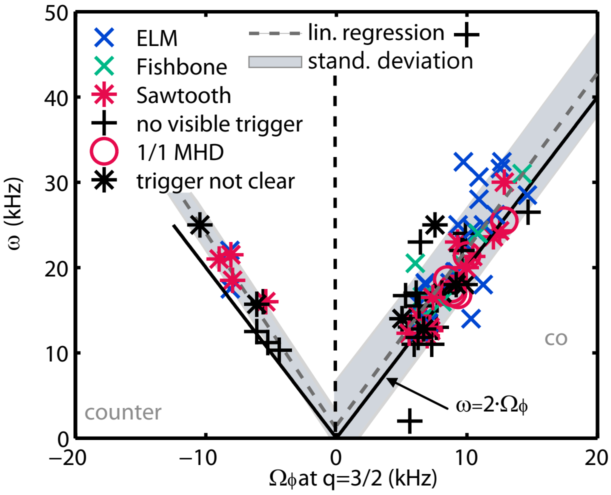

Figure 4.5: Comparison of the plasma toroidal rotation frequency Ω_ϕ at the q=3/2 surface measured with CXRS at the onset of the NTMs and the frequency ω of the NTM at the onset. A linear regression fit (dashed line), the standard deviation (grey shaded area) and the relation $\omega = 2 \times \Omega_\phi$ (straight line) are also indicated

onset threshold with counter-current rotation was found (compare figure 4.1). As already mentioned in previous works it was suggested that an offset of the threshold minimum exists which was not reached at DIII-D [67]. According to [80] the correct parameter to investigate the dependence of the NTM onset threshold on rotation is the velocity of the island ω, not the plasma rotation. This leads to a correction of the plasma rotation at the resonant surface $\Omega_\phi(r_{\mathrm{res}})$ by the ion diamagnetic drift frequency Ω_{i}^*, defined in equation (3.54). Considering this corrected island rotation, an offset as observed at DIII-D, can be explained. The island rotation frequency in the laboratory frame is defined in equation (3.55). As discussed in [67] this expression leads to a finite ω in counter current direction, even if $\Omega_\phi(r_{\mathrm{res}})$ is zero and in consequence for $\omega = 0$ an offset in the counter direction at $\Omega_\phi(r_{\mathrm{res}}) \approx \Omega_{\mathrm{i}}^*(r_{\mathrm{res}})$ exists.
In figure 4.5 the mode frequency ω at the onset is plotted against the toroidal plasma rotation frequency Ω_ϕ at the resonant surface at the time of the NTM onset. A linear regression fit is also indicated together with the corresponding standard deviation (grey shaded area). Referred to theory the difference of this fit and the assumption $\omega = n \cdot \Omega_\phi(r_{\mathrm{res}})$ is due to the ion diamagnetic drift frequency (cp. equation 3.55). For co-current rotation the diamagnetic contribution leads to slower mode rotation compared to plasma rotation, whereas for counter-current rotation the mode would rotate faster than the plasma. Since the difference of the mode and the plasma rotation is within the standard deviation, as shown in figure 4.5, the ion diamagnetic drift frequency is smaller than the error bars of the analysis at least for the co-current rotation data. For the counter-current rotation points a small ion diamagnetic drift frequency could exist, but due to the small amount of data points here this observation is marginal and it is hard to draw any conclusion. Concluding from the observations of the co-current data the ion diamagnetic drift frequency is smaller than the uncertainties of the frequency measurements and no obvious offset of the threshold minimum in figure 4.4 is expected. The data show a clear linear dependence of the onset threshold with co- and

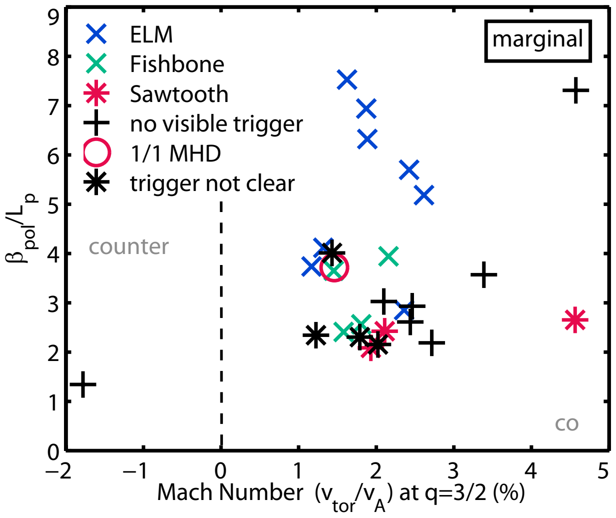

Figure 4.6: (3,2) NTM threshold at the marginal point versus the toroidal rotation velocity divided by the Alfvén velocity at the resonant surface. The symbols indicate the different trigger mechanisms.

counter-current rotation. On the bases of these observations, it would be worth to look again in the DIII-D database to clarify, if there really an offset exists, which is not reached yet, or a new interpretation of the data, could lead to an agreement with the results presented here. Plotting the NTM onset threshold against Ma_{A} it is noteworthy that in the region of low rotation NTMs are mostly triggered by a sawtooth crash or appear without any trigger. This can be seen in both figure 4.4 and figure 4.3. It is well known that a sawtooth crash can lead to a strong perturbation at the resonant surface and this results in a low NTM threshold. In contrast, based on the fact that the triggerless case is seen as the weakest trigger mechanism, one would expect these cases to have a higher onset threshold. From this discrepancy one can infer that there exists an influence of plasma rotation on the underlying tearing stability. It is observed that the Δ' term is very sensitive even to small changes of the current profile close to the resonant surface. Therefore it is possible that at lower plasma rotation the Δ' term changes such that the plasma is less stable against (N)TMs as already proposed in [73] and [67]. This leads to a less stabilising Δ' and would explain why (N)TMs without any trigger have a low onset threshold.

Further investigations have been made to disentangle the influence of rotation on the island stability itself as opposed to the trigger mechanism. To this end, the NTM behaviour at the marginal point, where no influence of the trigger mechanism exists, has been analysed. This dependence is shown in figure 4.6. The correlation analysis (table 4.1) reveals that only a very weak dependence of the NTM drive at the marginal point on the normalised rotation velocity exists but additionally this correlation is not significant, which rather implies that no dependence exists than the other way around. From this one can conclude that, so far, no dependence is observed at the marginal point, which could additionally indicate that the rotation dependence at the onset is caused by an impact of rotation on the trigger mechanism. However, the scatter of the data makes it difficult to exclude a dependence on

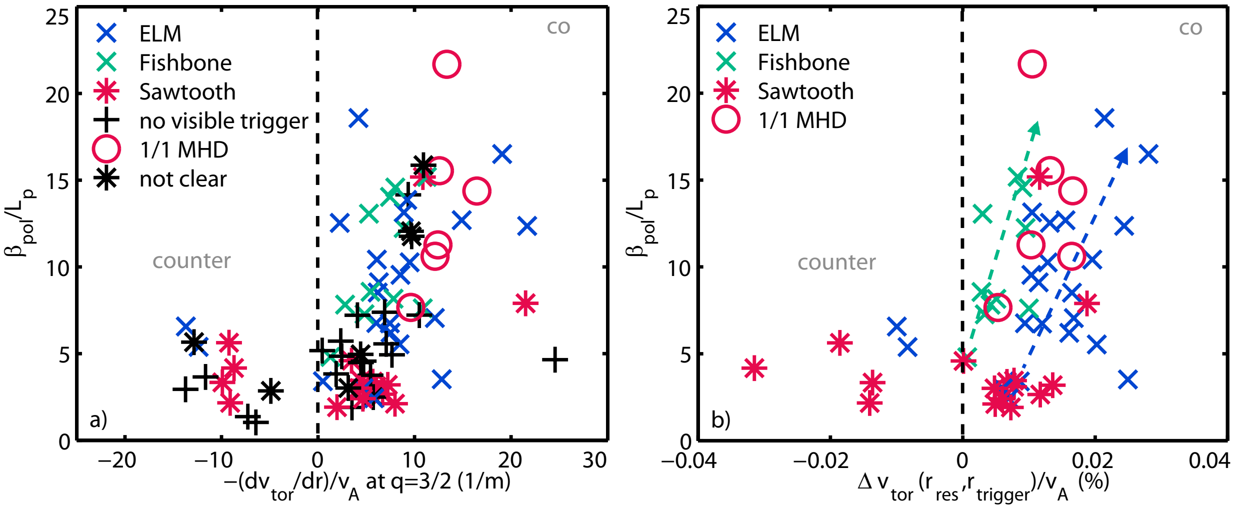

Figure 4.7: (a) (3,2) NTM onset threshold versus the toroidal rotation gradient normalised to the Alfvén velocity at the resonant surface. (b) (3,2) NTM onset threshold versus the differential rotation between the trigger surface (either pedestal top for ELMs or q=1 surface for fishbones, sawtooth or other 1/1 activity) and island surface normalised to the Alfvén velocity. The dashed lines are plotted to guide the eyes.

Δ', which would lead to a dependence at the marginal point and which can still be hidden in dependencies which have not been included in the analysis.

All rotation dependencies have also been analysed using the formulae of Sauter et al. for the bootstrap current drive, defined in equation (3.26), to describe the NTM onset threshold, defining a 'bootstrap drive' as was done in [74] and [44]. With this expression the scatter in the scalings is increased and the quality of the correlation of the whole dataset, especially for co-current rotation, is reduced. This is different compared to results from other machines but can be explained due to a stronger weighting of the density profile for the 'bootstrap drive' which has, at least at AUG, large uncertainties. As discussed above, also differential rotation is a possible candidate to influence the NTM onset threshold, either simply the differential rotation at the resonant surface or the differential rotation between the trigger and the island surface. In figure 4.7 (a) a linear dependence of the NTM onset threshold and the differential rotation (the rotation gradient) at the resonant surface is visible for the whole data set just as for most of the different trigger subsets. Compared to figure 4.4 the scatter of the data is a little bit increased which results in a smaller correlation coefficient (compare table 4.1). At NSTX the correlation of the scaling is improved when using the rotation shear [74] compared to only the rotation gradient. Due to the absence of reliable q profile measurements it is not possible to prove this at AUG.

In figure 4.7 (b) the differential rotation between the island surface and the flux surface where the trigger is located is plotted against the NTM onset threshold. The cases in which ELMs were identified as trigger mechanisms, Δv_{tor} is calculated as the difference of the toroidal rotation velocity at the resonant surface and the toroidal rotation velocity at the pedestal top (around $\rho_{\text{pol}} \simeq 0.95$), whereas the difference of the velocity at the q=1 surface and the resonant surface is used when the trigger mechanism is defined as fishbone, sawtooth crash

Table 4.1: Analysis of the statistical dependence of the NTM onset threshold on the normalised rotation at the NTM onset (figure 4.3 and 4.4) and the marginal point (figure 4.6), the normalised rotation gradient (figure 4.7 (a)) and the differential rotation (figure 4.7 (b)) at the NTM onset. Additionally the correlation parameter for the dependence of the NTM onset threshold on simply the rotation and for the dependence of Ma_A on the onset threshold definition developed by Sauter (equation 3.26) is indicated. The correlation parameter is shown for the whole data set in co- and counter-current direction. For some dependences also the correlation parameters for the different trigger sub-sets are shown. If there are too few data points, or the data range is too small, the correlation is not significant. This is indicated with an x. The abbreviation n.v.t. stands for 'no visible trigger'.

	co	counter	ELM	Fishbone	Sawtooth	n.v.t.	1/1
v_tor vs. β_N	0.47	-0.63	-	-	-	-	-
Ma_A vs. β_N	0.71	x	-	-	-	-	-
Ma_A vs. $\beta_\mathrm{pol}/L_\mathrm{p}$	0.60	-0.68	0.46	0.65	0.56	0.72	x
Ma_A vs. $\delta j_\mathrm{BS,Sauter}$	0.45	x	-	-	-	-	-
Ma_A vs. $\beta_\mathrm{pol}/L_\mathrm{p}$ (marginal)	x (0.13)	-	-	x	-	0.92	-
$(-dv_\mathrm{tor}/dr)/v_\mathrm{A}$ vs. $\beta_\mathrm{pol}/L_\mathrm{p}$	0.50	-0.7	x	0.58	0.56	0.46	x
$\Delta v_\mathrm{tor}(r_\mathrm{res}, r_\mathrm{trigger})/v_\mathrm{A}$ vs. $\beta_\mathrm{pol}/L_\mathrm{p}$	0.26	-	0.47	0.56	x	-	x

or any other mode activity at the q=1 surface. The NTM onset threshold increases with differential rotation for the ELM and fishbone triggered cases whereas no dependence on differential rotation is seen for the sawtooth triggered cases. This means that ELMs and fishbones can more easily lead to a sufficiently large perturbation at the resonant surface when the rotation profile is flat, whereas for sawtooth crashes the rotation profile seems to have no impact on the triggering mechanism. This is an indication that the magnetic reconnection forced by a sawtooth crash at the resonant surface is strong enough to induce a sufficiently large seed island independent of the rotation profile. This is also in line with the observation that NTMs triggered by a sawtooth crash can appear at a low onset threshold.

4.5 Conclusions

In this section, the rotation dependence of (3,2) NTMs at AUG has been analysed. The investigated database includes around 70 discharges with co- and counter-current rotation and different heating mixes. Additionally, the different trigger mechanisms at the NTM onset have been identified. These analyses show an increasing onset threshold with increasing (normalised) co and counter rotation. Compared to investigations at DIII-D where a further decrease of the onset threshold with counter rotation was found, at AUG the region of minimum onset threshold could be reached and the trend with counter rotation clearly verified. As a consequence the onset threshold increases with positive and negative rotation gradient as well. The analysis of the mode frequency indicates that at AUG no offset of the threshold minimum towards negative rotation exists. This is due to a small ion diamagnetic drift frequency which is of the order of the uncertainties of the analyses. It is still possible that at DIII-D the ion diamagnetic drift is larger and an offset exists and the minimum has just not been reached yet. Hence, the results from DIII-D and AUG are not contradictory. Nevertheless, the AUG results show a clear trend and on the bases of these observations, it would be worth to estimate the possible offset at DIII-D and think about a new interpretation of the DIII-D data. At AUG a range of onset β-values is found where the upper limit scales linearly with rotation. This formation of an upper NTM threshold limits the plasma operation below the machine limit. In the region of low rotation the upper threshold no longer depends on rotation which indicates that in this region the NTM behaviour or the triggering process is different. At the marginal point no dependence of the NTM threshold on rotation is found. This leads to the assumption that the trigger mechanism depends on rotation which then leads to a rotation dependence at the NTM onset. On the other hand from the scattered data it is hard to conclude that no influence of rotation on the equilibrium stability index (Δ') exists. It is still possible that this influence is hidden in dependencies that have not been taken into account in the presented analysis. Additionally the observation of NTMs without any trigger appearing at a low NTM threshold and low rotation reveals that the underlying Δ' is less negative (stabilising) at low rotation. Further it was identified that in contrast to the ELM and fishbone triggered cases the triggering of an NTM via a sawtooth crash is independent of the rotation profile and can therefore occur also at low onset threshold. This leads to the assumption that the perturbation at the resonant surface induced by a sawtooth crash is always strong ($W_{\mathrm{seed}} >> W_{\mathrm{crit}}$) or that the trigger mechanism differs from the others.

For ITER, which will be operated at low rotation, the results presented in this section also reveal a low beta limit due to NTMs. The analysis shows that in the range of low rotation the appearance of NTMs is possible even at low β-values. From this point of view it will be crucial to further investigate the NTM parameter dependencies in order to learn how to avoid NTMs best in ITER such that the desired performance can be attained.

Chapter 5

Influence of externally applied magnetic perturbations on neoclassical tearing modes at ASDEX Upgrade

Externally applied magnetic perturbations (MPs) are of great interest for the operation of future fusion devices. They are used for active MHD control, especially for the mitigation of edge instabilities, like the edge localised modes (ELMs) [81, 12, 82]. Additionally, also the active stabilisation of resistive wall modes [83] and NTMs [84] has already been shown. For these reasons magnetic perturbation coils are also planned to be part of the ITER design. However, these actively applied 3D fields have typically also negative side-effects such as density pump out [85, 86, 87, 88] and an increase of fast-ion losses [89, 88]. Additionally, they can act on the plasma stability in an unfavourable way.

The applied resonant MP components can penetrate into the plasma and provoke magnetic reconnection at the corresponding resonant surfaces. This is accompanied by the generation of magnetic islands there. These small islands can act as a seed island for an NTM [81, 90, 91]. Static resonant MPs can hence produce a locked mode, which in most of the cases even leads to a disruption. Also pre-existing rotating modes can interact with the resonant MP components [81, 84]. They can be slowed down and can be locked to the MP field. The non-resonant components of the MP field do not influence MHD modes directly but induce a global braking torque, the neoclassical toroidal viscous (NTV) torque. This also supports the appearance of locked modes [54]. Due to the negative effect of NTMs on the plasma confinement the avoidance, or at least the locking, of NTMs is aimed for. In this regard, the application of MP coils may be accompanied with some problems. Thus, the interaction of an NTM with the MP fields is an important subject, also with regard to ITER.

To study the influence of such externally applied MPs, the B-coils, described in section 2.1.1, are an ideal tool. They generate MP fields with low n mode spectra, mainly $n = 1, 2$ and 4. These spectra are perfectly suitable to study the influence of those MP fields on the (m/n)=(3/2) and (2/1) NTMs, which are the most common and confinement degrading NTMs in AUG.

In this chapter two different discharges are presented in which an influence of the B-coils on NTMs is observed. It is shown that the influence of the B-coils on the mode frequency and

the island width evolution of NTMs can be modelled using a coupled equation system based on the modified Rutherford equation, and the equation of motion, defined in equations (3.64) and (3.65), respectively. Here only the resonant contributions are taken into account. The NTV is neglected in this modelling. To confirm this assumption, the calculation of the NTV torque profile for one discharge is presented accounting for the real perturbation field and plasma geometry. Additionally, the evolution of the entire rotation profile can be calculated including the non-resonant and resonant effects of the MPs.
Experimental observations and the comparison with modelling results show that the resonant effects play the dominant role and the non-resonant contributions of the B-coils, like the NTV [57, 59], seem to be rather negligible under these conditions (relatively high $\nu^* < 1$ compared to ITER). Further it is shown that to fully describe the evolution of one island, all resonant torques at different resonant surfaces have to be taken into account. Parts of this chapter have been already presented in [92] and [93].

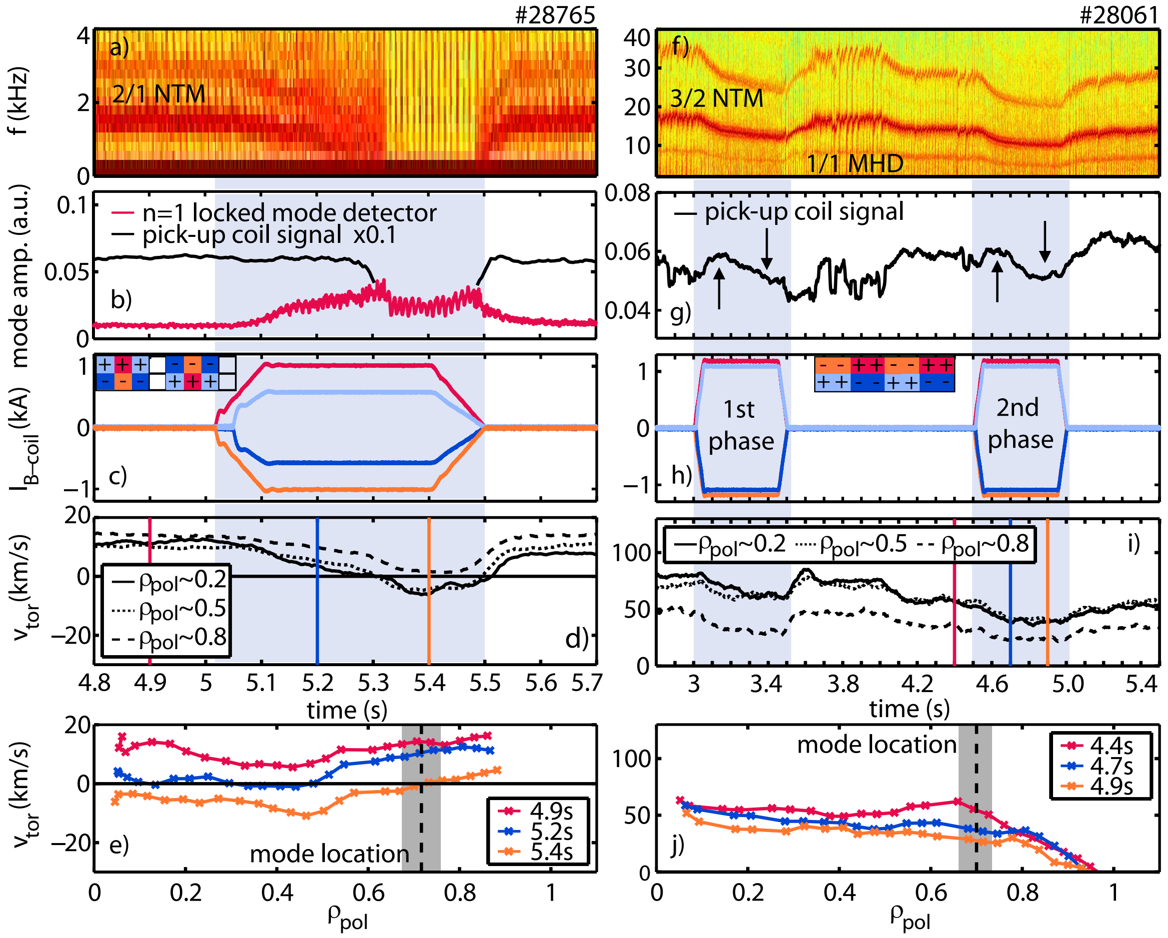

Figure 5.1: Overview of the two discharges which are discussed in this chapter. For each discharge a spectrogram of magnetic data (a) + (f), a qualitative signal for the mode amplitude, from the locked mode detector and/or the pick-up coils (b) + (g) , the current in one winding of the B-coils for four different coils (c) + (h), the time evolution of the toroidal plasma rotation from CXRS (cf. section 2.3.7) at three radii (d) + (i) and profiles of the toroidal plasma rotation at three time points (e) + (j) are shown.

5.1 Experimental observations

At AUG an influence of the MPs on NTMs is observed only in very few discharges so far. Two of them are illustrated in figure 5.1. Each discharge corresponds to one of the two limits where the influence of the MPs on NTMs is predicted to be strongest: low plasma rotation and medium plasma confinement, $\beta_{\mathrm{N}} = 1.35$ or a dedicated plasma shape with low q_{95}, high $\beta_{\mathrm{N}} = 2.1$, low density $n_{\mathrm{e}} = 6 \cdot 10^{19}\,\mathrm{m}^{-3}$ but substantial plasma rotation. In the first case a 2/1 NTM is slowed down and locks to the MP field, shown in figure 5.1 (a)-(e). In the second case a 3/2 NTM is slowed down during two B-coil phases, as illustrated in figure 5.1 (f)-(j).

In both discharges the plasma rotation (panel (d) and (i)) decreases together with the mode frequency (panel (a) and (f)) with a delay of around 50 ms after switching on the B-coils and it increases again with the same delay after ramping down the B-coils. In the locked mode discharge (#28765) the plasma rotation decreases gradually and changes into counter-current direction for $\rho_{\mathrm{pol}} < 0.7$ during the locking phase, whereas at the mode position the toroidal plasma rotation stays zero (panel (e)). In the braking case (#28061) the toroidal rotation profile is almost flat from the mode location towards the core (panel (i) and (j)). In both discharges the plasma rotation decreases over the entire plasma radius.

Analysing the mode amplitudes (panel (b) and (g)) an other small difference of the two cases becomes obvious. Whereas the amplitude of the 2/1 NTM, which is locking, is not changing, neither in the rotating nor in the locking phase, the 3/2 NTM amplitude, in terms of the perturbed radial magnetic field $B_{\mathrm{r}}(t)$, changes slightly correlated with the B-coils. The 3/2 NTM, which is strongly rotating at around 15 kHz, is growing for about 150 ms then the mode amplitude is decreasing again. Despite the decrease of the island's amplitude a confinement reduction during the B-coil phases is observed correlated with a density pump out [87]. In the locking case an enhancement of the higher harmonics, clearly correlated with the B-coils, can be observe, as shown in the spectrogram of one pick-up coil in figure 5.2 (a). This is caused by a distortion of the magnetic signals, which is even visible directly in the

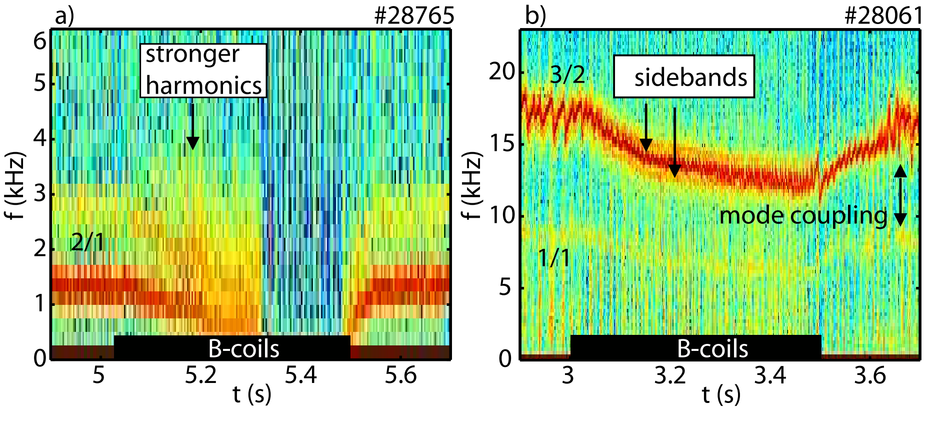

Figure 5.2: Spectrogram of one pick-up coil $\dot{B}_{\mathrm{r}}$ (a) for the locking case and (b) the braking case. In both cases the enhancement of the higher harmonics or the development of sidebands, respectively, can clearly be correlated with the B-coils.

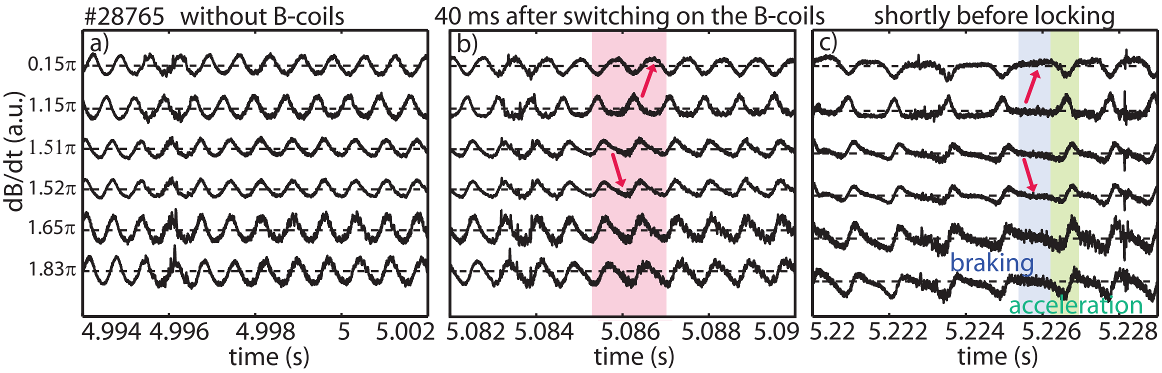

Figure 5.3: Time evolution of magnetic signals ($\dot{B}_\mathrm{r}$) measured with pick-up coils at different toroidal positions for a 2/1 NTM in #28765. (a) The unperturbed signals before switching on the B-coils, (b) slightly perturbed signals 30-40 ms after switching on the B-coils and (c) strongly perturbed signals shortly before mode locking appears, are illustrated. The arrows highlight phases where the increasing distortion is clearly visible.

evolution of the pick-up coil signals, shown in figure 5.3. Without MPs the characteristic signal ($\dot{B}$) of a mode is almost a sinusoid (panel (a)), whereas in the phases with B-coils a distortion is clearly visible, highlighted with the red arrows in panel (b) and (c). Shortly before the mode is locking (panel (c)) regions where the mode is clearly slowed down (blue) and regions where it is accelerated (green) are visible. The distortion however is visible already shortly after switching on the B-coils, in a phase where the mode frequency has not changed significantly. Therefore, an increased influence of the resistive wall torque (compare equation (3.61)) can be excluded, which reveals that the distortion is caused by an impact of the B-coils. The enhancement of the amplitude of the second harmonic can be illustrated by plotting the ratio of the amplitude of the first and second harmonic. This is shown in figure 5.4 (b). These amplitudes are extracted from a pick-up coil signal, corresponding to the frequencies shown in figure 5.4 (a). For the locking case the ratio of second to first harmonic increases strongly during the B-coil phase (figure 5.4 (b)), which corresponds to an increase of the second harmonic. In the braking case (#28061), neither a distortion of the magnetic signal nor an enhancement of the ratio $2^{\mathrm{nd}}/1^{\mathrm{st}}$ harmonic can be observed. In figure 5.4 (d) a small effect might be superposed by strong variations in the island width and hence in the amplitude of the first harmonic. Nevertheless, a clear correlation between the changes in the amplitude ratio and the B-coils is visible. A closer look into the spectrogram of the braking (figure 5.2 (b)) case reveals that in this discharge the 3/2 NTM develops weak sidebands in the first part of the B-coil phase, with its amplitudes decreasing in time. Additionally, the 3/2 NTM couples to the $n = 2$ harmonic of a 1/1 mode (see figure 5.2 (b)). The formation of this coupled mode system is likely to contribute to the strong influence of the B-coils on the mode frequency observed in this discharge even at those high rotation velocities. Additionally, the coupling is consistent with the flat rotation profiles observed in experiment (figure 5.1 (j)).

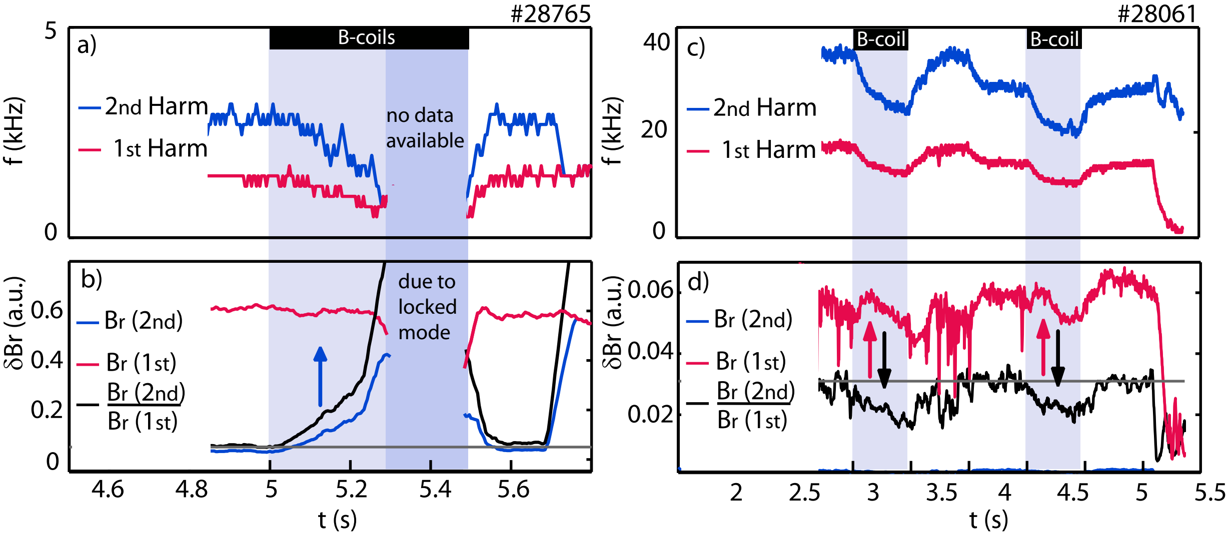

Figure 5.4: Frequency evolution of the 1st and 2nd harmonic during the B-coils phase for (a) the locking and (c) the braking case. In (b) and (d) the amplitude of these two harmonics and their ratio is illustrated. In both cases changes in the ratio of the amplitude of 2nd to 1st harmonic are clearly correlated to the B-coils. For the braking case the amplitude of the second harmonic shown as the blue line in (d) is so small that it is hardly visible.

5.1.1 Interpretation of experimental observation

Most of the experimental observations can be explained by the influence of the resonant MP components on the mode. They lead to a modulation of the island width and frequency, which results in an anharmonic structure of the mode just as detected with the pick-up coils for the locking case. Since the influence of the resonant components decreases with increasing rotation frequency the effect is expected to be weaker in the braking case, where the mode rotation is substantial. However, the development of the sidebands in the braking case due to the B-coils can not be explained. Additionally, the different phasing of the modulation of the island amplitude and phase with respect to the mode rotation, according to equation (3.35) and (3.37) leads on average to a slowing down and a stabilisation of a rotating mode as well as to a destabilisation of a locked mode. This explains the strong decrease of the mode frequency observed in experiments. Nevertheless the predicted influence on the island stability is not so clearly observed in any of the discharges.

Small islands are predicted to rotate naturally with almost the electron perpendicular velocity $v_{\perp,e}$ [94], as described in section 3.5. Two-fluid-theory suggests that resonant perturbations with the same velocity are predicted to have the strongest influence [95]. Hence, for static MPs the impact of the resonant components, mainly in the linear regime, is expected to be strongest for $v_{\perp,e}$ around zero at the corresponding resonant surfaces. In contrast the MP fields are shielded for $v_{\perp,e} \neq 0$. This is exactly what is predicted by the linear theory as illustrated in figure 3.8, assuming $f_{\mathrm{MHD}} \simeq v_{\perp,e}/(2\pi R)$. When f_{MHD} differs from the MP-field frequency the influence of the MPs decreases significantly. A rough estimation of the $v_{\perp,e}$ profile for both discharges is shown in figure 5.5. In the locking case $v_{\perp,e}$ is small over the

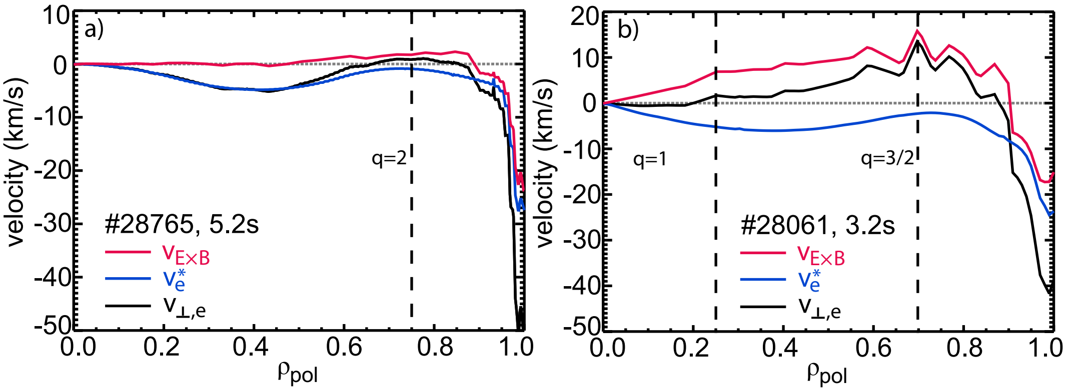

Figure 5.5: Profiles of the electron perpendicular velocity $v_{\perp,\mathrm{e}}$ as a sum of v_{ExB} and v_{e}^* for (a) the locking and (b) the braking case.

entire inner plasma region. In the discharges investigated here $v_{\perp,\mathrm{e}}$ is expected to be high at the edge due to the high gradients of the kinetic profiles there. In the braking case $v_{\perp,\mathrm{e}}$ has a maximum around the NTM position but also in this case, it is small over the entire inner plasma region ($\rho_{\mathrm{pol}} < 0.9$). This reveals that in both cases an influence of the resonant MPs in the linear phase is possible.

Thus, the experimental observations clearly show characteristics attributed to the resonant components of the perturbation field. However the fact that the island's amplitudes are only slightly affected, suggests that additional torques are acting, which do not influence the island stability at the resonant surface, but slow down the island rotation, like the NTV torque or resonant torques at other surfaces would do. This is in line with the presence of a small $v_{\perp,\mathrm{e}}$ which suggests that the influence of further resonant components in the linear phase is possible.

5.2 Basic model

The impact of the MP fields on the evolution of an NTM can be described by including the corresponding effects into the modified Rutherford equation (MRE) (eq. 3.64) and the equation of motion (EOM) (eq. 3.65).

The **resonant** components of the MP field lead, according to the non-linear theory described in section 3.4, to a modulation of the frequency and width of a rotating mode. This modulation of the island width and frequency is phase shifted, which on average, leads to a slowing down and a stabilisation of a rotating mode as well as to a destabilisation of a locked mode. So the resonant components directly influence the island stability and additionally induce a local torque at the resonant surfaces. The impact on the island stability is described by equation (3.35). The influence on the island frequency via the resonant ($\vec{j} \times \vec{B}$) torque is described by equation (3.37). In both equations the influence of the resonant MP field components is parametrised by the width of the vacuum island W_{vac}. The vacuum plots (superposition of the equilibrium and the perturbation field) for the locking and the braking case are shown in figure 5.6. The vacuum islands due to the applied n=1 and n=2 error

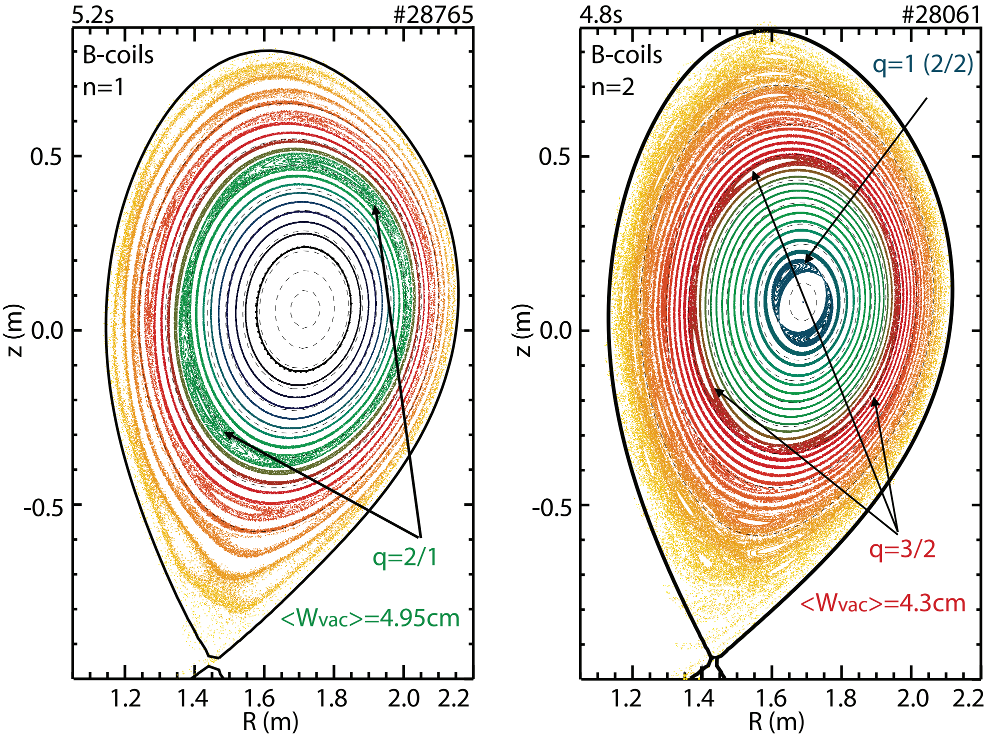

Figure 5.6: Poincaré plot of the vacuum magnetic field in the poloidal plane for (a) the locking case (B_{tor} = 2.5 T, I_{p} = 0.8 MA, $I_{\mathrm{B-coils}}$ = 5215 A, q_{95} ≈5.2) and (b) the braking case (B_{tor} = 1.73 T, I_{p} = 0.8 MA, $I_{\mathrm{B-coils}}$ = 5750 A, q_{95} ≈3.8). The B-coils have been used with an n=1 and n=2 configuration which leads to pronounced vacuum islands at the q=2/1 and the q=3/2 surface respectively. Also further vacuum islands at other surfaces are present as well.

fields are clearly visible. In the locking case (#28765) especially the formation of a 2/1 mode at the q=2/1 is observed. In the braking case both a 3/2 and large 2/2 mode at the q=3/2 and q=1 surface, respectively, are formed. In addition, in both discharges the formation of a variety of other islands is observed. The theory, described in section 3.4.1, is developed for cylindrical plasmas. Therefore, the quantities taken from the experiment with toroidal geometry have to be adjusted. The induced vacuum island width for example is not constant on a flux surface, clearly visible in figure 5.6. Hence, the flux surface averaged vacuum island width is used in the following calculation, corresponding to a flux surface averaged resonant component of the perturbation field at the resonant surface in real AUG geometry.

The **non-resonant** components of the externally applied MP fields do not influence the mode amplitude directly but they can affect the plasma rotation and hence the mode frequency via the NTV torque. The NTV torque has already been introduced in section 3.4.2 and can be described by equation (3.50), in a general form. This NTV torque can be included in the EOM. In order to estimate the influence of the NTV on the plasma rotation and concomitant also on the mode frequency the NTV has been calculated for the locking and braking cases. This calculation by means of the braking case is presented in detail in the following section 5.3.

In section 5.4 a simplified approach for the MRE is used, which includes an approximation for the Δ' term, an approximation for Δ_{BS}, the destabilising contribution of the bootstrap current (bs) defect, and the influence of the resonant MP components.

$$0.82\frac{\tau_R}{r_{\text{res}}}\frac{dW}{dt} = \Delta' r_{\text{res}} + \Delta_{\text{bs}} r_{\text{res}} + \Delta_{\text{ext}} r_{\text{res}} \tag{5.1}$$

$$\Delta' = -m/r_{\text{res}} \tag{5.2}$$

$$\Delta_{\text{bs}} = \frac{c_{\text{bs}}}{W} \tag{5.3}$$

The fit parameter c_{bs} is adjusted to fulfil $dW/dt = 0$ before switching on the B-coils with $\Delta_{\text{ext}} = 0$, in a phase where the island width is constant. The influence of the stabilising effect of the wall [37], introduced in equation (3.62) has also been investigated. This effect is small for the investigated discharges and has therefore not been taken into account in the analysis of the island growth in the following section. In section 5.4 the EOM is evaluated locally, at the position of a mode, hence ω corresponds to the mode frequency. This delivers the local mode frequency evolution and thus, all torques have to be evaluated at the resonant surface. In a local evaluation only the deviation of the mode frequency from its natural frequency is important. Hence, the viscous torque can be described by equation (3.57). In this approach the NBI input torque is already included and thus, it is not taken into account explicitly. The NTV torque is small compared to the resonant contribution and thus, it can be neglected in the modelling of the island rotation. This is motivated in more detail in section 5.3 and section 5.5.

In section 5.5 the evolution of the entire rotation profile is modelled, accounting for the radial dependence of all torques and a constant momentum diffusion coefficient D_ϕ. In this analysis also the influence of the NTV torque on the rotation profile is modelled.

5.3 Neoclassical toroidal viscosity

The non-resonant components of the external MP field can affect the plasma rotation via the neoclassical toroidal viscous torque (NTV), as already discussed in section 3.4. This NTV contributes to the plasma rotation damping via a non-ambipolar radial flux of trapped particles Γ_i induced by the error field:

$$-t_{\text{NTV}} = Ze\Gamma_i \tag{5.4}$$

The derivation of the NTV torque is quite complicated. It can not be expressed in a formula, which can be handled as simple as the one for the resonant contributions. Therefore, in the following section the calculation of the NTV profile for the braking case is discussed in detail. In [57] an expression for the NTV for cylindrical plasmas with helical perturbation fields in low collisionality plasmas (banana regime) is developed. Though, the B-coils, which are located only at the low field side, produce an MP field which is strongest at the edge in front of the coils. Hence, the B-coils produce an MP field which is not at all helical, as shown in figure 5.7. Additionally, the plasmas in ASDEX Upgrade are not cylindrical. Since the effect of the assumptions used in [57] can not be estimated, the formulae derived in [57] can not be used.

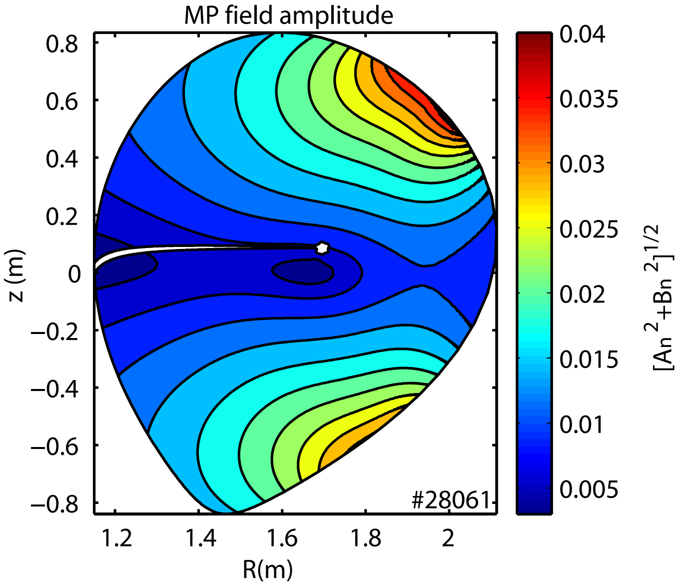

Figure 5.7: Total magnetic perturbation field amplitude in a poloidal cross section, which is strongest at the low field side in front of the B-coils.

In the following section a calculation of the NTV is presented, which is based on [57], [58] and [59], however, taking into account, the real perturbation field and plasma geometry. This is not done in most of the calculation at other experiments, where simply a helical perturbation and a cylindrical plasma is assumed. The following calculation is presented for a discharge with an $n = 2$ perturbation due to a 'non-resonant' B-coil configuration.

5.3.1 Perturbed magnetic field

First of all a decomposition of the perturbed magnetic field has to be found, which is compatible with the expression introduced in [58] and the straight-field-line coordinates used therein. The magnetic field in the presence of a perturbation field can be expressed by the perturbation field components (δB_{tor}, δB_{pol}, δB_r) and $B_0 = \sqrt{B_{\mathrm{tor}}^2 + B_{\mathrm{pol}}^2}$, the equilibrium magnetic field, in a torus coordinate system (ϕ,θ,r) (figure 1.3 (a))

$$\begin{aligned} B &= B_0 + \delta B \\ &= \sqrt{(B_{\mathrm{tor}} + \delta B_{\mathrm{tor}})^2 + (B_{\mathrm{pol}} + \delta B_{\mathrm{pol}})^2 + (\delta B_{\mathrm{r}})^2} \qquad (5.5) \\ &= B_0 \cdot \sqrt{1 + \frac{2B_{\mathrm{tor}}\delta B_{\mathrm{tor}}}{B_0^2} + \frac{2B_{\mathrm{pol}}\delta B_{\mathrm{pol}}}{B_0^2} + \frac{\delta B_{\mathrm{tor}}^2 + \delta B_{\mathrm{pol}}^2 + \delta B_{\mathrm{r}}^2}{B_0^2}}. \end{aligned}$$

This expression can be Taylor expanded via $\sqrt{1+x} \approx 1 + x/2$. Taking into account only the first order components yields:

$$\delta B = B_0 \cdot \left(\frac{B_{\mathrm{tor}}\delta B_{\mathrm{tor}}}{B_0^2} + \frac{B_{\mathrm{pol}}\delta B_{\mathrm{pol}}}{B_0^2} \right) \qquad (5.6)$$

The experimental perturbation field can be Fourier decomposed in toroidal direction for the main toroidal mode number(s), which delivers the covariant components of the perturbation

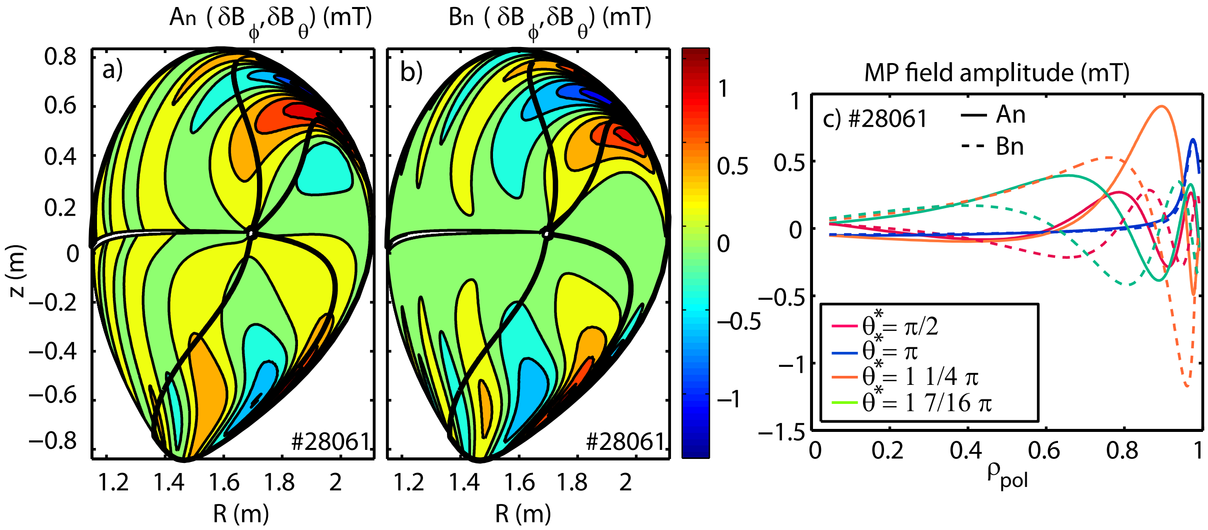

Figure 5.8: (a) Real (A_n) and (b) imaginary (B_n) perturbation field amplitudes, according to equation 5.13 in a poloidal cross section according to the decomposition of the perturbations field shown in equation (5.13). (c) Radial profiles of the real (A_n) and imaginary (B_n) perturbation field amplitudes for the constant θ^* values indicated in (a) and (b) by the black lines.

field. This yields the following expression for the toroidal, the normal($\hat{=}$radial) and the tangential ($\hat{=}$ poloidal) component of the perturbation field

$$\delta B_i = R_i \cos(n\phi) + I_i \sin(n\phi), \tag{5.7}$$

with R_{i} the real part and I_{i} the imaginary part of the perturbation amplitude and i indicating the different components. To follow the calculations in [58], adjustments to expressions and the coordinate system used in [58] have to be made. In [58] a straight-field-line coordinate system (Ψ, θ, β) is used with $\beta = q(r)\theta - \phi$ and $J = -1/\vec{B} \cdot \vec{\nabla}\theta$ the corresponding Jacobian. The according Fourier decomposition of the experimental perturbation field is:

$$\delta B_i = R_i(r,\theta)\cos(q(r)n\theta - n\beta) + I_i(r,\theta)\sin(q(r)n\theta - n\beta) \tag{5.8}$$

A new ordering of this expression results in the formulae below with the new argument ($n\beta$)

$$\begin{aligned} \delta B_i &= a_i \cos(n\beta) + b_i \sin(n\beta) && (5.9)\\ a_i &= R_i \cos(q(r)n\theta) + I_i \sin(q(r)n\theta) && (5.10)\\ b_i &= R_i \sin(q(r)n\theta) - I_i \cos(q(r)n\theta). && (5.11) \end{aligned}$$

In [58] the magnetic field in the presence of the MP field is decomposed in the following way:

$$B = B_0(\theta) - B_0 \sum_n D_n(\theta,\beta) \tag{5.12}$$

$$D_n(\theta,\beta) = A_n(\theta)\cos(n\beta) + B_n(\theta)\sin(n\beta) \tag{5.13}$$

with n the toroidal mode number. For the later calculations, and since the decomposition is only done in toroidal direction, equation (5.5), (5.6) and (5.9) have to be combined and conformed to find the corresponding expression for the coefficients A_n and B_n, which are needed in the later calculation.

$$D_n = \sum_i -\delta B_i/B_0 \tag{5.14}$$

$$\Downarrow$$

$$A_n(\theta) \hat{=} -\frac{B_{\mathrm{tor}}}{B_0^2}a_\phi - \frac{B_{\mathrm{pol}}}{B_0^2}a_\theta \tag{5.15}$$

$$B_n(\theta) \hat{=} -\frac{B_{\mathrm{tor}}}{B_0^2}b_\phi - \frac{B_{\mathrm{pol}}}{B_0^2}b_\theta \tag{5.16}$$

with $A_n(\theta)$ and $B_n(\theta)$ the real and imaginary perturbation field amplitudes. The perturbation field amplitudes in the poloidal plane for the decomposition introduced in equation (5.13) are illustrated in figure 5.8 (a) and (b), accounting for the poloidal and toroidal perturbation field components. Figure 5.8 (c) shows four radial profiles of the perturbation field amplitudes for constant θ^* taken at four different angles, which are indicated by black lines in figure 5.8 (a) and (b). The perturbation field amplitudes are in the order of 0.1 mT and are peaked towards the edge.

5.3.2 Estimation of the particle flux

According to equation (5.4) the NTV torque can be calculated from the radial non-ambipolar particle flux Γ in the relevant collisionality regime. In the core region the investigated plasmas are mainly in the low collisional banana regime ($\nu_{\mathrm{ii}}/\epsilon < \omega_{\mathrm{b}}$). Within this regime they are in-between the $1/\nu$ and ν regime. For the following estimation the formulae and parameter dependences valid for the $1/\nu$ banana regime are used for the entire plasma. At higher collisionality, for example towards the edge or at higher densities, the flux of trapped particles is reduced and concomitant also the NTV torque. Hence, the NTV torque calculated in the following represents an upper limit.

The radial particle flux in the $1/\nu$ regime can be determined solving the bounce averaged drift-kinetic equation and taking the velocity momentum of the distribution function.

Using the Ansatz as calculated in [58] the flux can be described as a product

$$Ze\Gamma_{\mathrm{i}} = n_i m_i \mu_{||} I_\lambda \left(\langle R^2 \vec{v}_{\mathrm{i}} \vec{e}_\phi \rangle - \langle R^2 \Omega^*_{\mathrm{NC}} \rangle \right), \tag{5.17}$$

of the ion mass m_i and density n_i, the toroidal viscosity frequency $\mu_{||}$, the pitch angle integral I_λ and the difference of the rotation velocity of the ion fluid $\vec{v}_{\mathrm{i}}\vec{e}_\phi$ and a neoclassical offset frequency Ω^*_{NC}.

The profiles of the four different contributions are shown in figure 5.9.

Toroidal viscosity frequency $\mu_{||}$

The toroidal viscosity frequency $\mu_{||}$ [59, 96], is also known as the NTV damping frequency. It depends on the ion transit frequency ω_{ti}, hence, on the thermal ion velocity $v_{\mathrm{th,i}}$ and the

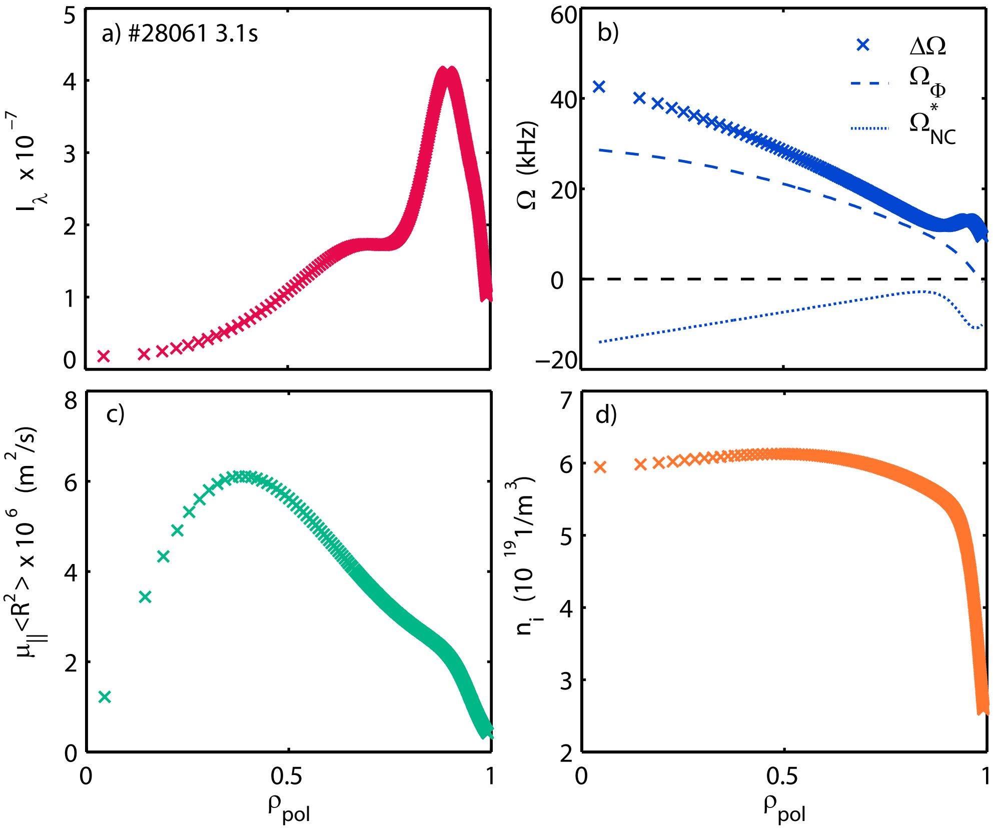

Figure 5.9: Profiles which contribute to the particle flux: (a) pitch angle integral (b) difference of toroidal and offset frequency, (c) toroidal viscosity frequency and (d) density.

ion-ion collision frequency ν_{ii} [5], which are defined below and illustrated in figure 5.10

$$\mu_{||} = 0.84\epsilon^{3/2}q^2\omega_{\text{ti}}^2/\nu_{\text{ii}} \tag{5.18}$$

$$\omega_{\text{ti}} \simeq v_{\text{th,i}}/(\langle R\rangle q) \tag{5.19}$$

$$v_{\text{th,i}} = \sqrt{2T_{\text{i}}/m_{\text{i}}} \tag{5.20}$$

The resulting toroidal viscosity frequency profile (figure 5.9 (c)) is hollow towards the core. This is caused by the dependence on the fraction of trapped particles, which is proportional to $\sqrt{\epsilon}$, so it is zero in the core and increases towards the edge.

Pitch angle integral I_λ

The parameter I_λ (figure 5.9 (a)) is the integral over the perturbed magnetic field harmonics

$$I_\lambda = \frac{16\pi^2}{A}\int_0^1 d\kappa^2[\hat{J}(\kappa)]^{-1}\sum_n n^2[\tilde{a}_n^2 + \tilde{b}_n^2] \tag{5.21}$$

$$A = \int_0^{2\pi}\int_0^{2\pi} -Jd\theta d\beta \cong 2\pi\int_0^{2\pi} -Jd\theta \tag{5.22}$$

$$\hat{J}(\kappa) = \oint -Jd\theta\sqrt{\kappa^2 - \sin^2(\theta/2)} \tag{5.23}$$

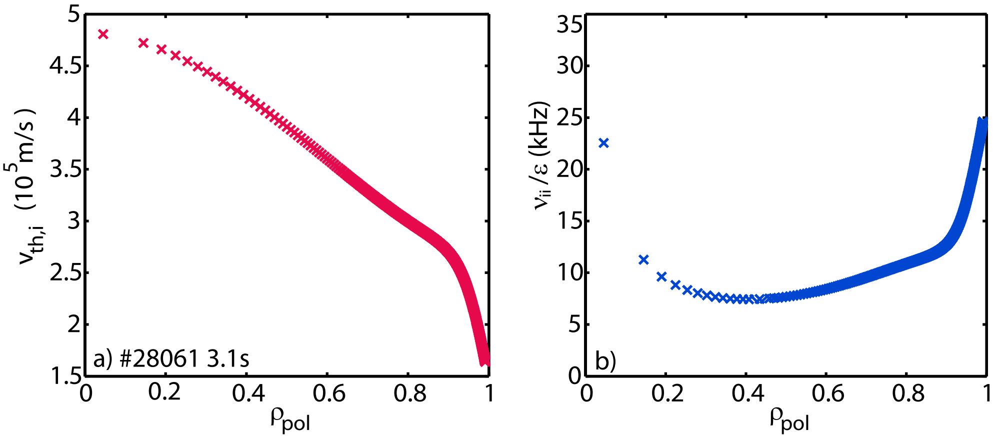

Figure 5.10: (a) Thermal velocity profile and (b) ion-ion collision frequency profile which contribute to the calculation of the toroidal viscosity frequency profile.

with κ the normalised pitch angle parameter. The coefficients $\tilde{a}_{\mathrm{n}}$ and $\tilde{b}_{\mathrm{n}}$ are bounce integral coefficients over the harmonic coefficients A_{n} and B_{n}. Hence, I_λ includes the perturbation field amplitudes as introduced in equation (5.15) and (5.16) and the information of the redistribution of trapped particles due to the magnetic field distortion. The integration over the closed line integral $\oint d\theta = \oint_{-\theta_b}^{\theta_b} d\theta$ is taken between symmetric bounce points $\theta_b = 2\arcsin(\kappa)$ [57] which depends on κ. The parameter κ^2 is within [0, 1], which represents the velocity space of trapped particles. The bounce integral coefficients are defined in the following way:

$$\tilde{a}_n = \oint -J d\theta \sqrt{\kappa^2 - \sin^2(\theta/2)} A_n(\theta) \tag{5.24}$$

$$\tilde{b}_n = \oint -J d\theta \sqrt{\kappa^2 - \sin^2(\theta/2)} B_n(\theta) \tag{5.25}$$

The different components which contribute to the pitch angle integral are shown in figure 5.11 for κ values from 0 to 1.

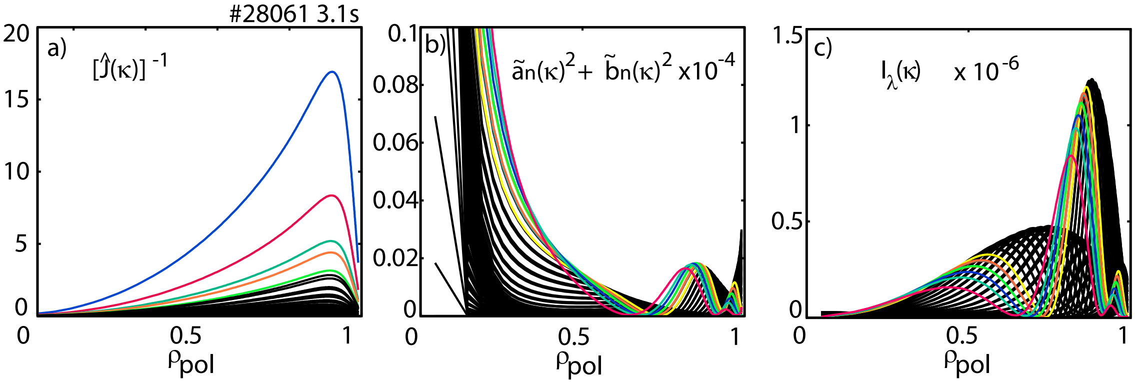

Figure 5.11: In (a) and (b) the two important contribution to the pitch angle integral for different κ values are illustrated. The resulting I_λ for different κ values is shown in (c). κ is within [0, 1]

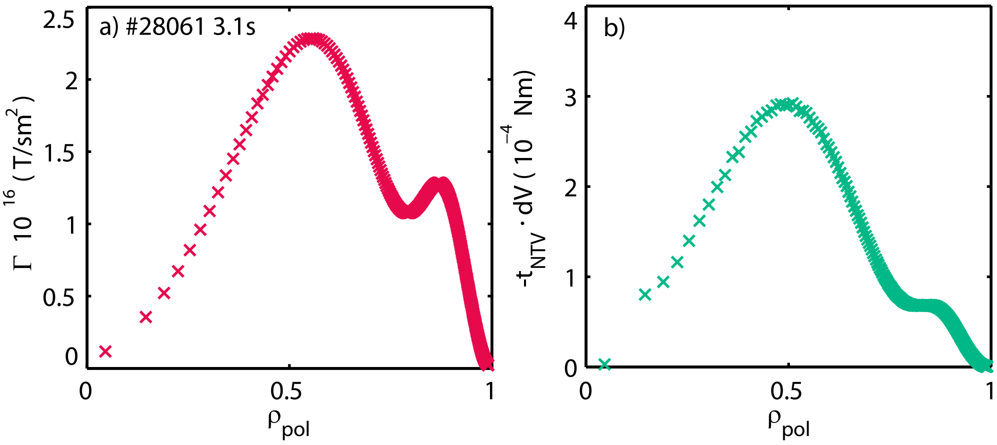

Figure 5.12: (a) Non-ambipolar flux profile and (b) resulting NTV torque profile.

Neoclassical offset frequency $\langle \Omega^*_{NC} \rangle$

An important contribution is the difference of the toroidal plasma rotation frequency and a neoclassical offset frequency. The NTV torque can be seen as driven by this rotation difference. For the calculation it is assumed that the toroidal rotation frequency $\langle \Omega_t \rangle \equiv \vec{v_{\mathrm{i}}}\vec{e}_\phi$ is constant on a flux surface, hence it is taken from the CXRS measurements at the low field side. The neoclassical offset frequency, which was so far only observed experimentally [61, 62, 97, 98], is of the order of the ion diamagnetic drift frequency and can be approximated according to [59]

$$\langle \Omega^*_{\mathrm{NC}} \rangle \approx \frac{c_p + c_t}{eZ} \frac{dT_{\mathrm{i}}}{d\psi} \tag{5.26}$$

The coefficient c_t and c_p are around 2.4 and 1 respectively [59], in the relevant low collisionality regime. In figure 5.9 $\langle \Omega^*_{NC} \rangle$ is shown which is always in counter-current direction for a static perturbation. $\langle \Omega^*_{NC} \rangle$ is mainly determined by $dT_{\mathrm{i}}/d\psi$. In the calculation the derivative with respect to ψ can be substituted with $d\rho_{\mathrm{pol}}(d\psi/d\rho_{\mathrm{pol}})$ using equation (1.8).

NTV torque profile

Assuming that the toroidal rotation frequency and also the neoclassical offset frequency are constant on a flux surface, the value for $\langle R^2 \rangle$ can be extracted from $\langle R^2 \Omega_\phi \rangle = \langle R^2 \rangle \langle \Omega_t \rangle$ and reduced with the one in $\mu_{||}$ (cf. equation (5.18)), which further simplifies the calculation.

$$Ze\Gamma_{\mathrm{i}} = n_i m_i \mu_{1/||} I_\lambda \langle R^2 \rangle \left(\langle \Omega_\phi \rangle - \langle \Omega^*_{\mathrm{NC}} \rangle \right) \tag{5.27}$$

The torque density t_{NTV} is hence given by $(-Ze\Gamma_{\mathrm{i}})$ and the total torque T_{NTV} via $\int t_{\mathrm{NTV}} dV$. A total torque profile $T_{\mathrm{NTV}}(r)$, which is needed for the calculation of the change in rotation due to the NTV, is obtained by multiplying t_{NTV} with the Volume of a small plasma shell defined by the distance of the radial grid. The resulting flux profile and the NTV torque profile are illustrated in figure 5.12. Both profiles are peaked centrally with only a small hump near the edge. In fact one would expect to get a profile which is peaked at the edge, because of the biggest influence of the MPs there, like the I_λ profile. However, the radial dependence of the other contributions (figure 5.9) leads to a reduction of the NTV at the edge and leads to a maximum at mid radius.

5.3.3 Interpretation

The total calculated NTV torque is around 0.023 Nm, which is around 100 times smaller, than the input torque of one NBI beam. This revels that at least in this discharge the NTV appears to be rather negligible. Nevertheless the question arises if the calculated NTV torque is of the right order of magnitude. The theory predicts a strong dependence of the NTV on the ion temperature $T_\mathrm{i}^{7/2}$. This can be reproduced in the calculation. In the calculation a factor of two higher T_i leads to an increase of the total T_NTV by a factor of 10. From this point of view the parameter dependence is implemented correctly. Unfortunately no other calculation exists to compare the results with. However, aslo the comparison with other experiments gives no information on the correctness: at DIII-D [62, 61], JET [99] and NSTX [97] it is observed that the NTV has a significant influence, which can be partly reproduced by the models. However, for example at TEXTOR [99] the calculated and observed NTV is very small.

At least also in the experiments at AUG no indication for a big impact of the NTV is observed. In general in the experiment it is difficult to disentangle resonant and non-resonant effects, if the rotation is affected. However if one assumes that the resonant effects are minimised in a 'non-resonant' configuration, the impact of the non-resonant components should be dominant. And if further, in a discharge with a 'non-resonant' MP configuration the rotation is not affected, it can be concluded that the NTV is small.

Hence, the evolution of the rotation profile of such a discharge is presented in figure 5.13 as a contour plot. The kinetic profiles (n_e, T_e and T_i) of this discharge are similar to the braking case but the plasma rotation and the toroidal magnetic field ($B_\mathrm{tor} = 2.5\,T$) are higher. Additionally the B-coil configuration is slightly different. The calculated total NTV torque is around 0.0031 Nm, which is even smaller than in the braking case. In this discharge the B-coils are switched on 4 times in an n=2 configuration but with different phasing of the upper and lower row. This results in two phases with a 'resonant' and two with a 'non-resonant' configuration, where ELM mitigation occurs during the 'non-resonant' B-coil phases. In this discharge only a 3/2 NTM is present, but the mode frequency and amplitude are not affected, hence the resonant components seem to be shielded. This is in agreement with the high plasma rotation. Accordingly, in the contour plot also no impact on the rotation in the phases with a 'resonant' B-coil configuration is observed. However, also in the phases with a non-resonant configuration the rotation is not affected. If the NTV would be significant at least in these phases an influence should be visible. This reveals that also in experiment the NTV is small, which is in good agreement with the predicted small torque resulting from the calculation, which validates the calculation.

The calculated total NTV torque for the locking case is around 0.0002 Nm. This is around

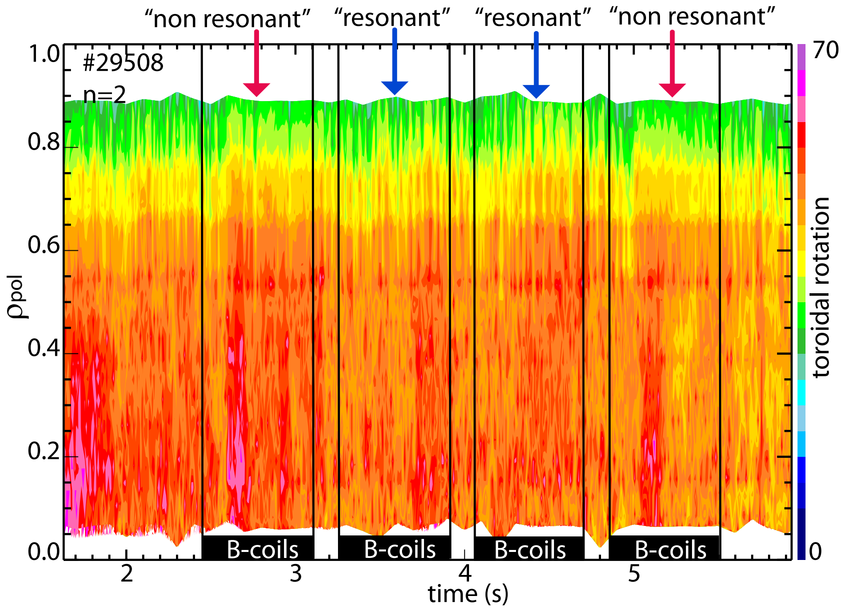

Figure 5.13: Contour plot of the toroidal plasma rotation of a discharge with four B-coils, two in a resonant and two in a non-resonant configuration.

two orders of magnitude smaller compared to the braking case, but can be explained by the very low plasma rotation (figure 5.1 (e)), which reduces the drive of the NTV, and a significantly smaller perturbation field amplitude. In summary, the calculation of the NTV torque can be confirmed with experimental observations. It seems to depend strongly on the MP field configuration. The calculated NTV is small for the braking case and even smaller for the locking case. Hence, it can be neglected in both cases. This is additionally confirmed for the braking case by modelling the influence of the NTV torque on the entire rotation profile presented in section 5.5.

5.4 Modelling of the island stability and rotation

The interaction of a saturated, rotating magnetic island with the externally applied MPs can be calculated, solving the coupled equation system for the mode amplitude and phase, defined in equation (5.1) and (3.65), simultaneously [37]. The initial island width W_0 is taken from the flattening of the T_e profile measured at the low field side (LFS) of AUG (compare figure 1.5). The width of the vacuum island W_{vac} is determined from the vacuum approximation (fig. 5.6). An averaged vacuum island width on a flux surface is used, to take into account the elongated plasma shape and differences of the high and low field side in the cylindric approach. The equilibrium reconstruction (section 2.3.1) provides q profiles, which are consistent with the experimental determination of the location of the resonant surface r_{res}. All input parameters for the calculations are summarised in table 5.1. The coefficient A in equation (3.57) is adjusted in a way, that after switching off the B-coils the mode spins up to its natural frequency ω_0 consistent with the timescale observed in the experiment. This parameter A in the presence of an island is of the order of 10^{-5} kg m^2/s for

Table 5.1: Modelling parameters.

	r_{res} (m)	q	q' (1/m)	B_{tor} (T)	C (T/m)	W_0 (m)	W_{vac} (m)
#28061 braking	0.27	3/2	3.62	1.73	0.038	0.05	0.043
#28765 locking	0.29	2/1	7.44	2.5	0.0486	0.06	0.049

the investigated discharges. Another way to determine the parameter A is to assume, that the plasma rotation measured in the experiment is only caused by the applied NBI input torque. This method can only be applied when no mode is present due to the unknown torque the presence of the mode would cause. Knowing the rotation profile and the local input torque via $T_{\text{NBI}} = -A/n\langle\Omega_\phi\rangle$ the parameter A can be determined. The estimated total NBI input torque is around 1-2 Nm per beam, depending on the injection angle. One example NBI input torque profile for the braking case (#28061) is shown in blue in figure 5.19 (c) together with the corresponding unperturbed rotation profile in figure 5.19 (a) in blue. According to these profiles this method delivers a parameter A of around $0.5 \cdot 10^{-5}$ kg m^2/s which is in good agreement with the values of the first method listed in table 5.1. The corresponding momentum diffusion coefficient D_ϕ calculated in section 5.5 is around 0.4 m/s^2.

Solving the EOM and the MRE including the effect of only the resonant MPs leads to a slowing down of the island, which is far too small in both investigated cases.
To match the frequency evolution of the modes in experiment two fit parameters, c_{vac} and c_{ext}, had to be introduced in equation (5.1) and (3.65). The vacuum island width is multiplied by the parameter c_{vac} to adjust the influence of the B-coils in the EOM and the MRE. This is equal to introducing an effective vacuum island width $W_{\text{effective}} = W_{\text{vac}} \cdot c_{\text{vac}}$. By adjusting c_{vac} in the calculation a shielding or an amplification of the perturbation field compared with the vacuum case can be included. The second parameter c_{ext} is used to diminish the modulation of the islands amplitude directly and hence, the resulting effect on the island width via a multiplication of Δ_{ext} with c_{ext}. This results in the following equations, according to equation (3.35) and (3.37):

$$\Delta_{\text{ext}} = \frac{2m}{r_{\text{res}}}\left(\frac{c_{\text{vac}}W_{\text{vac}}}{W}\right)^2 \cos(\Delta\phi) \tag{5.28}$$

$$T_{\phi,\text{jxB}} = -4\pi^2 c_{\text{ext}}\frac{mn}{\mu_0}\; C^2\; (c_{\text{vac}}W_{\text{vac}})^2\; W^2\; \sin(\Delta\phi) \tag{5.29}$$

All adjusted fit parameters are summarised in table 5.2. Additionally in the calculation, the B-coils are switched on immediately and are not ramped up as in the experiment. To correct this and the corresponding delay of the response of the mode during the ramp up

Table 5.2: Fit parameters.

	A (kg m^2/s)	c_{vac}	c_{ext}
#28061 braking (1$^{\text{st}}$/2$^{\text{nd}}$ phase)	$0.5 \cdot 10^{-5}$ / $0.9 \cdot 10^{-5}$	4.06 / 4.0	1 / 1
#28765 locking	$1.1 \cdot 10^{-5}$	2.2	0.65

of the B-coils, the B-coils in the modelling are switched on 0.05 s later with respect to the experiment.

5.4.1 Mode locking

The modelling results for the island width and the rotation frequency for the locking case (#28765) and the comparison to the experimental values are shown in figure 5.14. The experimental mode frequency and island width evolution are determined from magnetic coil signals. The experimental island width resulting from magnetic measurements are not absolutely calibrated, therefore the evolution is scaled to match the unperturbed island width W_0 before switching on the B-coils.

The best agreement of experiment and calculation for the frequency evolution is achieved by increasing the vacuum island size by a factor of 2.2. This enhancement additionally leads to a stabilisation of the island before it is locking. Since this is not observed in experiment the influence of the B-coils on the island width evolution had to be decreased directly by a factor (c_{ext}) of 0.65.

Despite the adjustments described above the island is still strongly stabilised in the calculation while it is rotating. During the locking the island grows strongly which is also not in agreement with the experiment. Additionally, in the calculation the actual locking of the mode can only be reproduced by including the resistive wall term. By definition, compare equation (3.61), $T_{\phi,\text{rw}}$ depends on W^4, hence it will grow rapidly during the locking phase using the calculated island width W and the restoring viscous torque will not be able to unlock the island after switching off the B-coils. Since unlocking is observed in experiment and also the island width is not increasing, in the calculation the dependence on W is replaced by $T_{\phi,\text{rw}}(W_0)$, in order to adjust the modelling to the experimental observations.

In addition, the mode is locking earlier in the modelling than in experiment. All these assumptions, which have to be made in order to describe the measurements, reveal that the

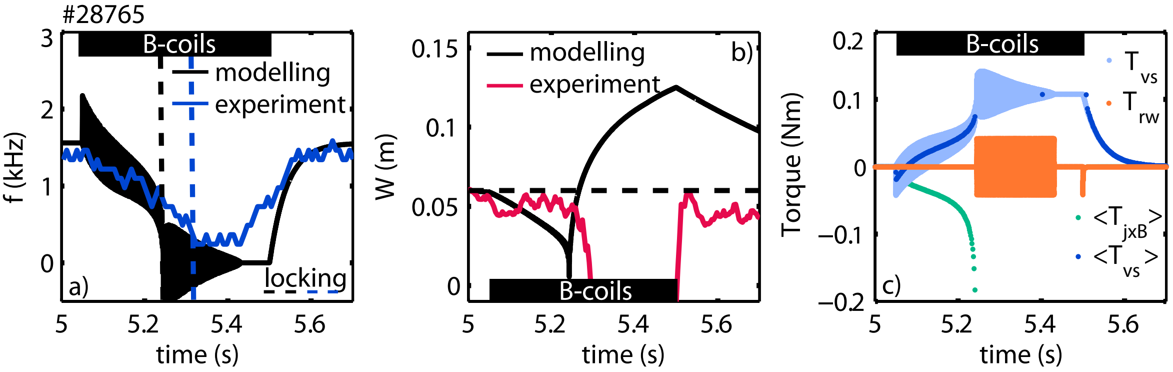

Figure 5.14: (a) Calculated mode frequency and (b) island width resulting from the modelling where the discussed assumptions are included. Each evolution is compared to the experimental quantities. No experimental data for the island width are available during mode locking. (c) Time evolution of the acting torques, where the viscous and the $(\vec{j} \times \vec{B})$ torque are averaged over 2π are shown. The vertical dashed lines in (a) indicate the locking time in the calculation (black) and in the experiment (blue).

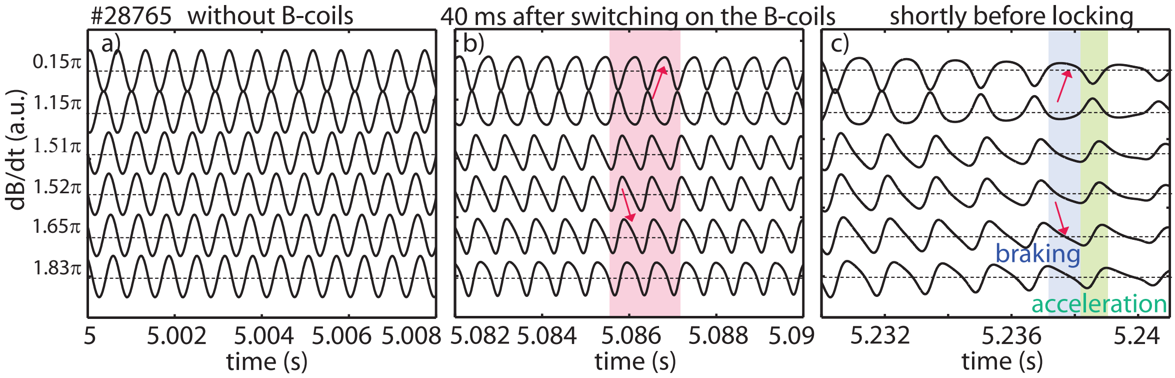

Figure 5.15: Simulated ballooning coil signals at different toroidal positions for the locking case. The unperturbed signals (a) before switching on the B-coils, (b) slightly perturbed signals 30-40 ms after switching on the B-coils and (c) strongly perturbed signals shortly before mode locking appears are illustrated.

effect on the island width is overestimated or that further effects are not included. Another solution would be that additional torques exist which slow down the island but do not influence the island amplitude. However, the modulation of the mode amplitude and phase due to the resonant MP components is clearly reproduced in the modelling. The synthetic pick-up coil signals show a clear distortion (figure 5.15) comparable to the experiment. Also the resulting enhancement of the higher harmonics in the spectrogram during the B-coil phase is reproduced, as shown in figure 5.16 (a).

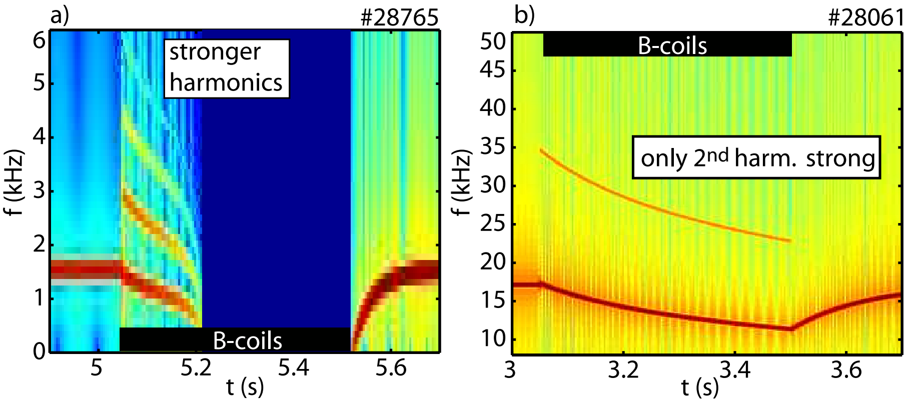

Figure 5.16: Spectrogram calculated from one single simulated magnetic pick-up coil signal, as shown in figure 5.15 for (a) the locking (#28765) and (b) the braking case (#28061).

5.4.2 Mode braking

The modelling results for the braking case (#28061) for both B-coil phases are shown in figure 5.17, where the mode frequency, the island width and the acting torques are illustrated. To match the experimental mode frequency evolution (figure 5.17 (a)) W_{vac} had to be increased by a factor of 4 in both B-coils phases. The impact on the island width directly remained unchanged in this case, hence the second fit parameter c_{ext} is equal to one. In the simulation

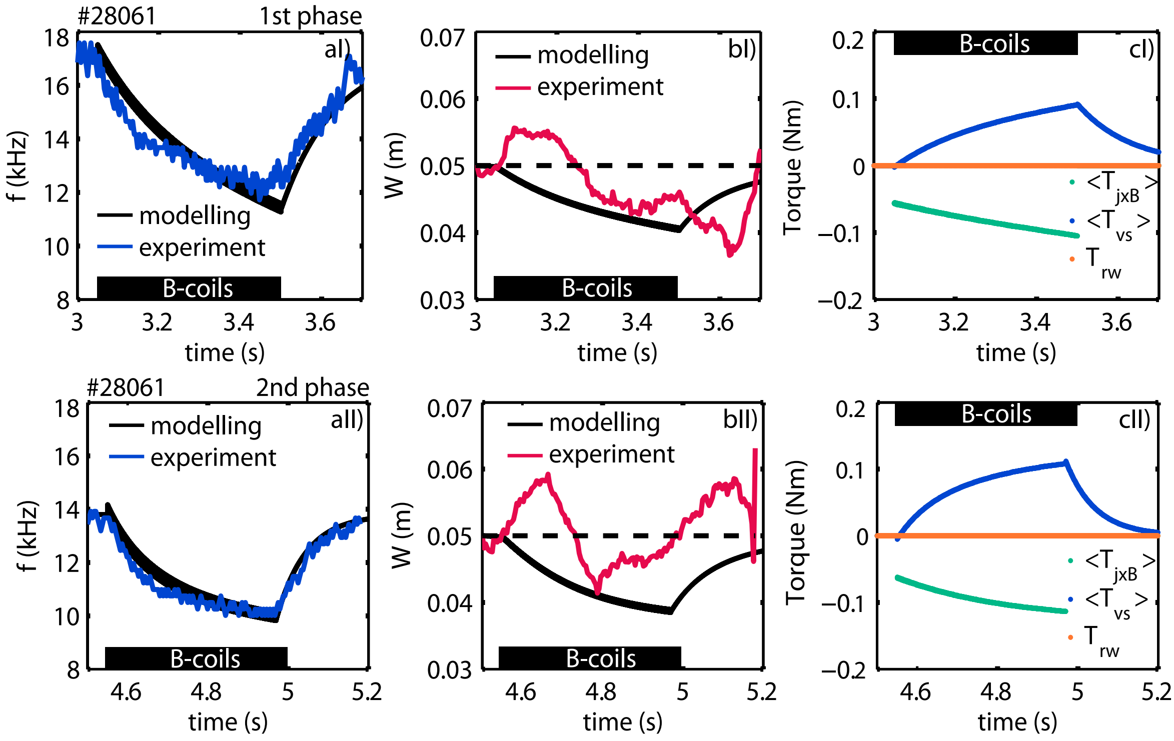

Figure 5.17: (a) Calculated mode frequency and (b) island width resulting from the modelling where the discussed assumptions are included. Each evolution is compared to the experimental quantities. (c) Time evolution of the acting torques, where the viscous and the $(\vec{j} \times \vec{B})$ torque are averaged over 2π are shown. On the top the first B-coil phase and on the bottom the second B-coil phase is illustrated.

the destabilisation in the first part of the B-coil phases can not be reproduced (figure 5.17 (b)) but the trend of stabilising the island in the second part of the B-coil phases can be modelled. However, the stabilising effect is slightly overestimated. The modelling results in a maximal resonant $(\vec{j} \times \vec{B})$ torque of around 0.1 Nm, visible in figure 5.17 (c). The resistive wall torque can be neglected for such high mode frequencies. Similar to the experiment for the braking case no big distortion of the simulated magnetic signal is visible. The small distortion can be detected in figure 5.16 (b) due to a visible enhancement of only the second harmonic during the B-coil phase.

5.4.3 Error field direction

From the comparison of the simulated and experimental pick-up coil signals the direction of the resulting error field for the locking case can be determined, which includes the external field but also other internal field contributions. The total resulting error field is responsible for the distortion of the mode signal. Its orientation in the toroidal plane determines the different impact on the mode depending on the toroidal location, like for example the braking and acceleration in different toroidal regions. By rotating the error field in the modelling until the modelled signal structure matches the experimental one for every coil position, the direction of the resulting error field can be determined [65]. The different coil positions of the coils shown in figure 5.15 and 5.3 are indicated in figure 5.18. The resulting error field direction can then be compared to the position of the locked mode in experiment and the position of the 2/1 vacuum field direction, which is assumed to have the dominating impact on the mode in the modelling in section 5.4.1.

The position of the locked mode in experiment is determined with saddle coils located at the high field side introduced in section 2.4.5. The 2/1 vacuum field direction is identified from the position of the 2/1 vacuum island. The resulting error field direction in the toroidal plane is indicated in figure 5.18 in orange. Additionally the experimental locked mode position in the toroidal plane (dark blue) and the position of the 2/1 vacuum island (red) is indicated. The experimental locked mode location is shifted about 40° in counter-current direction compared to the error field direction determined from the modelling (orange). The island does not lock ($\Delta\phi = 0$) in the minimum of the error field potential ($\sim -\cos(\Delta\phi)$) but is slightly driven, 'up the hill'. This is caused by the driving torque due to the plasma rotation and the viscous coupling to the island. Therefore a phase shift of less than 90° in counter-current direction on the basis of a counter rotating plasma (compare figure 5.1 (e)) is reasonable. However the 2/1 vacuum field location (red) does not agree with the determined error field direction. This implies that not only the 2/1 component of the MP field contributes to the slowing down and locking of the NTM but also other resonant components and the intrinsic error field. This means that a combination of resonant contributions at different resonant surfaces, caused by the external or intrinsic error field, act on the plasma. These torques together lead to a slowing down of the plasma and concomitant to a slowing down of the island. The interplay of these torques could lead to a deviation of the locking position from the single 2/1 vacuum field direction.

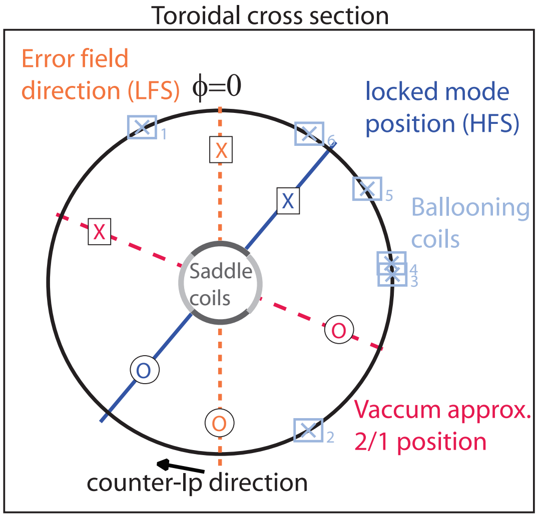

Figure 5.18: Location of the locked mode measured with the locked mode detector in dark blue compared to the resulting error field direction in orange and the position of the vacuum island in the toroidal plane in red. Additionally, the position of the pick-up coils used in figure 5.15 are indicated.

5.5 Reconstruction of the entire rotation profile during RMPs

In order to investigate the influence of different combination of torques, also at several rational surfaces, the evolution of the entire rotation profile (figure 5.19 (b)) is modelled for the braking case. The equation of motion is solved accounting for the radial dependence of all torques. The modelling results can then be compared to the experimentally observed profile evolution.

For this analysis the viscous torque T_{vs} with a constant momentum diffusion coefficient, described by equation (3.56), the resonant ($\vec{j} \times \vec{B}$) torque $T_{\mathrm{j\times B}}$, the non-resonant NTV torque T_{NTV} and the NBI input torque T_{NBI} with their radial dependences are included in the EOM. Additionally, the coupling of the (2/2) component of the 1/1 mode and the 3/2 NTM via T_{cpl}, observed in experiment are quantitatively taken into account [40]. In figure 5.19 the experimental rotation profiles from CXRS (panel (a)), the torques used for the modelling (panel (b)), and the modelled rotation profiles (panel (c) and (d)) are shown.

First of all the rotation profile at the beginning of the discharge without any big mode and external perturbation field being present is simulated (panel (c) blue). This is done by balancing the toroidal component of T_{NBI} and the viscous torque by adjusting the momentum diffusion coefficient D_ϕ in oder to achieve the red profile. The adjustment of the modelled profile (panel (c) blue) to the experimental profile yields a D_ϕ of around $0.4\,\mathrm{m^2/s}$. Example torque profiles of T_{NBI} and T_{vs} corresponding to a later time point (3.5 s) are shown in panel (b) in dark blue and light blue, respectively. The NBI deposition profile is taken from TRANSP simulations [100]. In the next step the green rotation profile (panel (a)), present shortly before the B-coils are switched on at 2.8 s is reproduced. At this time point already the 1/1 and the 3/2 NTM are present. To reproduce this flat profile mode coupling is included qualitatively, by introducing opposite torques T_{cpl} at the q=1, q=3/2 surface and in-between. These local torques are shown in green in panel (b) [40]. These torques are adjusted manually to reproduce the profile flattening observed in experiment. The modelled profile is shown in dark green in panel (c). Starting from the green rotation profile, where $T_{\phi,\mathrm{vs}}$ and T_{cpl} are now adjusted for, the influence of the calculated resonant ($\vec{j} \times \vec{B}$) and non-resonant (NTV) torques on the rotation profile can be investigated and compared to the experiment. To reproduce the decrease of the rotation profile observed in experiment due to the B-coils (green to red profile panel (a)), a local ($\vec{j} \times \vec{B}$) torque of 0.18 Nm at the q=3/2 surface has to be introduced. This is in good agreement with the 0.1 Nm calculated in section 5.4.2. The rotation decreases globally in the modelling, also when exerting a local torque, which agrees with the experimental profile evolution. This local torque is shown in red in panel (b). Almost the same rotation profile can be achieved, exerting smaller torques at different radial positions. For example exerting a torque of 0.07 Nm at each of the q=1, q=3/2 and q=2 surfaces, delivers almost the same rotation profile than in the previous case (light blue panel (d)). In the modelling of the entire rotation profile also the NTV torque profile, calculated in section 5.3 and shown in panel (b) in orange, can be included. Including T_{NTV} in the torque balance equation results in a decrease of rotation of around 0.4 kHz (orange profile panel (d)). This corresponds to around 8% of the total decrease of rotation observed in experiment (≈5 kHz). This confirms that the NTV is negligibly small. Therefore, the rotation damping and the concomitant slowing down of the NTM in the investigated discharges, can be assumed to be dominantly induced by the resonant perturbation field components. Additionally, it is shown that in fact the same decrease of rotation, also at a specific resonant surface, can be achieved when exerting several smaller torques at different resonant surfaces.

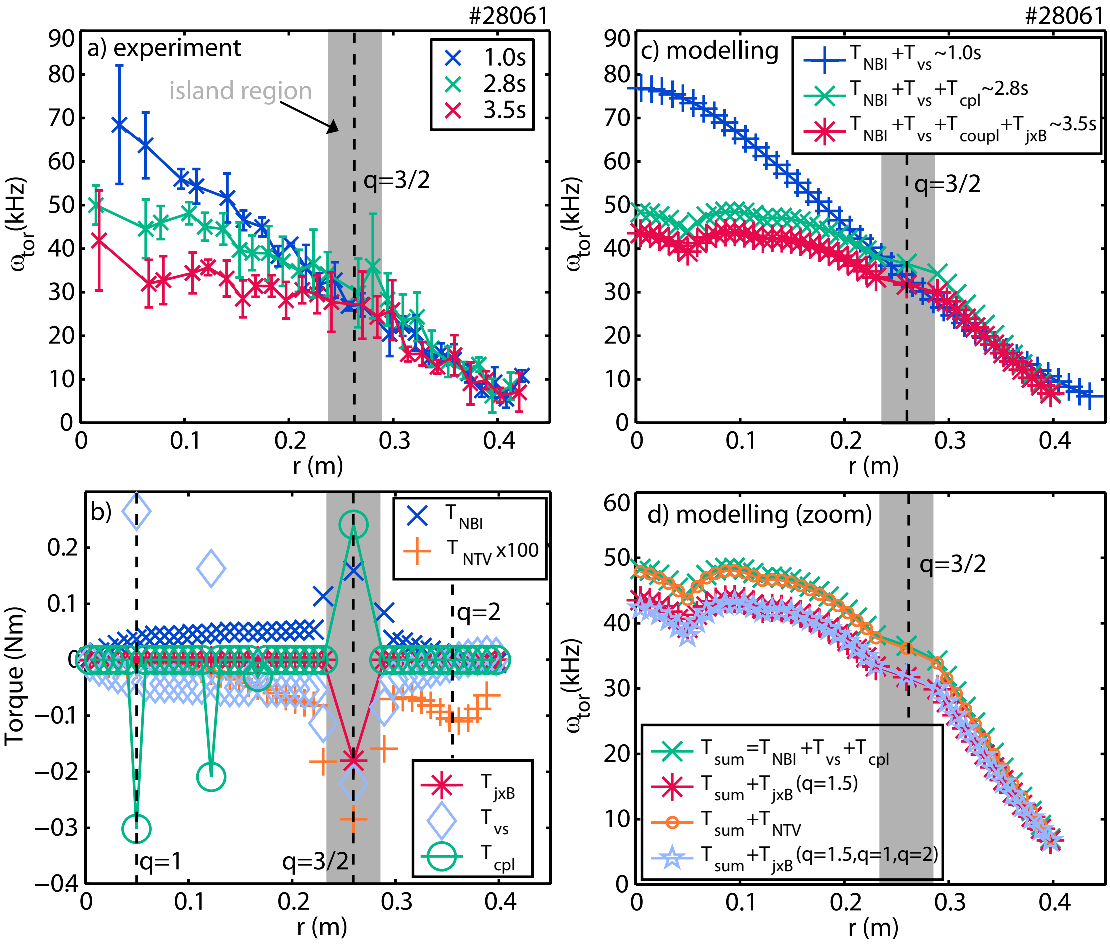

Figure 5.19: In (a) the experimental rotation profiles are shown at the beginning of the discharge (1.0 s) where no modes are present in dark blue, before switching on the B-coils (2.8 s) in green and at the end of the B-coil phase (3.5 s) in red. In (c) the corresponding modelled rotation profiles are shown, where the colour coding corresponds to (a). All torques used to achieve the red profile in (c) are shown in (b): the NBI torque (dark blue), the viscous torque (light blue), the coupling torque (green) and the resonant torque at the mode surface (red). Additionally the NTV torque profile calculated at 3.0 s at the beginning of the B-coil phase is shown in orange. Note that the NTV profile in (b) is scaled by a factor of 100. (d) Shows the small influence of the NTV torque (orange) compared to the resonant ($\vec{j} \times \vec{B}$) torque, which is almost the same exerting the torque at only one (red profile) or different radial positions (light blue).

5.6 Summary and Conclusions

The effect of MP fields on NTMs has been investigated in the AUG tokamak. Mode braking and locking due to the MPs is observed, as well as the spinning up of the mode when switching off the B-coils. In the investigated discharges the mode frequency as well as the global plasma rotation both decreases. In contrast, the mode amplitude is only slightly influenced. In the locking case a strong modulation of the island width and frequency is observed, directly via a distortion of the pick-up coil signals evolution and indirectly via the enhancement of higher harmonics in the spectrograms. This is less pronounced in the braking case, due to a higher mode rotation.

The NTV torque caused by the non-resonant MP components has been calculated accounting for the real perturbation field and plasma geometry. The calculation showed that the NTV torque is small and that its influence on the plasma rotation is negligible. Hence, the resonant MP components are dominant. Accounting only for the influence of the resonant MP field components the mode braking and locking, as well as the modulation of the island width, can be reproduced by the modelling. However, in both modelling cases the influence of the perturbation on the mode had to be increased, compared to the calculated vacuum approximations, to match the experimental frequency evolution. As a consequence, the effect on the island width is overestimated. This could be solved by including an additional torque in the modelling, which decreases the mode frequency but does not influence the island stability. Especially in the braking case, the presence of a 1/1 mode with the corresponding large resonant MP field component at the $q = 1$ surface reveals, that the influence of the 2/2 resonant component seems not to be insignificant.

For the locking case, the direction of the resulting error field, which is responsible for the modulation of the island width and frequency depending on the phase of the mode, could be determined from the modelling. The error field direction is in good agreement with the actual experimental locked mode position but it does not agree with the 2/1 vacuum island position. This leads to the assumption that the sum and interaction of different contributions, internal or external, influence the slowing down and locking of the mode and not only one dominant external component.

The modelling of the entire rotation profile for the braking case, accounting for the radial dependence of all torques and a constant momentum diffusion coefficient, reveals that a combination of smaller resonant torques at different surfaces can lead to the same rotation decrease at the mode surface as a single large torque at the NTM surface. This means that it is possible that smaller $(\vec{j} \times \vec{B})$ torques at several surfaces sum up to a total torque, which has the same effect as one large local one. This leads to a smaller influence on the mode stability at one specific resonant surface. This can additionally be confirmed with the fact that also in experiment (figure 5.6) vacuum islands induced by the external MP field appear at several different surfaces. Most of them are smaller than the dominating one at the position of the NTM but in sum they seem to have a significant impact. Additionally, the $v_{\perp,\mathrm{e}}$ for both discharges is small, which reveals that these additional components could influence the plasma in the linear regime.

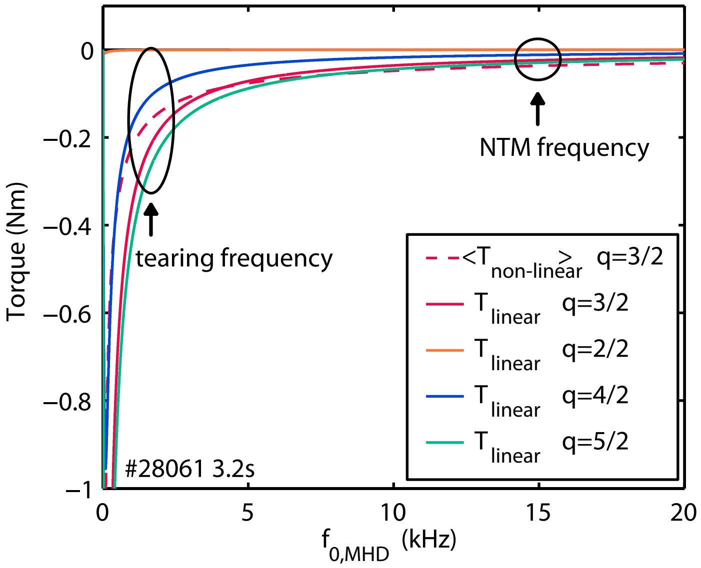

Figure 5.20: The linear torques (equation (3.46)) depending on the tearing frequency $f_{0,\mathrm{MHD}}$ at the q=1, 3/2, 2 and 5/2 surface induced by a static MP field with n=2 and m= 2, 3, 4, 5 for the braking case are shown. The used input parameters are listed in table 5.3. A constant resistivity η has been assumed and $r_\mathrm{s}\Delta_0'$ is estimated via $-m$. For the q=3/2 surface also the time averaged non-linear torque (equation (3.41)) is shown depending on the actual mode frequency in this case and the parameters listed in table 5.1. The range of the tearing frequencies relevant for the linear theory and the NTM frequency relevant for the non-linear case are also shown. According to the estimation of $v_{\perp,e}$ (≅tearing frequency) in figure 5.5 the actual tearing frequency for the q=1,2 and 5/2 surface is small compared to the NTM frequency.

To estimate this influence the linear torques for the braking case at the q=1, 3/2, 2 and 5/2 surfaces are roughly estimated and shown in figure 5.20. The input parameters are summarised in table 5.3. For the NTM surface at q=3/2 also the non-linear torque is shown. The linear and non-linear torque are of the same order of magnitude. The linear torque at the q=1 surface is small due to an almost flat q profile towards the core. However, according to the estimated tearing frequencies which are assumed to be equal to $v_{\perp,e}$, the linear torques at these surface are large. Therefore, even if these components are shielded, they are able to contribute significantly to the total torque as supposed before.

In summary, the experimental observation and modelling results show that in the locking case the sum of several small resonant contributions in the linear phase, in addition to the

Table 5.3: Input parameters for the calculation of the linear torque for #28061 at 3.2 s

q-surfaces	r_res (m)	$\langle W_\mathrm{vac}\rangle$ (m)	τ_res (s)	τ_rec (s)	C (T/m)
1	0.07	0.054	0.0419	0.0027	0.0037
3/2	0.28	0.043	0.3284	0.0022	0.0807
2	0.34	0.027	0.4842	0.0017	0.1103
5/2	0.37	0.04	0.5734	0.0014	0.1152

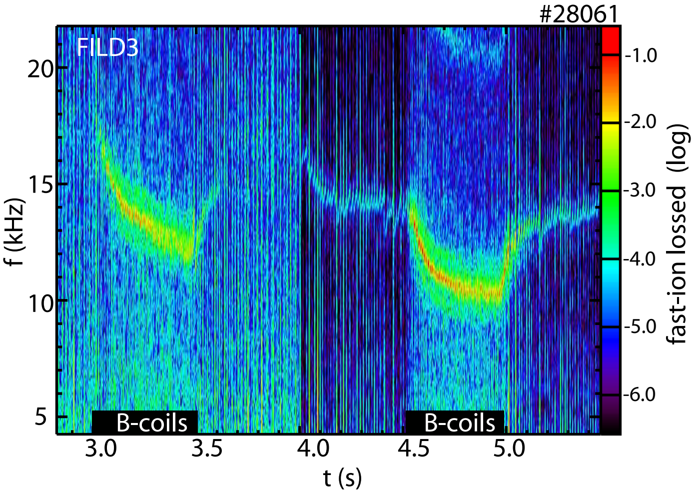

Figure 5.21: Spectrogram of the fast-ion losses detected with a fast-ion loss detector (FILD3) located at the plasma edge. The fast-ion losses caused by the NTM alone are not significant but they are strongly enhanced during the B-coils phases when the mode is slowed down.

contribution of the resonant component at the NTM surface (non-linear) and the intrinsic error field seem to be responsible for the slowing down and the locking of the NTM. In the braking case besides the small linear resonant contributions at several surfaces and the bigger non-linear one at the NTM surface, the impact of the 2/2 MP component on the 1/1 mode seem to play a crucial role. This could explain the factor of 4 increase of the single resonant component required in the modelling compared to a factor of only 2 in the locking case.

In addition to the $(\vec{j} \times \vec{B})$ torques induced by the B-coils in both discharges, the torque induced by the loss of fast-ions [88, 89] could be an additional contribution. In figure 5.21 a spectrogram of the fast-ion losses measured with a fast-ion loss detector (FILD [101]) is illustrated for the braking case. The losses are clearly correlated with the mode frequency and increase strongly during the B-coil phases, when the mode is slowed down. In addition, also the cylindric approximation of the resonant effects and their parametrisation via the vacuum approximation is responsible for deviations from the experimental observations.

Concluding, the NTV caused by the MP field seems to be small at AUG but the resonant torques at different resonant surfaces act together as a global resonant torque that is responsible for the rotation damping. To describe the evolution of a single magnetic island accounting for the influence of the resonant MPs, all resonant contributions at several surfaces, either in the non-linear or linear regime, have to be taken into account. However, even if the NTV is negligible at AUG it can be important for ITER. Since ITER will operate at significantly higher temperatures and lower collisionalities this will lead according to theory and e.g. equation (3.50), assuming a similar perturbation field amplitude, to a larger NTV torque.

Chapter 6

Summary and Outlook

6.1 Summary

In this thesis different aspects concerning the stability and rotation dependence of neoclassical tearing modes (NTMs) have been investigated. NTMs become destabilised as a consequence of a seed perturbation induced by a triggering instability. They are driven by a loss of helical bootstrap current and mainly develop in plasmas with high pressure. NTMs are resistive MHD instabilities and thus, they are accompanied by a change in the plasma topology due to the formation of magnetic islands. Over the island region the plasma pressure is radially flattened, which results in a loss of energy confinement. Additionally, an NTM can slow down the plasma rotation, lock to the vessel wall, flush out all the confined plasma energy and terminate a discharge via a disruption.

In present day experiments operation is still possible in the presence of NTMs, whereas in larger tokamaks the effects of NTMs will not be acceptable. In the next fusion device ITER, the confinement reduction will limit the achievable fusion power and a disruption caused by an NTM is even likely to damage the machine. Therefore, in ITER these instabilities have to be avoided or at least mitigated. Controlling these instabilities is based on a detailed understanding and predictions made from observations in present day devices.

One key issue, concerning the predictions for ITER, is the influence of plasma rotation on NTMs, especially at the NTM onset. ITER will be operated at low plasma rotation, which is opposite to most present day experiments. No theory is currently available to describe the relation. Experiments are therefore required to provide a basis for the theory to describe the physics. Additionally scalings can be developed from the experiments and extrapolated in order to predict the NTM behaviour in the parameter range relevant for ITER. Another important aspect is the effect of externally applied magnetic perturbation fields on the NTM stability and rotation. These fields will be used in ITER primarily for the mitigation of edge instabilities. As a side effect, they can also slow down an NTM and the plasma rotation, which enhances the appearance of locked modes. Additionally, they can also influence the NTM stability. This interaction has to be predicted via modelling for ITER. The available models and the according theories have to be validated on present day experiments. Both topics have been studied within the scope of this thesis at the ASDEX Upgrade tokamak.

The influence of rotation on the NTM onset threshold has been investigated on the basis of a database including around 70 discharges. This database has been built for $(m/n)=(3/2)$ NTMs. For most of the NTM onsets, additionally, the trigger mechanism could be identified either as an ELM, fishbone, sawtooth crash, general 1/1 MHD, or 'triggerless' case. Based on this database the influence of rotation, the rotation gradient and the differential rotation between the trigger and the NTM surface, on the NTM onset threshold have been analysed. In all correlations the scatter could be reduced using quantities normalised to the Alfvén velocity, which is in agreement with observations at other experiments. The work presented in this thesis shows that the NTM onset threshold increases with increasing co- and counter-current rotation. Hence, the NTM onset behaviour does not depend on the direction of the plasma rotation and NTMs can more easily be triggered at low plasma rotation. This is contrary to the results of DIII-D [73] where a further decrease in the threshold with increasing counter-current rotation was observed. However, the AUG results suggest to re-analyse the DIII-D data. Furthermore, the formation of an upper NTM onset threshold with normalised rotation was observed. All NTM onset data points, as well as data points taken from discharges without any NTM activity, are situated below this threshold. This shows that the appearance of NTMs clearly limits the operational space in terms of the plasma pressure. This upper onset threshold increases with increasing normalised plasma rotation but is less distinct at low plasma rotation. This indicates that the NTM behaviour changes at low rotation. The observation that the triggerless cases appear mainly at low rotation further confirm this. At low normalised rotation Δ' is less stabilising, and hence, the equilibrium current profile appears to be different.

In contrast, at the marginal point, shortly before the mode disappears and the trigger process plays no role anymore, no dependence is observed so far. This indicates that the dependence on rotation at the onset is caused by an influence of rotation on the trigger mechanism. Additionally, a linear dependence on the normalised rotation gradient at the resonant surface is found, although the scatter is increased. This implies that steeper rotation profiles hamper the appearance of NTMs. In addition, high differential rotation seems to impede the triggering process for ELMs and fishbones as a trigger, but not for sawtooth crashes.

To summarise the main results of this study according to the questions posed in the introduction:

- NTMs can more easily be triggered at low plasma rotation.
- Rotation seems to influence both the seeding process as well as the intrinsic NTM stability via Δ', which appears to be less stabilising at low plasma rotation.
- The rotation gradient appears to be stabilising, as well as a high differential rotation between the triggering and the NTM surface, at least for the fishbone and ELM triggered cases.
- Contrary to results at DIII-D, at AUG the NTM onset threshold increases with normalised rotation, independent of the plasma rotation direction. This suggests to re-

analyse the DIII-D data.

- For ITER, this study indicates that NTMs will be less stable, most probably due to a combination of a less stabilising Δ' term and a stronger impact of the trigger instabilities at low rotation. To avoid the appearance of NTMs both effects have to be controlled. The former could be influenced by controlling the equilibrium current profile, via local current drive for example. For the latter the triggering process has to be hampered. For ELM and fishbone as trigger this may be realised by steepening the rotation profiles - although unfortunately it will not be able to control the rotation in ITER. This will not influence the triggering by a sawtooth crash, due to its immense impact. Nevertheless, one possibility lies in the avoidance of large sawtooth crashes. This can be obtained by driving current inside the $q = 1$ surface, which increases the sawtooth frequency and consequently reduces the size of the sawtooth crashes [102].

The impact of externally applied magnetic perturbation (MP) coils on already existing rotating NTMs has been studied using the 16 in-vessel saddle coils installed recently at the low field side of AUG [8]. This set of coils, called B-coils, enables the generation of MP fields with a toroidal mode number of $n \leq 4$. These low mode numbers are suitable for the study of the influence of MPs on the (m/n)=(3/2) and (2/1) NTMs, which are the most common confinement degrading NTMs in AUG.

The B-coils produce MP fields containing resonant and non-resonant components. The resonant components of the MP field can penetrate the plasma and provoke magnetic reconnection at a resonant surface. Additionally, it can lead to a modulation of the island width and frequency of a pre-existing rotating mode. The modulation of the island width and frequency is phase shifted which, on average, leads to a slowing down and a shrinking of a rotating mode as well as to a growth of a locked mode. The non-resonant components of the MP field do not influence the NTM stability but they induce a global NTV braking torque. In summary, the B-coils can influence the island amplitude and phase evolution of an NTM.

Two discharges have been analysed in detail. In both, an influence of the MPs on already existing rotating NTMs has been observed. Mode braking of a 3/2 NTM and locking of a 2/1 NTM due to the MPs is observed in each of the discharges, as well as the spinning up of the mode when the B-coils are switched off. In the investigated discharges both the mode frequency and the global plasma rotation decreases. The mode amplitudes are only slightly influenced. In the locking case a strong modulation of the island width and frequency is observed directly - via a distortion of the pick-up coil signal evolution, and indirectly - via the enhancement of higher harmonics in its spectrogram. This is less pronounced in the braking case, due to a higher mode frequency. According to theory most of the experimental observations can be explained by the influence of the resonant MP components.

The non-resonant NTV torque has been calculated for the braking case taking into account the real geometry of the perturbation field and the plasma. This calculation confirmed that the NTV torque is small in the investigated discharges, which supports that the influence of the resonant MP components seems to be dominant. Accounting only for the resonant effects at the position of the mode, the mode braking and locking could be modelled. To match the experimental mode frequency the impact of the perturbation field on the mode evolution had to be increased. At the same time, this leads to an overestimation of the effect on the mode stability. This observation reveals that an additional contribution is missing in the model, which slows down the mode but does not affect the island stability, like several resonant torques at other resonant surfaces would do. Nevertheless, the modulation of the island frequency and amplitude as observed experimentally is well reproduced.

For the locking case, additionally, the error field direction could be determined from the modelling. The resulting error field direction is in good agreement with the actual locked mode position determined experimentally. However, it does not agree with the 2/1 vacuum island position, which is assumed to be the dominant contribution in the modelling. This supports the hypothesis that different contributions influence the braking and locking of the mode as well as the intrinsic error field.

In addition, the entire rotation profile was modelled accounting for the radial dependence of all torques and a constant momentum diffusion coefficient. It was observed that a combination of smaller resonant torques at different surfaces can lead to the same rotation decrease at the mode surface as a single large torque. This would lead to a smaller effect on the mode amplitude at one specific resonant surface. This is supported by the fact that for both cases vacuum islands, induced by the external MP field, appear at several surfaces. They could influence the plasma rotation in the linear regime and it was shown that they appear to have a significant impact.

The experimental observations and the modelling results show that, in the locking case, the sum of several resonant contributions in the linear regime, in addition to the contribution of the resonant component at the NTM surface and the intrinsic error field seems to be responsible for the slowing down and the locking of the NTM. In the braking case, besides the linear resonant contributions at several surfaces and the bigger non-linear one at the NTM surface, the impact of the 2/2 MP component on the 1/1 mode appears to play a crucial role. This could explain the factor of 4 increase of the single resonant component required in the modelling compared to a factor of only 2 in the locking case. The summary of this analysis leads to the following answers to the question posed in the introduction:

- Mode braking and locking due to the MPs is observed, as well as the spinning up of the modes when switching off the B-coils. The mode amplitudes are only slightly influenced. Additionally, a direct modulation of the island width and frequency can be detected.

- The influence of the resonant MP components appears to be dominant.

- Most of the experimental observations can be explained by the resonant effects. Mode braking and locking can be modelled accounting only for those. However, taking only the resonant effects at the mode surface into account, matching the island frequency requires an increase of the resonant component of up to 4. This at the same time leads to an overestimation of the influence on the island amplitude.

- This can be solved, when the resonant torques at different resonant surfaces act together as a global resonant torque, that appears to be responsible for the rotation damping. Therefore, in order to model the evolution of one single NTM, all resonant components at several surfaces have to be included in the modelling in the linear regime as well as in the non-linear regime, especially for surfaces where additional islands are present. In addition, the torque induced by the loss of fast-ions, which is strongly enhanced during the B-coil phases [88, 89], could be a further contribution. The non-resonant NTV torque strongly depends on the ion temperature ($T_{\mathrm{i}}^{7/2}$) and the plasma collisionality. Therefore, even if the NTV is small at AUG, for ITER, with its high temperatures and low collisionalities, the influence of the NTV can not be excluded. This could lead to an additional effect on the island frequency evolution, which has to be taken into account.

6.2 Outlook

It is important to validate the presented calculation for the NTV with other independent calculations or codes. Furthermore, a more general estimation of the NTV, combining the formulae valid in the $1/\nu$ and ν regime, is needed. Both aspects are essential for the use of the calculation later on in order to examine the parameter regime of the NTV, its dependence on kinetic profiles, and different B-coils configurations both theoretically and experimentally. According to these calculations dedicated experiments should be performed. Furthermore, experiments at low density, resulting in lower collisionalities like in ITER, should be performed in order to predict the influence of the NTV in ITER. Additionally, the model for the NTM evolution has to be extended to calculate the impact of the B-coils on one mode including all different resonant surfaces and the according resonant effects, in the linear and non-linear regimes. Another important issue is the estimation of the torque caused by the loss of fast ions, which is significantly enhanced during the B-coils phases. It has to be checked if this torque also contributes to the slowing down of the plasma. In addition, discrepancies between the vacuum approximation for the island width and the VMEC code, which calculates the ideal plasma response, are observed but not discussed in this work. These discrepancies concern the determination of resonant and non-resonant configurations, and the corresponding expected influence on the plasma. Dedicated experiments are required to clarify these discrepancies. Finally, it would be important to extend the experimental database in order to confirm the present findings in comparison to other devices. First of all it would be interesting to repeat the discharges presented in this work. In particular it should be investigated if the evolution of the island width and for example the development of the sidebands in the braking case and the error field direction in the locking case, are reproducible and can be explained. Since so far only a few cases exist, where an influence of the B-coils on NTMs is observed, further experiments in which the influence of the resonant MPs is maximised have to be performed. Low density, a clear ‘resonant’ configuration, low plasma rotation and also a lower magnetic field are predicted to maximise the effect of the resonant MPs.

Bibliography

[1] TIPLER, P. A. / LLEWLLYN, R. A., *Moderne Physik*, Oldenbourg Verlag München Wien, 1^{st} edition, 2003.

[2] HERRMANN, A. et al., Fusion Science and Technology **44** (2003) 569.

[3] WESSON, J., *Tokamaks*, Oxford University Press, 3^{rd} edition, 2004.

[4] HINTON, F. L. et al., Rev. Mod. Phys. **48** (1976) 239.

[5] HELANDER, P. et al., *Collisional Transport in Magnetized Plasmas*, Cambridge University Press, 2005.

[6] The ITER Project, http://www.iter.org.

[7] ZOHM, H., Plasma Physics and Controlled Fusion **38** (1996) 105.

[8] SUTTROP, W. et al., Fusion Engineering and Design **84** (2009) 290 , Proceedings of the 25th Symposium on Fusion Technology (SOFT-25).

[9] ROTT, M. et al., Fusion Engineering and Design **84** (2009) 1653 , Proceedings of the 25th Symposium on Fusion Technology (SOFT-25).

[10] SUTTROP, W. et al., Fusion Engineering and Design (2013) .

[11] D'HAESELEER, W., *Flux Coordinates and Magnetic Field Structure-A Guide to a Fundamental Tool of Plasma Theory*, Springer-Verlag, 1991.

[12] SUTTROP, W. et al., Phys. Rev. Lett. **106** (2011) 225004.

[13] McDERMOTT, R. M. et al., Plasma Physics and Controlled Fusion **53** (2011) 124013.

[14] McDERMOTT, R. M. et al., Plasma Physics and Controlled Fusion **53** (2011) 035007.

[15] MANINI, A. et al., Nuclear Fusion **46** (2006) 1047.

[16] SOMMER, F. et al., Nuclear Fusion **52** (2012) 114018.

[17] McCARTHY, P. J., Physics of Plasmas **6** (1999) 3554.

[18] DUNNE, M. et al., Nuclear Fusion **52** (2012) 123014.

[19] RATHGEBER, S. K. et al., Plasma Physics and Controlled Fusion **55** (2013) 025004.

[20] SUTTROP, W. et al., Practical limitations to plasma edge electron temperature measurements by radiometry of electron cyclotron emission, Technical Report 1/306, IPP, Garching, Germany, 1996.

[21] KURZAN, B. et al., Review of Scientific Instruments **82** (2011) 103501.

[22] SCHWEINZER, J. et al., Plasma Physics and Controlled Fusion **34** (1992) 1173.

[23] FISCHER, R. et al., Plasma Physics and Controlled Fusion **50** (2008) 085009.

[24] WILLENSDORFER, M. et al., Review of Scientific Instruments **83** (2012) 023501.

[25] MLYNEK, A. et al., Review of Scientific Instruments **81** (2010) 033507.

[26] FISCHER, R. et al., Fusion Science and Technology **58** (2010) 675.

[27] VIEZZER, E. et al., Review of Scientific Instruments **83** (2012) 103501.

[28] SOKOLL, M., MHD-Instabilitäten in magnetisch eingeschlossenen Plasmen und ihre tomographische Rekonstruktion im Röntgenlicht, Technical Report 1/309, IPP, Garching, Germany, 1997.

[29] TANZI, C., *Emission of soft X-ray and microwave radiation from tokamak plasmas*, PhD thesis, Universiteit Utrecht, 1996.

[30] REICH, M. et al., Fusion Science and Technology **61** (2012) 309.

[31] MARASCHEK, M. et al., (2013), Proceedings of the 40th European Physical Society Conference on Plasma Physics, Espoo, Finland, 2013, No. MCF/P4.127.

[32] ZOHM, H., Vorlesungsskript: MHD-Gleichgewichte und Stabilität heißer Fusionsplasmen, Technical report, Max-Planck-Institut für Plasmaphysik, 2004.

[33] FURTH, H. P. et al., Physics of Fluids **6** (1963) 459.

[34] ZOHM, H., *Untersuchung magnetischer Moden am Tokamak ASDEX*, PhD thesis, Universität Heidelberg, 1990.

[35] WILSON, H., Fusion Science and Technology **53** (2008) 152.

[36] HEGNA, C. C. et al., Physics of Plasmas **4** (1997) 2940.

[37] FITZPATRICK, R., Nuclear Fusion **33** (1993) 1049.

[38] RUTHERFORD, P. H., Physics of Fluids **16** (1973) 1903.

[39] HEGNA, C. C. et al., Physics of Plasmas **1** (1994) 2308.

[40] CLASSEN, I., *Imaging and Control of Magnetic Islands in Tokamaks*, PhD thesis, Technische Universiteit Eindhoven, 2007.

[41] QU, W. X. et al., (1985), University of Wisconsin Report No. UWPR 85-5.

[42] CARRERA, R. et al., Physics of Fluids **29** (1986) 899.

[43] LA HAYE, R. J., Physics of Plasmas **13** (2006) 055501.

[44] SAUTER, O. et al., Physics of Plasmas **6** (1999) 2834.

[45] FITZPATRICK, R., Physics of Plasmas **2** (1995) 825.

[46] WILSON, H. R. et al., Physics of Plasmas **3** (1996) 248.

[47] POLI, E., Magnetic islands in tokamak plasmas, Habilitationsschrift Universität Ulm, 2011.

[48] POLI, E. et al., Phys. Rev. Lett. **94** (2005) 205001.

[49] BERGMANN, A. et al., Physics of Plasmas **12** (2005) 072501.

[50] WILSON, H. R. et al., Plasma Physics and Controlled Fusion **38** (1996) A149.

[51] JAMES, M. et al., Plasma Physics and Controlled Fusion **52** (2010) 075008.

[52] CONNOR, J. W. et al., Physics of Plasmas **8** (2001) 2835.

[53] GUDE, A. et al., Nuclear Fusion **39** (1999) 127.

[54] COLE, A. J. et al., Phys. Rev. Lett. **99** (2007) 065001.

[55] FITZPATRICK, R., Physics of Plasmas **5** (1998) 3325.

[56] HUA, M.-D. et al., Plasma Physics and Controlled Fusion **52** (2010) 035009.

[57] SHAING, K. C., Physics of Plasmas **10** (2003) 1443.

[58] COLE, A. et al., Low collisionality neoclassical toroidal viscosity in tokamaks and quasi-symmetric stellerators using integral-truncation technique, Technical report, UW CPTC Report 08-8, Wisconsin, 2009.

[59] CALLEN, J. et al., Nuclear Fusion **49** (2009) 085021.

[60] CALLEN, J. D. et al., Physics of Plasmas **16** (2009) 082504.

[61] GAROFALO, A. M. et al., Physics of Plasmas **16** (2009) 056119.

[62] GAROFALO, A. M. et al., Phys. Rev. Lett. **101** (2008) 195005.

[63] STIX, T. H., Physics of Fluids **16** (1973) 1260.

[64] KLÜBER, O. et al., Nuclear Fusion **31** (1991) 907.

[65] ZOHM, H. et al., EPL (Europhysics Letters) **11** (1990) 745.

[66] FIETZ, S. et al., Plasma Physics and Controlled Fusion **55** (2013) 085010.

[67] LA HAYE, R. J. et al., Physics of Plasmas **17** (2010) 056110.

[68] WAELBROECK, F. L. et al., Phys. Rev. Lett. **87** (2001) 215003.

[69] NAVE, M. F. F. et al., Physics of Plasmas **13** (2006) 014503.

[70] GRAVES, J. P. et al., Plasma Physics and Controlled Fusion **47** (2005) B121.

[71] HEGNA, C. C. et al., Physics of Plasmas **6** (1999) 130.

[72] BUTTERY, R. J. et al., Proceedings of the 22nd IAEA Fusion Energy Conference, Geneva, Switzerland, 2008 (International Atomic Energy Agency, Vienna, 2003), Paper No. IT/P6-8.

[73] BUTTERY, R. J. et al., Physics of Plasmas **15** (2008) 056115.

[74] GERHARDT, S. et al., Nuclear Fusion **49** (2009) 032003.

[75] SAUTER, O. et al., Physics of Plasmas **4** (1997) 1654.

[76] YU, Q., Nuclear Fusion **50** (2010) 025014.

[77] ITER Physics Expert Group on Confinement and Transport and ITER Physics Expert Group on Confinement Modelling and Database, ITER Physics Basis Editors, Nuclear Fusion **39** (1999) 2175.

[78] ZOHM, H. et al., Final report, EFDA Contract 03-1060, Tasks TW3-TPHE-ECHULA/ECHULB, Del. (f).1, 2005.

[79] MEISTER, H., Untersuchungen zur Plasmarotation und Impulstransport in ASDEX Upgrade, Master's thesis, Universität Augsburg, 1997.

[80] LA HAYE, R. et al., Physics of Plasmas **10** (2003) 3644.

[81] HENDER, T. et al., Nuclear Fusion **32** (1992) 2091.

[82] EVANS, T. E. et al., Phys. Rev. Lett. **92** (2004) 235003.

[83] STRAIT, E. J. et al., Physics of Plasmas **11** (2004) 2505.

[84] HU, Q. et al., Nuclear Fusion **52** (2012) 083011.

[85] EVANS, T. et al., Nuclear Fusion **48** (2008) 024002.

[86] SCHMITZ, O. et al., Plasma Physics and Controlled Fusion **50** (2008) 124029.

[87] MORDIJCK, S. et al., Plasma Physics and Controlled Fusion **53** (2011) 122001.

[88] GARCIA-MUNOZ, M. et al., Nuclear Fusion **IAEA-CN-197** (2012) EX/P6.

[89] GARCIA-MUNOZ, M. et al., (2013), Proceedings of the 40th European Physical Society Conference on Plasma Physics, Espoo, Finland, 2013, No. MCF/I5.114.

[90] KOSLOWSKI, H. et al., Nuclear Fusion **46** (2006) L1.

[91] YU, Q. et al., Nuclear Fusion **48** (2008) 024007.

[92] FIETZ, S. et al., (2013), Proceedings of the 40th European Physical Society Conference on Plasma Physics, Espoo, Finland, 2013, No. MCF/P5.158.

[93] FIETZ, S. et al., Plasma Physics and Controlled Fusion , submitted.

[94] WAELBROECK, F., Nuclear Fusion **49** (2009) 104025.

[95] FERRARO, N. M., Physics of Plasmas **19** (2012) 056105.

[96] BERGMANN, A., NTV due to non-axisymmetric magnetic field perturbation, https://www.aug.ipp.mpg.de/aug/ringberg2010/presentations/, ASDEX Upgrade Programme Seminar, Ringberg 2010.

[97] ZHU, W. et al., Phys. Rev. Lett. **96** (2006) 225002.

[98] CALLEN, J., Nuclear Fusion **51** (2011) 094026.

[99] SUN, Y. et al., Nuclear Fusion **52** (2012) 083007.

[100] PANKIN, A. et al., Computer Physics Communications **159** (2004).

[101] GARCIA-MUNOZ, M. et al., Review of Scientific Instruments **80** (2009) 053503.

[102] CHAPMAN, I. T. et al., Nuclear Fusion **53** (2013) 066001.

Appendix A

Summary of important parameters and abbreviations

A.1 List of important parameters

a	plasma minor radius (m)
$\vec{B}$	magnetic field (T)
B_0	toroidal magnetic field at the magnetci axis (T)
B_{pol}	poloidal magnetic field (T)
B_{r}	radial magnetic field (T)
B_{tor}	toroidal magnetic field (T)
B_{tot}	total magnetic field (T)
c	speed of light ($2.9979 \cdot 10^8\,\mathrm{m/s}$)
D_Φ	momentum diffusion coefficient ($\mathrm{m^2/s}$)
$\vec{E}$	electric field (V/m)
e	elementary charge ($1.6022 \cdot 10^{-19}\,\mathrm{C}$)
I	moment of inertia ($\mathrm{kg\,m^2}$)
I_{p}	plasma current (A)
I_λ	pitch angle integral
J	Jacobian
$\vec{j}$	current density ($\mathrm{A/m^2}$)
$\vec{k}$	wave vector (1/m)
$\ln\Lambda$	Coulomb logarithm
Ma_{A}	Alfvén Mach number
m	poloidal mode number
$m_{\mathrm{e,i}}$	electron, ion mass (kg)
n	toroidal mode number

$n_{\mathrm{e,i}}$	electron, ion density ($1/\mathrm{m}^3$)
P	power (W)
p	kinetic plasma pressure ($\mathrm{Pa}=\mathrm{N}/\mathrm{m}^2$)
q	safety factor
$q_{\mathrm{e,i}}$	electron, ion charge (C)
R	major plasma radius (m)
R_0	major plasma radius at the magnetic axis (m)
R_{tang}	NBI tangential radius (m)
r	minor plasma radius - used as radial label (m)
$\vec{T}$	torque (Nm)
$T_{\mathrm{e,i}}$	electron, ion temperature (K or eV)
$\vec{v}$	plasma rotation velocity (m/s)
v_{A}	Alvén velocity (m/s)
v_{th}	thermal velocity (m/s)
$v_{\perp\mathrm{e,i}}$	electron, ion perpendicular velocity (m/s)
$v^*_{\mathrm{e,i}}$	electron, ion diamagnetic drift velocity (m/s)
W	island width (m)
W_{tot}	total plasma energy (m)
Z	atomic number
β_{pol}	poloidal plasma β
β_{N}	β normalized
ϵ	inverse aspect ratio
ϵ_0	dielectric constant ($8.85421\cdot 10^{-12}\,\mathrm{C}/(\mathrm{V\,m})$)
η	electrical resistivity ($\Omega\,\mathrm{m}$)
θ	poloidal coordinate
Γ	particle flux ($\mathrm{T}/(\mathrm{s\,m}^2)$)
μ_0	magnetic constant ($4\pi\ 10^{-7}\mathrm{Vs}/(\mathrm{A\,m})$)
$\mu_{\|\|}$	toroidal viscosity frequency (1/s)
ρ	mass density (kg/m^3)
ρ_{pol}	poloidal flux coordinate
$\rho_{\theta,\mathrm{i}}$	ion poloidal gyro radius (m)
σ	electrical conductivity ($1/(\Omega\,\mathrm{m})$)
τ_{e}	energy confinement time (s)
τ_{ii}	ion-ion collision time (s)
τ_{H}	hydromagnetic time-scale (s)
τ_{rec}	reconnection time-scale (s)

τ_{res}	plasma resistive time-scale (s)
τ_{V}	viscous diffusion time-scale (s)
τ_{wall}	resistive time scale of the wall (s)
τ_{Φ}	momentum confinement time (s)
ϕ	toroidal coordinate
Ψ	poloidal magnetic flux function (Vs)
Ω_{ϕ}	toroidal rotation frequency (1/s)
$\Omega^{*}_{\mathrm{e,i}}$	electron, ion diamagnetic drift frequency (1/s)
Ω^{*}_{NC}	neoclassical offset frequency (1/s)
ω	mode frequency (1/s)
$\omega_{\mathrm{ce,ci}}$	electron, ion cyclotron frequency (1/s)
ω_{p}	plasma frequency (1/s)
$\omega_{\mathrm{te,ti}}$	electron, ion transit frequency (1/s)

A.2 List of abbreviations

AUG	ASDEX Upgrade
CXRS	charge exchange recombination spectroscopy
ECCD	electron cyclotron current drive
ECE	electron cyclotron emission
ECRH	electron cyclotron resonance heating
ELM	edge localised mode
EOM	equation of motion
ICRH	ion cyclotron resonance heating
IDA	integrated data analysis
LIB	lithium beam
MHD	magneto hydrodynamic
MP	magnetic perturbation
MRE	modified Rutherford equation
NBI	neutral beam injection
NTM	neoclassical tearing mode
NTV	neoclassical toroidal viscosity
PSL	passive stabilising loop
SEP	separatrix
SOL	scrape off layer
SXR	soft X-Ray
TS	Thomson scattering

Danksagung

Mein besonderer Dank gilt Prof. Hartmut Zohm, der es mir nicht nur ermöglicht hat meine Doktorarbeit am IPP zuschreiben, sondern der mich auch stets akademisch als auch fachlich aufmerksam betreut hat. Vor allem möchte ich Ihm für die Zeit, die er sich stets für mich genommen hat, die langen Diskussionen, das Interesse und die guten Ratschläge, die für mich unglaublich hilfreich waren, danken.

Mein besonderer Dank gilt auch Dr. Marc Maraschek, der mir immer mit Rat und Tat zur Seite stand, stets Zeit für mich hatte und von dem ich unglaublich viel gelernt habe.

Weiterhin möchte ich Dr. Ivo Classen herzlich danken, für die fruchtbaren Diskussionen, die guten Anregungen und seine Bereitschaft mir all meine unzähligen Fragen zu beantworten.

Besonders dankbar bin ich auch Dr. Francois Ryter, Dr. Emiliano Fable und Dr. Jörg Hobirk, die mir bei der schwierigen Aufgaben meiner ersten Veröffentlichung unglaublich geholfen, mich dabei stetig unterstützt, wieder aufgebaut und angetrieben und mich durch Höhen und Tiefen begleitet haben.

Ich möchte Dr. Andreas Bergmann und Dr. Qingquan Yu für ihre Unterstützung auf theoretischer Seite danken. Beide haben mir bei sowohl bei grundlegenden aber auch komplizierteren Problemen mit viel Geduld und Zeit weiter geholfen.

Dr. Wolfgang Suttrop und Dr. Manuel Garcia-Munoz möchte ich für ihre Hilfestellung und Diskussionsbereitschaft danken und dafür, dass sie stets das Potenzial in meiner Arbeit gesehen haben.

Prof. Sybille Günter und Prof. Karl Lackner danke ich für Ihre guten Ratschläge und Anregungen, die diese Arbeit in vieler Weise bereichert haben.

Weiterhin möchte ich Dr. Garret Conway für sein Interesse an meiner Arbeit und seine guten Ratschläge und Korrekturen danken. Auch war es für mich sehr interessant und lehrreich, dass er mir Einblick in seine Arbeit gewährt hat.

Dr. Emanule Poli danke ich dafür, dass er sich Zeit genommen hat meinen Theorie-Kapitel sehr ausführlich zu lesen und mir eine Reihe unglaublich guter Verbesserungsvorschläge zu machen.

Dr. Matthias Reich und Dr. Rachael McDermott bin ich sehr dankbar für ihre Unterstützung bei der Vorbereitung von Experimenten und der Auswertung und Interpretation von Daten.

Ich möchte mich auch bei Dr. Anja Gude und Dr. Valentin Igochine bedanken, die mir unter anderem geholfen haben die Daten der Soft X-Ray Diagnostik zu analysieren und richtig zu verwenden.

Bei Dr. Karl Behler und Dr. Roland Merkel möchte ich mich für ihre allgegenwärtige Bereitschaft, mir bei allen noch so kleinen Computerproblemen mit Rat und Tat zur Seite zu stehen, bedanken.

Ein großer Dank gilt allen Doktoranden und Post-Doktoranden, die nicht nur durch fachliche Diskussionen und Unterstützung zum gelingen dieser Arbeit beigetragen haben, sondern die auch die Arbeitsatmosphäre und die gesamten letzten drei Jahre zu etwas besonderem gemacht haben. Vielen Dank an euch: Leena Aho-Mantila, Laura Barrera-Orte, Matthias Bernert, Gregor Birkenmeier, Jurrian Boom, Andreas Burckhart, Livia Casali, Marco Cavedon, Mike Dunne, Benedikt Geiger, Tim Happel, Athina Kappatou, Alexander Lebschy, Tilmann Lunt, Steffen Potzel, Sylvia Rathgeber, Philip Schneider, Fabian Sommer, Chris-

tian Vorpahl, und Matthias Willensdorfer.
Dir liebe Eli danke ich besonders, dafür dass du mit mir durch dick und dünn gegangen bist, mich immer wieder aufgebaut hast und einfach immer für mich da warst.
Zu guter Letzt möchte ich mich beim gesamte ASDEX Upgrade Team bedanken. Ohne euch wäre diese Arbeit nicht möglich gewesen, vielen Dank!

List of journal publications

1. **S. Fietz**, E. Fable, J. Hobirk, R. Fischer, C. Fuchs, G. Pereverzev, F. Ryter and the ASDEX Upgrade Team,
   Investigation of transport models in ASDEX Upgrade current ramps, Nuclear Fusion **53** (2013)

2. **S. Fietz**, A. Bergmann, I. Classen, M. Maraschek, M. Garcia-Munoz, W. Suttrop, H. Zohm and the ASDEX Upgrade Team,
   Influence of externally applied magnetic perturbations on neoclassical tearing modes at ASDEX Upgrade (in preparation)

3. **S. Fietz**, M. Maraschek, H. Zohm, M. Reich, L. Barrera R.M. McDermott and the ASDEX Upgrade Team,
   Influence of rotation on the (m,n)=(3,2) neoclassical tearing mode threshold in ASDEX Upgrade, Plasma Physics and Controlled Fusion **55** (2013)

4. S.K. Rathgeber, R. Fischer, **S. Fietz**, J. Hobirk, A. Kallenbach, H. Meister, T. Pütterich, F. Ryter, G. Tardini, E. Wolfrum and the ASDEX Upgrade Team,
   Estimation of profiles of the effective ion charge at ASDEX Upgrade with Integrated Data Analysis, Plasma Physics and Controlled Fusion **52** (2010)

5. M. Garcia-Munoz, S. Akaslampolo, O. Asunta, J. Boom, X. Chen, I. G. J. Classen, R. Dux, T. E. Evans, **S. Fietz**, R. K. Fisher, C. Fuchs, B. Geiger, W. W. Heidbrink, M. Hoelzl, V. Igochine, J. Kim, J. Y. Kim, T. Kurki-Suonio, B. Kurzan, N. Lazanyi, N. Luhmann, T. Lunt, R. M. McDermott, M. Maraschek, M. Nocente, H. Park, G. I. Pokol, D. C. Pace, T. L. Rhodes, K. Shinohara, W. Suttrop, M. A. Van Zeeland, E. Viezzer, M. Willensdorfer, E. Wolfrum and the ASDEX Upgrade, DIII-D and KSTAR Teams
   Fast-ion redistribution and loss due to edge perturbations in the ASDEX Upgrade, DIII-D and KSTAR tokamaks, Nuclear Fusion **IAEA-CN-197** EX/P6-03 (2012)

6. E. Fable, C. Angioni, J. Hoebirk, G. and Pereverzev, **S. Fietz**, T. Hein and the ASDEX Upgrade Team,
   Confinement and transport properties during current ramps in the ASDEX Upgrade Tokamak, Nuclear Fusion **51** (2011)

7. M. Garcia-Munoz, S. Akaslampolo, O. Asunta, J. Boom, X. Chen, I. G. J. Classen, R. Dux, T. E. Evans, **S. Fietz**, R. K. Fisher, C. Fuchs, B. Geiger, W. W. Heidbrink, M. Hoelzl, V. Igochine, J. Kim, J. Y. Kim, T. Kurki-Suonio, B. Kurzan, N. Lazanyi, N. Luhmann, T. Lunt, R. M. McDermott, M. Maraschek, M. Nocente, H. Park, G. I. Pokol, D. C. Pace, T. L. Rhodes, K. Shinohara, W. Suttrop, M. A. Van Zeeland, E. Viezzer, M. Willensdorfer, E. Wolfrum and the ASDEX Upgrade, DIII-D and KSTAR Teams
   Fast-ion redistribution and loss due to edge perturbations in the ASDEX Upgrade, DIII-D and KSTAR tokamaks, Nuclear Fusion **53** (2013)

8. M. Garcia-Munoz, S. Akaslampolo, P. de Marne, R. Dux, T. E. Evans, N. M. Ferraro, **S. Fietz**, C. Fuchs, B. Geiger, A. Herrmann, M. Hoelzl, B. Kurzan, N. Lazanyi, R. M. McDermott, D. C. Pace, M. Rodriguez-Ramos, K. Shinohara, E. Strumberger, W. Suttrop, M. A. Van Zeeland, E. Viezzer, M. Willensdorfer, E. Wolfrum and the ASDEX Upgrade Team

   Fast-ion losses induced by ELMs and externally applied magnetic perturbations in the ASDEX Upgrade tokamak, Plasma Physics and Controlled Fusion **55** (2013)